DISSERTATION

OPTIMAL HIGHER ORDER MODELING METHODOLOGY BASED ON METHOD OF MOMENTS AND FINITE ELEMENT METHOD FOR ELECTROMAGNETICS

Submitted by

Eve Marian Klopf

Department of Electrical and Computer Engineering

In partial fulfillment of the requirements

For the Degree of Doctor of Philosophy

Colorado State University

Fort Collins, Colorado

Fall 2011

Doctoral Committee:

Advisor: Branislav M. Notaroš

V. Chandrasekar
Steven C. Reising
Iuliana Oprea

ABSTRACT

OPTIMAL HIGHER ORDER MODELING METHODOLOGY BASED ON METHOD OF MOMENTS AND FINITE ELEMENT METHOD FOR ELECTROMAGNETICS

General guidelines and quantitative recipes for adoptions of optimal higher order parameters for computational electromagnetics (CEM) modeling using the method of moments and the finite element method are established and validated, based on an exhaustive series of numerical experiments and comprehensive case studies on higher order hierarchical CEM models of metallic and dielectric scatterers. The modeling parameters considered are: electrical dimensions of elements (subdivisions) in the model (*h*-refinement), polynomial orders of basis and testing functions (*p*-refinement), orders of Gauss-Legendre integration formulas (numbers of integration points – integration accuracy), and geometrical orders of elements (orders of Lagrange-type curvature) in the model. The goal of the study, which is the first such study of higher order parameters in CEM, is to reduce the dilemmas and uncertainties associated with the great modeling flexibility of higher order elements, basis and testing functions, and integration procedures (this flexibility is the principal advantage but also the greatest shortcoming of the higher order CEM), and to ease and facilitate the decisions to be made on how to actually use them, by both CEM developers and practitioners. The ultimate goal is to

close the large gap between the rising academic interest in higher order CEM, which evidently shows great numerical potential, and its actual usefulness and application to electromagnetics research and engineering applications.

TABLE OF CONTENTS

Page

ACKNOWLEDGEMENTS

Thank you to Nada Šekeljić, Sanja Manić, Dr. Milan Ilić and Dr. Branislav Notaroš, whose help made this dissertation possible. Thank you all for your help, guidance, and endless patience. Also, thank you to Ana Manić and Elena Chobanyan, as well as Nada Šekeljić and Sanja Manić, for all of our lunches and chats about life, the lab, and everything.

Also, thank you to my wonderful husband, Seth Anthony, for all the evenings he brought me dinner at the lab.

1. INTRODUCTION AND MOTIVATION OF THE WORK

1.1. Problem Statement

Traditional computational electromagnetics (CEM) tools are low-order techniques (also referred to as small-domain or subdomain) – the electromagnetic structure is modeled by volume and/or surface geometrical elements that are electrically very small and with planar sides, and the fields and/or currents within the elements are approximated by low-order basis functions, which results in very large requirements in computational resources. An alternative which can greatly reduce the number of unknowns for a given problem and enhance the accuracy and efficiency of the CEM analysis is the higher order (also known as the large-domain or entire-domain) computational approach, which utilizes higher order basis functions defined in large geometrical elements [1]. Relatively recently, the CEM community has started to very extensively investigate and employ higher order surface and volume elements and higher order basis functions, mostly in the frame of the method of moments (MoM) [2-22], the finite element method (FEM) [2], [5], [23-36], and hybrid approaches [37-43].

However, the principal advantage of higher-order techniques, their flexibility in terms of the size and shape of elements and spans of approximation functions, is also their greatest shortcoming – in terms of dilemmas, uncertainties, and so many open, equally attractive, options and decisions to be made on how to actually use them. In other words,

the additional flexibility can be also considered a drawback in the sense that a user has to handle many more parameters in building an EM model, which requires a much deeper knowledge and understanding of the technique, as well as a great deal of modeling experience and expertise, and possibly considerably increases the overall simulation (modeling plus computation) time.

1.2. Overview of Previous Research

In terms of previous research toward the development of general guidelines and quantitative recipes for adoptions of higher-order parameters for CEM modeling, the following works provide some insightful information about typical orders of large-domain polynomial basis functions and numbers of unknowns, and the maximum electrical dimensions of elements used in the models. A 1970 paper [44] shows that the current along a thin straight wire dipole that is one wavelength (λ) long can be accurately calculated using MoM with entire-domain polynomial basis functions of the fourth order along each of the dipole arms. In [9] and [45], it has been shown that with the Galerkin testing procedure, which is found to be an optimal choice for testing, and polynomial basis functions, as few as only three to four unknowns per λ suffice for an accurate MoM analysis of wires, and that this type of approximation outperforms all of the alternative approximations. In an entire-domain MoM analysis of a $\lambda \times \lambda$ large metallic plate scatterer [10], polynomial orders of 6 to 9 yield almost identical solutions for the surface currents, with an eighth-order solution being adopted as a benchmark. Polynomial approximation of the eighth order provides an optimal solution for the volume current distribution in the MoM analysis of a 2λ long rod-like dielectric scatterer [46]. A large-domain 1-D FEM

numerical study [47] demonstrates that polynomial bases of orders 8 and higher can yield unstable results in single precision and that the optimal order of 1-D elements (with respect to the minimal number of unknowns for the prescribed 1% [0.04 dB] accuracy of the RMS of the scattered electric field) is about seven in single precision, with five unknowns per λ. Works on a higher order MoM in the framework of the surface integral equation (SIE) approach, FEM, and hybrid FEM-MoM techniques [7], [24], [25], [37] demonstrate examples using 2-D and 3-D elements that are about 2λ in each dimension.

In terms of previous research toward the optimal selection of numbers of integration points within MoM and FEM elements, which as well is an important part of this present study, an excellent and extremely comprehensive mathematical survey of integration formulas can be found in [48]. In addition, in CEM, the accuracy and efficiency of numerical integrations are tightly coupled to singularity cancellation and extraction techniques [1], [46], [49], [50]. However, as we deal in this study with elements of various electrical sizes (up to very large ones), we seek rules and guidelines that would relate the number of integration points ($N_{\text{integration}}$) to the order of basis functions (N_{basis}) in each direction in the element. The few available pieces of information on this topic are by no means consistent nor complete and provide no clear guideline for CEM implementations. In [46], the formula $N_{\text{integration}} = N_{\text{basis}} + 1$ in the context of the Gauss-Legendre quadrature is found to be an optimal choice in a higher order MoM solution to a volume integral equation, and the same formula is used in [3], where it is also reported that the minimal number of integration points, needed by the Galerkin method, often approaches the number of unknowns. In the low-order FEM technique [51], a constant five-point Gauss-Legendre formula is utilized. In the higher order FEM technique [24],

the Gauss-Legendre integration formula in $N_{\text{integration}} = N_{\text{basis}} + 10$ points is implemented. In [52], $2(p + 1) + 1$ Gaussian points, where p is the element order, are employed in each direction for the semi-analytical integration scheme in an electromagnetic scattering code. Finally, in the higher order MoM technique with Lagrange-type interpolatory polynomial basis functions [6], a 12-point Gaussian quadrature is used for the third-order basis functions on curvilinear triangles, as it is found that such a quadrature yields a well-conditioned matrix.

1.3. Research Goals

This work develops – through very extensive numerical experiments and studies using higher order MoM-SIE and hybrid FEM-MoM techniques [7], [37] – as precise as possible quantitative recipes for adoptions of optimal (or nearly optimal) higher order and large-domain parameters for electromagnetic modeling. The parameters considered are: the number of elements or electrical dimensions of elements (subdivisions) in the model (*h*-refinement), polynomial orders of basis functions (*p*-refinement), which are the same as the orders of testing functions (we use the Galerkin method for testing), orders of Gauss-Legendre integration formulas (numbers of integration points – integration accuracy), and geometrical orders of elements (orders of Lagrange-type curvature) in the model. All these parameters can, theoretically, be arbitrary. By optimal parameters we mean the values of parameters that ideally (for simple problems) yield an accurate solution employing the least possible computational resources, or (for complex problems) provide a firm initial model (starting point) that can be further refined in a straightforward fashion, and the results can be checked for convergence. This is the first

such study of higher order parameters in CEM. The ultimate goal of this work and the continued future work in this area is to reduce those dilemmas and uncertainties associated with the great modeling flexibility of higher order elements and basis and testing functions, and to ease and facilitate their use, by both CEM developers and practitioners. The goal is to establish and validate general guidelines and instructions in order for the higher order CEM modeling methodology to be an easily used analysis and design tool, with a minimum of expert interaction required to produce valuable results in practical applications. Simply speaking, it is believed that this and similar future studies, including those on associated efficient higher order meshing techniques and algorithms (which are not discussed in this work), are the best, if not the only, way to close the large gap between the rising academic interest in the higher order CEM, which clearly shows great numerical potential, and its actual usefulness and use in electromagnetics research and engineering applications.

A partial objective of this work is the development of a parallelization procedure in order to reduce the computational time of the numerical calculations. Namely, MoM and FEM simulations at different frequencies are carried out in parallel on a small computer cluster. For this purpose, the previously developed parser based on the internet protocol (IP) has been adapted. Extensive modifications of the IP parser code have enabled the desired control over the input parameters and file transfers needed for the MoM and FEM simulations on the cluster.

Another research objective and an integral part of this work is the development and implementation of a higher order technique for an indirect time-domain FEM analysis – namely, finding the time-domain response of a microwave passive structure based on the

FEM analysis in the frequency domain combined with the discrete Fourier transform (DFT) and its inverse (IDFT). The frequency-domain technique is a higher order large-domain Galerkin-type FEM for 3-D analysis of waveguide structures with discontinuities implementing curl-conforming hierarchical polynomial vector basis functions in conjunction with Lagrange-type curved hexahedral finite elements and a simple single-mode boundary condition [5], and it is coupled with standard DFT and IDFT algorithms. The goal is to demonstrate that, with a highly efficient and appropriately designed frequency-domain FEM solver, it is possible to obtain extremely fast and accurate time-domain solutions of microwave passive structures performing computations in the frequency domain along with the DFT and IDFT. Hence, the investigations and optimizations of modeling parameters may include simulations in the time domain as well.

1.4. Organization of the Dissertation

The dissertation is organized as follows. Chapter 2 briefly presents the mathematical background and main numerical components of the higher order MoM-SIE, FEM, and hybrid FEM-MoM techniques, and defines all modeling parameters that are to be studied. Chapter 3 proposes and discusses a systematic analysis procedure and strategy for determining optimal parameters through numerical experiments. In Chapter 4, an exhaustive series of simulations and comprehensive case studies on higher order models of metallic and dielectric scatterers is performed, through which a set of general guidelines and instructions and quantitative recipes for adoptions of optimal simulation parameters is established and validated. Chapter 5 summarizes the main conclusions of

the study, and puts them in a broader perspective of current and future CEM research and practice. The work described in Chapters 3, 4 and 5 forms the basis of the paper "Optimal Modeling Parameters for Higher Order MoM-SIE and FEM-MoM Electromagnetic Simulations" [53], which is currently under review for publication in IEEE Transactions on Antennas and Propagation. In Chapter 6, a computational technique is presented for efficient and accurate time-domain analysis of multiport waveguide structures with arbitrary metallic and dielectric discontinuities using a higher order finite element method (FEM) in the frequency domain coupled with standard DFT and IDFT algorithms; the work described in this chapter forms the basis of the paper "Efficient Time-Domain Analysis of Waveguide Discontinuities Using Higher Order FEM in Frequency Domain" [54]. Finally, Chapter 7 outlines some directions for future work in the area of the present work.

2. HIGHER ORDER METHOD OF MOMENTS, FINITE ELEMENT METHOD, AND HYBRID FEM-MOM

2.1. Higher Order Method of Moments

The surface integral equation (SIE) method, in which electric and magnetic surface currents are set over boundary surfaces separating homogeneous portions of the structure, and surface integral equations based on the boundary conditions for the electric and magnetic field intensity vectors are solved for the unknown current density values, is one of the most general approaches for analyzing metallic and dielectric structures. The method of moments (MoM) [55] can be used to discretize these SIEs, thus resulting in the development of MoM-SIE modeling techniques [56-58]. Overall, the MoM-SIE method is a robust and adaptable numerical method for simulations of electromagnetic fields within antenna and scattering applications involving both absorbing (dielectric and linear magnetic) and perfectly conducting materials. This section of the dissertation describes the higher-order Galerkin-type MoM-SIE technique for 3-D electromagnetics which is described in detail in reference [7]. This modeling method is based on higher-order current modeling and higher-order geometrical modeling, and is consequently referred to as a double-higher-order method.

Consider an electromagnetic system that is being excited by a time-harmonic electromagnetic field of complex field-intensities $\mathbf{E}_i$ and $\mathbf{H}_i$, with angular frequency ω;

this field may be the aggregate of an impressed field from one or more concentrated generators or from incident plane waves. Within the electromagnetic system, there are an arbitrary number of variously shaped metallic and dielectric objects. Using the surface equivalence principle (generalized Huygen's principle), we are able to break the system up into subsystems, each containing one of the dielectric regions (domains) found within the system, together with the metallic surfaces, with the homogenous surrounding space existing as its own domain (subsystem). Within each domain, the scattered electric and magnetic fields, **E** and **H**, can be formulated in terms of the equivalent (artificial) surface magnetic current, of density $\mathbf{M}_S$, and of the equivalent (artificial) surface electric current, of density $\mathbf{J}_S$, that are placed on the boundary surface for the domain with the intention of having zero field transfer from the domain into the surrounding space. It should be mentioned that only the surface electric currents, $\mathbf{J}_S$, exist on metallic surfaces, as these are actual currents, and $\mathbf{M}_S = 0$.

On the boundary surface between any two adjacent dielectric domains (domains 1 and 2), the boundary conditions for the tangential components of the total (incident plus scattered) electric and magnetic field vectors yield [7]

$$[\mathbf{E}(\mathbf{J}_S, \mathbf{M}_S, \varepsilon_1, \mu_1)]_{\text{tang}} + (\mathbf{E}_i)_{\text{tang}} = [\mathbf{E}(-\mathbf{J}_S, -\mathbf{M}_S, \varepsilon_2, \mu_2)]_{\text{tang}}, \tag{2.1}$$

$$[\mathbf{H}(\mathbf{J}_S, \mathbf{M}_S, \varepsilon_1, \mu_1)]_{\text{tang}} + (\mathbf{H}_i)_{\text{tang}} = [\mathbf{H}(-\mathbf{J}_S, -\mathbf{M}_S, \varepsilon_2, \mu_2)]_{\text{tang}}, \tag{2.2}$$

where we are making the assumption that the incident (impressed) field is present only in domain 1. We should also note that the boundary conditions (2.1) and (2.2) reduce to $(\boldsymbol{E}_{\text{tot}})_{\text{tang}} = 0$ on conducting bodies, so, for metallic surfaces in domain 1, we find [7]

$$[\mathbf{E}(\mathbf{J}_S, \mathbf{M}_S, \varepsilon_1, \mu_1)]_{\text{tang}} + (\mathbf{E}_i)_{\text{tang}} = 0. \tag{2.3}$$

In a region of complex permeability, μ, and complex permittivity, ε, we express the scattered electric field in terms of the electric and magnetic current densities as follows [7]:

$$\mathbf{E} = \mathbf{E}_{\mathrm{J}}(\mathbf{J}_S) + \mathbf{E}_{\mathrm{M}}(\mathbf{M}_S), \tag{2.4}$$

$$\mathbf{E}_{\mathrm{J}}(\mathbf{J}_S) = -\mathrm{j}\omega\mathbf{A} - \nabla\phi, \tag{2.5}$$

$$\mathbf{E}_{\mathrm{M}}(\mathbf{M}_S) = -\frac{1}{\varepsilon}\nabla\times\mathbf{F}, \tag{2.6}$$

while the scattered magnetic field is expressed as [7]

$$\mathbf{H} = \mathbf{H}_{\mathrm{M}}(\mathbf{M}_S) + \mathbf{H}_{\mathrm{J}}(\mathbf{J}_S), \tag{2.7}$$

$$\mathbf{H}_{\mathrm{M}}(\mathbf{M}_S) = -\mathrm{j}\omega\mathbf{F} - \nabla U, \tag{2.8}$$

$$\mathbf{H}_{\mathrm{J}}(\mathbf{J}_S) = \frac{1}{\mu}\nabla\times\mathbf{A} \tag{2.9}$$

where Φ and U are the electric and magnetic scalar potentials, and **F** and **A** are the electric and magnetic vector potentials, respectively. The potentials are obtained as [7]

$$\mathbf{A} = \mu\int_S \mathbf{J}_{\mathrm{S}} g\,\mathrm{d}S, \tag{2.10}$$

$$\mathbf{F} = \varepsilon\int_S \mathbf{M}_{\mathrm{S}} g\,\mathrm{d}S, \tag{2.11}$$

$$\Phi = \frac{\mathrm{j}}{\omega\varepsilon}\int_S \nabla_{\mathrm{S}}\cdot\mathbf{J}_{\mathrm{S}} g\,\mathrm{d}S, \tag{2.12}$$

$$U = \frac{\mathrm{j}}{\omega\mu}\int_S \nabla_{\mathrm{S}}\cdot\mathbf{M}_{\mathrm{S}} g\,\mathrm{d}S. \tag{2.13}$$

In the above expressions, S is the boundary surface of the domain under consideration,

and g is the Green's function for the unbounded homogeneous medium of parameters μ and ε [7],

$$g = \frac{\mathrm{e}^{-\gamma R}}{4\pi R}, \qquad \gamma = \mathrm{j}\omega\sqrt{\varepsilon\mu}, \tag{2.14}$$

with R being the distance from the source point to the field point, and γ being the propagation coefficient in the medium. Keeping in mind the integral expressions for fields **E** and **H** in (2.4)-(2.13), (2.1)-(2.3) represent a system of coupled electric/magnetic field integral equations (EFIE/MFIE) which can be discretized and solved using the method of moments in order to find the unknown values for $\mathbf{J}_S$ and $\mathbf{M}_S$.

We can make the assumption that all dielectric and metallic surfaces within a system can be approximated by some number of arbitrary surface elements. We can then approximate the surface electric and magnetic current density vectors, $\mathbf{J}_S$ and $\mathbf{M}_S$, over each element in the model using an appropriately selected set of basis functions having unknown complex current-distribution coefficients. In order to solve for these coefficients, the EFIE/MFIE system in (2.1)-(2.3) is tested using the Galerkin method, i.e., the same functions are used as were selected for the current expansion. The four types of generalized Galerkin impedances, which appear as system matrix elements, correspond to the four possible combinations of electric and magnetic current testing functions, $\mathbf{J}_{Sm}$ and $\mathbf{M}_{Sm}$, defined on the m^{th} surface element, S_m, and the electric and magnetic basis functions, $\mathbf{J}_{Sn}$ and $\mathbf{M}_{Sn}$ that are defined on the n^{th} element in the model given by [7]

$$Z_{mn}^{\text{ee}} = \int_{S_m} \mathbf{J}_{Sm} \cdot \mathbf{E}_{\text{J}}(\mathbf{J}_{Sn}) \mathrm{d}S_m, \tag{2.15}$$

$$Z_{mn}^{\text{em}} = \int_{S_m} \mathbf{J}_{Sm} \cdot \mathbf{E}_{\text{M}}(\mathbf{M}_{Sn}) \mathrm{d}S_m, \tag{2.16}$$

$$Z_{mn}^{\mathrm{me}} = \int_{S_m} \mathbf{M}_{\mathrm{S}m} \cdot \mathbf{H}_{\mathrm{J}}(\mathbf{J}_{\mathrm{S}n}) \mathrm{d}S_m, \tag{2.17}$$

$$Z_{mn}^{\mathrm{mm}} = \int_{S_m} \mathbf{M}_{\mathrm{S}m} \cdot \mathbf{H}_{\mathrm{M}}(\mathbf{M}_{\mathrm{S}n}) \mathrm{d}S_m. \tag{2.18}$$

The generalized voltages which appear as excitation column-matrix elements are similarly evaluated as [7]

$$V_m^{\mathrm{e}} = \int_{S_m} \mathbf{J}_{\mathrm{S}m} \cdot \mathbf{E}_{\mathrm{i}} \mathrm{d}S_m, \tag{2.19}$$

$$V_m^{\mathrm{m}} = \int_{S_m} \mathbf{M}_{\mathrm{S}m} \cdot \mathbf{H}_{\mathrm{i}} \mathrm{d}S_m. \tag{2.20}$$

Substituting (2.5) into (2.15), expanding $\nabla_S \cdot (\mathbf{J}_{\mathrm{S}m} \phi_n)$, and then applying the surface divergence theorem results in the following expressions for the electric/electric Galerkin impedances [7]:

$$\begin{aligned} Z_{mn}^{\mathrm{ee}} &= -\mathrm{j}\omega \int_{S_m} \mathbf{J}_{\mathrm{S}m} \cdot \mathbf{A}_n \mathrm{d}S_m - \int_{S_m} \mathbf{J}_{\mathrm{S}m} \cdot \nabla_S \phi_n \mathrm{d}S_m \\ &= -\mathrm{j}\omega \int_{S_m} \mathbf{J}_{\mathrm{S}m} \cdot \mathbf{A}_n \mathrm{d}S_m + \int_{S_m} \phi_n \nabla_S \cdot \mathbf{J}_{\mathrm{S}m} \mathrm{d}S_m - \oint_{c_m} \mathbf{J}_{\mathrm{S}m} \phi_n \mathbf{n}_m \mathrm{d}l_m \end{aligned}, \tag{2.21}$$

where $\mathbf{n}_m$ is the outward normal to the boundary contour c_m for the surface S_m. When the divergence-conforming current expansion on boundary elements is implemented, either the two contributions of elements sharing an edge exactly cancel each other out in the final expression for generalized impedances or else the normal components of testing functions $\mathbf{J}_{\mathrm{S}m}$ are zero at the element edges, thus resulting in the final term of (2.21) having zero value. Then, by formulating the potentials in (2.21) in terms of the electric-current basis function $\mathbf{J}_{\mathrm{S}n}$ over the n^{th} surface element, S_n, we obtain [7]

$$Z_{mn}^{\mathrm{ee}} = -\mathrm{j}\omega\mu \int_{S_m} \int_{S_n} \mathbf{J}_{\mathrm{S}m} \cdot \mathbf{J}_{\mathrm{S}n} g \mathrm{d}S_n \mathrm{d}S_m + \frac{\mathrm{j}}{\omega\varepsilon} \int_{S_m} \int_{S_n} (\nabla_S \cdot \mathbf{J}_{\mathrm{S}m})(\nabla_S \cdot \mathbf{J}_{\mathrm{S}n}) g \mathrm{d}S_n \mathrm{d}S_m. \tag{2.22}$$

In a similar manner, starting from (2.6) and (2.11), expanding $\nabla\times(\mathbf{M}_n g)$, and then performing a cyclic permutation of the scalar triple product, the electric/magnetic generalized impedances in (2.16) can be expressed as [7]

$$\begin{aligned} Z_{mn}^{\mathrm{em}} &= -\frac{1}{\varepsilon}\int_{S_m}\mathbf{J}_{\mathrm{S}m}\cdot\nabla\times\mathbf{F}_n\mathrm{d}S_m = -\int_{S_m}\int_{S_n}\mathbf{J}_{\mathrm{S}m}\cdot\nabla\times(\mathbf{M}_{\mathrm{S}n}g)\mathrm{d}S_n\mathrm{d}S_m \\ &= -\int_{S_m}\int_{S_n}\mathbf{J}_{\mathrm{S}m}\cdot(\nabla g\times\mathbf{M}_{\mathrm{S}n})\mathrm{d}S_n\mathrm{d}S_m = -\int_{S_m}\int_{S_n}(\mathbf{M}_{\mathrm{S}n}\times\mathbf{J}_{\mathrm{S}m})\cdot\nabla g\mathrm{d}S_n\mathrm{d}S_m \end{aligned} . \tag{2.23}$$

Using duality, the magnetic/electric and magnetic/magnetic generalized Galerkin impedances in (2.17) and (2.18) can be seen to have the same respective forms as the electric/electric and electric/magnetic generalized Galerkin impedances shown in (2.22) and (2.23), and are given by [7]

$$Z_{mn}^{\mathrm{me}} = -\int_{S_m}\int_{S_n}(\mathbf{J}_{\mathrm{S}n}\times\mathbf{M}_{\mathrm{S}m})\cdot\nabla g\mathrm{d}S_n\mathrm{d}S_m = -Z_{mn}^{\mathrm{em}}, \tag{2.24}$$

$$Z_{mn}^{\mathrm{mm}} = -\mathrm{j}\omega\varepsilon\int_{S_m}\int_{S_n}\mathbf{M}_{\mathrm{S}m}\cdot\mathbf{M}_{\mathrm{S}n}g\mathrm{d}S_n\mathrm{d}S_m + \frac{\mathrm{j}}{\omega\mu}\int_{S_m}\int_{S_n}(\nabla_S\cdot\mathbf{M}_{\mathrm{S}m})(\nabla_S\cdot\mathbf{M}_{\mathrm{S}n})g\mathrm{d}S_n\mathrm{d}S_m . \tag{2.25}$$

The impedance equations (2.22)-(2.25) give general expressions for MoM generalized impedances for solving the EFIE/MFIE system in (2.1)-(2.3) using any set of divergence-conforming basis functions and any kind of surface discretization in the context of the Galerkin method.

In this higher order MoM-SIE technique, dielectric and metallic surfaces of an electromagnetic structure (antenna or scatterer) being simulated are modeled using Lagrange-type generalized curved parametric quadrilaterals of arbitrary geometrical orders K_u and K_v ($K_u, K_v \geq 1$), seen in Fig. 2.1 and analytically described as [7]

$$\mathbf{r}(u,v) = \sum_{k=0}^{K_u}\sum_{l=0}^{K_v}\mathbf{r}_{kl}L_k^{K_u}(u)L_l^{K_v}(v), \quad -1\leq u,v\leq 1, \tag{2.26}$$

where $\mathbf{r}_{kl} = \mathbf{r}(u_k, v_l)$ are position vectors having $M = (K_u+1)(K_v+1)$ interpolation nodes and $L_k^{K_u}$ represent Lagrange interpolation polynomials given by [7]

$$L_k^{K_u}(u) = \prod_{\substack{i=0 \\ i \neq k}}^{K_u} \frac{u - u_i}{u_k - u_i}, \tag{2.27}$$

with u_i being the interpolation nodes along the interval $-1 \le u \le 1$ (note that $L_k^{K_u}$ is unity for $u = u_k$ and zero at all other nodes), with $L_l^{K_v}(v)$ being similarly defined.

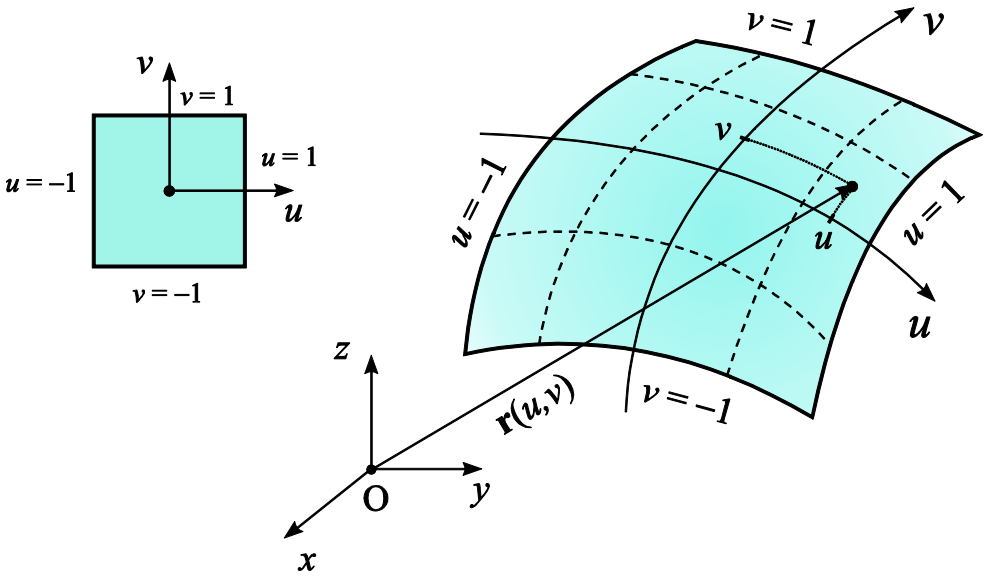

Fig. 2.1. Generalized curved parametric quadrilateral defined by (2.26), with the square parent domain [7].

In Fig.2, the most simple generalized quadrilateral is shown; this quadrilateral, known as the bilinear quadrilateral, is defined by $K_u = K_v = 1$. It is determined entirely by $M = 4$ interpolation points – its 4 vertices (arbitrarily positioned in space), so that (2.26) becomes

$$\mathbf{r}(u,v) = \frac{1}{4}[\mathbf{r}_1(1-u)(1-v) + \mathbf{r}_2(u+1)(1-v) + \mathbf{r}_3(1-u)(v+1) + \mathbf{r}_4(u+1)(v+1)] \\ = \mathbf{r}_{00} + \mathbf{r}_{10}u + \mathbf{r}_{01}v + \mathbf{r}_{11}uv \quad . \tag{2.28}$$

The edges and coordinate lines for the quadrilateral are all straight, while its surface is slightly curved (inflexed). We should notice that these quadrilaterals afford equal or improved flexibility for geometrical modeling of general electromagnetic objects as compared to commonly used elements such as flat triangular and rectangular patches, while using generalized quadrilaterals of higher (K_u, K_v > 1) geometrical orders, of course, result in additional modeling flexibility and accuracy.

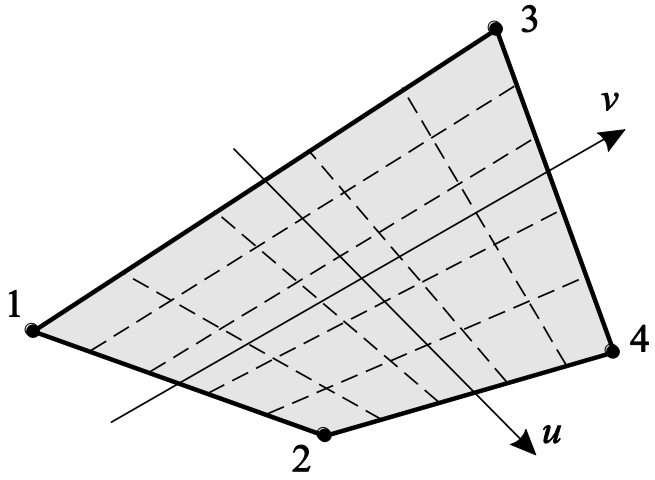

Fig. 2.2. A bilinear quadrilateral (the simplest generalized quadrilateral, defined by K_u = K_v = 1) [7].

For higher-order geometrical elements, we use an equidistant distribution of interpolation nodes along each coordinate in the parametric space. For example, a quadrilateral of the 4th geometrical order, having $K_u = K_v = 4$, $M = 25$, is given by

$$\mathbf{r}(u,v) = \frac{4}{9}\mathbf{r}_1(u+0.5)u(u-0.5)(u-1)(v+0.5)v(v-0.5)(v-1)$$
$$-\frac{16}{9}\mathbf{r}_2(u+1)u(u-0.5)(u-1)(v+0.5)v(v-0.5)(v-1)+\ldots$$
$$+\frac{4}{9}\mathbf{r}_{25}(u+1)(u+0.5)u(u-0.5)(v+1)(v+0.5)v(v-0.5)$$
$$=\mathbf{r}_{00}+\mathbf{r}_{10}u+\mathbf{r}_{20}u^2+\mathbf{r}_{30}u^3+\mathbf{r}_{40}u^4+\ldots+\mathbf{r}_{04}v^4+\mathbf{r}_{14}uv^4+\mathbf{r}_{24}u^2v^4+\mathbf{r}_{34}u^3v^4+\mathbf{r}_{44}u^4v^4$$
$$-1\le u,v\le 1. \qquad (2.29)$$

The electric and magnetic surface current density vectors, $\mathbf{J}_s$ and $\mathbf{M}_s$, over every generalized quadrilateral in the model are approximated by means of divergence-conforming hierarchical-type vector basis functions consisting of simple power functions (P) in parametric coordinates u and v [7],

$$\mathbf{J}_s = \frac{1}{\Im}\left[\sum_{i=0}^{N_u}\sum_{j=0}^{N_v-1}\alpha_{ij}^{(u)} f_{ij}^{(u)}(u,v)\mathbf{a}_u + \sum_{i=0}^{N_u-1}\sum_{j=0}^{N_v}\alpha_{ij}^{(v)} f_{ij}^{(v)}(u,v)\mathbf{a}_v\right],$$

$$\mathbf{M}_s = \frac{1}{\Im}\left[\sum_{i=0}^{N_u}\sum_{j=0}^{N_v-1}\beta_{ij}^{(u)} f_{ij}^{(u)}(u,v)\mathbf{a}_u + \sum_{i=0}^{N_u-1}\sum_{j=0}^{N_v}\beta_{ij}^{(v)} f_{ij}^{(v)}(u,v)\mathbf{a}_v\right],$$

$$f_{ij}^{(u)} = \hat{P}_i(u)P_j(v),\ f_{ij}^{(v)} = P_i(u)\hat{P}_j(v), \qquad (2.30)$$

where $\hat{P}$ denotes the modified (divergence-conforming) power functions [7],

$$\hat{P}_i(u) = \begin{cases} 1-u, & i=0 \\ u+1, & i=1 \\ u^i-1, & i\ge 2, \text{even} \\ u^i-u, & i\ge 3, \text{odd} \end{cases},\ P_j(v)=v^j,\ -1\le u,v\le 1. \qquad (2.31)$$

$\{\alpha\}$ and $\{\beta\}$ are the unknown current-distribution coefficients, N_u and N_v (N_u, $N_v \ge 1$) are the adopted orders of the polynomial current approximation in the u- and v-direction, respectively, which are entirely independent from the element geometrical orders (K_u and

K_v,), and $\Im$ is the Jacobian of the covariant transformation, which is found from the unitary vectors $\mathbf{a}_u$ and $\mathbf{a}_v$ along the parametric coordinates [7],

$$\Im = |\mathbf{a}_u \times \mathbf{a}_v|, \qquad \mathbf{a}_u = \partial\mathbf{r}/\partial u, \qquad \mathbf{a}_v = \partial\mathbf{r}/\partial v, \tag{2.32}$$

with $\mathbf{r}$ given in (2.26). It should be noticed that the limits of the sum in (2.30) corresponding to the variations of a current density vector component in the direction across that component are smaller by one than the orders corresponding to variations in the other parametric coordinate. This mixed-order arrangement has been found to be an excellent general choice for modeling of surface currents as it ensures equal approximation orders for surface charge densities corresponding to the *u*- and *v*-directed current basis functions.

Polynomial degrees in the current expansions (N_u and N_v) can be high, which allows us to use electrically large boundary elements. Doing so greatly reduces the overall number of unknowns for a given problem and significantly enhances the accuracy and efficiency of the technique, as compared to traditionally used low-order basis functions. These basis functions automatically satisfy continuity boundary conditions for the current components normal to the quadrilateral edges shared by adjacent elements in the structure (divergence-conforming functions).

The basis functions defined in (2.31) are hierarchical functions – every lower-order set of functions is a subset of all higher-order sets. These functions enable using different orders of current approximation in different elements, which allows for a whole spectrum of "regular" and "irregular" shapes and element sizes, with the corresponding current approximation orders, to be used simultaneously within a single simulation model of a complex structure. They also enable a very efficient *p*-refinement of the model, where the

accuracy of the solution is improved through the optimal selection of polynomial orders of the basis functions within the same geometrical elements, which is done without changing the geometrical discretization of the structure. Hierarchical basis functions, on the other hand, typically have poor orthogonality properties, which results in MoM matrices with large condition numbers. However, the MoM matrix condition number can be lowered by modifying the basis functions in a way that causes a strong mutual coupling between the pairs of higher-order functions defined on the same (electrically large) quadrilateral patch to be reduced. For example, higher-order basis functions constructed from ultraspherical and Chebyshev orthogonal polynomials on bilinear quadrilaterals result in the reduction of the MoM matrix condition number by several orders of magnitude [24], [59].

Properties of the basis functions in (2.31) allow the connection of any two (or more) quadrilateral elements regardless of their adopted geometrical orders, current-expansion orders, or the local orientations of parametric coordinates. The only requirement that must be satisfied is the geometrical compatibility of the edges between adjacent quadrilaterals in a junction over which the current-continuity boundary condition is adjusted. Basis functions containing the terms P_0 and P_1 in an arbitrary quadrilateral serve for adjusting the boundary condition at the corresponding quadrilateral edges (u, $v = \pm 1$; the remaining basis functions are zero at the quadrilateral edges and serve for improving the current approximation over the surface. In the assembly procedure in [7], the geometrical interpolation nodes associated with two quadrilaterals that govern the geometry of a common edge are ordered in a way that ensures a symmetrical or antisymmetrical variation of the corresponding parametric coordinates. The continuity of

the normal surface current density components across a common edge is enforced by equating the corresponding normal-component current coefficients associated with the quadrilaterals, with additional corrections related to possibly different element orientations. For elements with different current-expansion orders, the normal-component current coefficients are matched only up to the lesser of the corresponding orders and are set to zero for the remaining normal-component current basis functions. This order reduction pertains to the common edge only and does not affect expansions over the remaining surfaces of the elements. In situations when more than two quadrilaterals share a common edge, the overall adjustment of the continuity boundary condition across the edge is accomplished by cyclically performing the assembly procedure for element pairs (1, 2), (2, 3), …, and (*L*–1, *L*), where *L* is the number of quadrilaterals in the junction [7].

In (2.30), the unknown coefficients, {α} and {β}, are found by solving the EFIE/MFIE system of with the generalized Galerkin impedances in (2.22)-(2.25), which are specialized for the use of hierarchical divergeance-conforming polynomial vector basis functions of arbitrary current-approximation orders, (2.31), and generalized curved quadrilateral elements of arbitrary geometrical orders, (2.26). Without losing generality, we can consider only the *u*-components of the basis and testing functions. Moreover, we can consider the functions in a simplified form, as follows [7]:

$$\mathbf{f}_{ij}(u,v) = \frac{\Gamma_{ij}(u,v)}{J(u,v)} \frac{\partial \mathbf{r}(u,v)}{\partial u}, \tag{2.33}$$

where Γ are the simple two-dimensional power functions,

$$\Gamma_{ij}(u,v) = u^i v^j. \tag{2.34}$$

The impedances for any higher-order set of basis functions of divergence-conforming

polynomial type can be constructed as a linear combination of the impedances corresponding to the simple power functions in (2.33) and (2.34). An interesting example of this are the higher-order basis functions with improved orthogonality properties composed of ultraspherical and Chebyshev polynomials [59]. Consequently, the generalized Gelerkin impedances corresponding to the basis functions in (2.31) can be formulated as a linear combination of those corresponding to the simplified forms in (2.33) and (2.34).

Subsequent to the substitution of (2.33) into (2.22), the electric/electric impedances corresponding to the basis function defined by the indices i_n and j_n on the n^{th} quadrilateral and the testing function defined by indices i_m and j_m on the m^{th} quadrilateral become [7]

$$Z^{\text{ee}}(i_m, j_m, i_n, j_n) = -\text{j}\omega\mu \int_{u_{1m}}^{u_{2m}} \int_{v_{1m}}^{v_{2m}} \int_{u_{1n}}^{u_{2n}} \int_{v_{1n}}^{v_{2n}} \left(\Gamma_{i_m j_m} \frac{\partial \mathbf{r}_m}{\partial u_m} \right) \cdot \left(\Gamma_{i_n j_n} \frac{\partial \mathbf{r}_n}{\partial u_n} \right) g(R) \text{d}u_n \text{d}v_n \text{d}u_m \text{d}v_m$$
$$+ \frac{\text{j}}{\omega\varepsilon} \int_{u_{1m}}^{u_{2m}} \int_{v_{1m}}^{v_{2m}} \int_{u_{1n}}^{u_{2n}} \int_{v_{1n}}^{v_{2n}} \frac{\partial \Gamma_{i_m j_m}}{\partial u_m} \frac{\partial \Gamma_{i_n j_n}}{\partial u_n} g(R) \text{d}u_n \text{d}v_n \text{d}u_m \text{d}v_m \quad , \qquad (2.35)$$
$$i_m = 0, 1, \ldots, N_u^{(m)}, \quad j_m = 0, 1, \ldots, N_v^{(m)}, \quad i_n = 0, 1, \ldots, N_u^{(n)}, \quad j_n = 0, 1, \ldots, N_v^{(n)}$$

where $N_u^{(n)}$ and $N_v^{(n)}$ are the orders of the n^{th} quadrilateral along the u- and v-coordinate, respectively, and $N_u^{(m)}$ and $N_v^{(m)}$ are the current-approximation orders of the m^{th} quadrilateral along the u- and v-coordinate, where the integration limits for both quadrilaterals are $u_1 = v_1 = 1$ and $u_2 = v_2 = 1$. The source-to-field distance, R, is calculated as

$$R = |\mathbf{r}_m(u_m, v_m) - \mathbf{r}_n(u_n, v_n)|. \qquad (2.36)$$

If we consider the parametric representation of the quadrilateral surface element, (2.26), we can then obtain the final expression [7]:

$$Z^{\mathrm{ee}}(i_m, j_m, i_n, j_n) = \sum_{k_m=1}^{K_u^{(m)}} \sum_{l_m=0}^{K_v^{(m)}} \sum_{k_n=1}^{K_u^{(n)}} \sum_{l_n=0}^{K_v^{(n)}} k_m k_n \mathbf{r}_{kl}^{(m)} \cdot \mathbf{r}_{kl}^{(n)} \xi(i_m + k_m - 1, j_m + l_m, i_n + k_n - 1, j_n + l_n) - \frac{1}{\omega^2 \mu \varepsilon} i_m i_n \xi(i_m - 1, j_m, i_n - 1, j_n)$$

(2.37)

where $\mathbf{r}_{kl}^{(n)}$ are the geometrical vector coefficients in the polynomial expansion for the n^{th} quadrilateral, $K_u^{(n)}$ and $K_v^{(n)}$ are the geometrical orders along its *u*- and *v*-coordinates, respectively, $K_u^{(m)}$, $K_v^{(m)}$ and $\mathbf{r}_{kl}^{(m)}$ are the corresponding parameters of the m^{th} quadrilateral, and ξ is the basic Galerkin potential integral given by [7]

$$\xi(i_m, j_m, i_n, j_n) = -\mathrm{j}\omega\mu \int_{u_{1m}}^{u_{2m}} \int_{v_{1m}}^{v_{2m}} \int_{u_{1n}}^{u_{2n}} \int_{v_{1n}}^{v_{2n}} u_m^{i_m} v_m^{j_m} u_n^{i_n} v_n^{j_n} g(R) \mathrm{d}u_n \mathrm{d}v_n \mathrm{d}u_m \mathrm{d}v_m \,. \tag{2.38}$$

In a similar manner, using (2.33) and expanding the gradient of Green's function, the electric/magnetic impedances in (2.23) become

$$\begin{aligned} Z^{\mathrm{em}}(i_m, j_m, i_n, j_n) &= -\frac{1}{\varepsilon} \int_{S_m} \mathbf{f}_m \nabla \times \mathbf{F}_n \mathrm{d}S_m \\ &= -\int_{u_{1m}}^{u_{2m}} \int_{v_{1m}}^{v_{2m}} \int_{u_{1n}}^{u_{2n}} \int_{v_{1n}}^{v_{2n}} \Gamma_{i_m j_m} \Gamma_{i_n j_n} \left(\frac{\partial \mathbf{r}_n}{\partial u_n} \times \frac{\partial \mathbf{r}_m}{\partial u_m} \right) \cdot \nabla g(R) \mathrm{d}u_n \mathrm{d}v_n \mathrm{d}u_m \mathrm{d}v_m \\ &= -\int_{u_{1m}}^{u_{2m}} \int_{v_{1m}}^{v_{2m}} \int_{u_{1n}}^{u_{2n}} \int_{v_{1n}}^{v_{2n}} \Gamma_{i_m j_m} \Gamma_{i_n j_n} \left(\frac{\partial \mathbf{r}_n}{\partial u_n} \times \frac{\partial \mathbf{r}_m}{\partial u_m} \right) \cdot (\mathbf{r}_m - \mathbf{r}_n) \frac{1}{R} \frac{\mathrm{d}g(R)}{\mathrm{d}R} \mathrm{d}u_n \mathrm{d}v_n \mathrm{d}u_m \mathrm{d}v_m \end{aligned}$$

$$i_m = 0, 1, \ldots, N_u^{(m)}, \quad j_m = 0, 1, \ldots, N_v^{(m)}, \quad i_n = 0, 1, \ldots, N_u^{(n)}, \quad j_n = 0, 1, \ldots, N_v^{(n)}$$

(2.39)

Using (2.26) then results in [7]

$$Z^{\mathrm{em}}(i_m, j_m, i_n, j_n) =$$
$$\sum_{k'_m=0}^{K_u^{(m)}} \sum_{l'_m=0}^{K_v^{(m)}} \sum_{k_m=1}^{K_u^{(m)}} \sum_{l_m=0}^{K_v^{(m)}} \sum_{k_n=1}^{K_u^{(n)}} \sum_{l_n=0}^{K_v^{(n)}} k_m k_n \left(\mathbf{r}_{kl}^{(n)} \times \mathbf{r}_{kl}^{(m)}\right) \cdot \mathbf{r}_{k'l'}^{(m)} \zeta(i_m + k_m + k'_m - 1, j_m + l_m + l'_m, i_n + k_n - 1, j_n + l_n)$$
$$- \sum_{k'_n=0}^{K_u^{(n)}} \sum_{l'_n=0}^{K_v^{(n)}} \sum_{k_m=1}^{K_u^{(m)}} \sum_{l_m=0}^{K_v^{(m)}} \sum_{k_n=1}^{K_u^{(n)}} \sum_{l_n=0}^{K_v^{(n)}} k_m k_n \left(\mathbf{r}_{kl}^{(n)} \times \mathbf{r}_{kl}^{(m)}\right) \cdot \mathbf{r}_{k'l'}^{(n)} \zeta(i_m + k_m - 1, j_m + l_m, i_n + k_n + k'_n - 1, j_n + l_n + l'_n) \tag{2.40}$$

, where ζ is the basic Galerkin field integral evaluated as [7]

$$\zeta(i_m, j_m, i_n, j_n) = -\int_{u_{1m}}^{u_{2m}} \int_{v_{1m}}^{v_{2m}} \int_{u_{1n}}^{u_{2n}} \int_{v_{1n}}^{v_{2n}} u_m^{i_m} v_m^{j_m} u_n^{i_n} v_n^{j_n} \frac{1}{R} \frac{\mathrm{d}g(R)}{\mathrm{d}R} \mathrm{d}u_n \mathrm{d}v_n \mathrm{d}u_m \mathrm{d}v_m \,. \tag{2.41}$$

We should note that only two types of basic scalar Galerkin integrals, ξ and ζ in (2.38) and (2.42), are necessary for the entire Galerkin impedance matrix. Additionally, only ξ-integrals are needed for purely metallic objects.

The numerical integration is performed using the Gauss-Legendre integration formula. For example, the four-fold integration formula for the quadruple integrals ξ in (2.38) has the form [7]

$$[\xi(i_m, j_m, i_n, j_n)]_{\mathrm{numerical}} = -\mathrm{j}\omega\mu \sum_{p=1}^{NGL_{mu}} \sum_{q=1}^{NGL_{mv}} \sum_{s=1}^{NGL_{nu}} \sum_{t=1}^{NGL_{nv}} A_p A_q A_s A_t u_{m,p}^{i_m} v_{m,q}^{j_m} u_{n,s}^{i_n} v_{n,t}^{j_n} \cdot g[|\mathbf{r}_m(u_{m,p}, v_{m,q}) - \mathbf{r}_n(u_{n,s}, v_{n,t})|] \tag{2.42}$$

where $u_{m,p}$, $v_{m,q}$, $u_{n,s}$, and $v_{n,t}$ are arguments (zeros of the Legendre polynomials), NGL_{mu}, NGL_{mv}, NGL_{nu}, and NGL_{nv} are the adopted orders, and A_p, A_q, A_s, and A_t are weights of the corresponding Gauss-Legendre integration formulas. Of course, since the integrand contains Green's function, in (2.14), it is not a polynomial (in parametric coordinates), and the well-known accuracy characterizations of the quadrature formula, if applied to integrals of polynomials, are not applicable. Efficient algorithms for recursive construction of the generalized Galerkin impedances are used in order to avoid redundant

operations related to the indices for basis and testing functions (e.g., indices *i* and *j* in (2.30)), for geometrical representations (e.g., indices *k* and *l* in (2.26)) within all of the interactions in the MoM/FEM solution, and for the summation indices within the integration formulas (e.g., indices *p*, *q*, *s*, and *t* in (2.42)) [7].

The final system of linear algebraic equations having complex unknowns $\{\alpha\}$ and $\{\beta\}$ can then be solved classically, using Gaussian elimination. By post-processing using the calculated coefficients, the fields **E** and **H** in any dielectric region, including the far field, and the currents $\mathbf{J}_S$ and $\mathbf{M}_S$ over any generalized quadrilateral in the simulation can be found.

2.2. Higher Order Finite Element Method

Our FEM begins with the curl-curl electric-field vector wave equation [24]

$$\nabla \times \mu_r^{-1} \nabla \times \mathbf{E} - k_0^2 \varepsilon_r \mathbf{E} = 0 , \tag{2.43}$$

where **E** is the electric field complex intensity vector, which must be tangentially continuous as all material interfaces, ω is the angular frequency of the implied time-harmonic variation, $k_0 = \omega\sqrt{\varepsilon_0 \mu_0}$ is the free-space wave number, and μ_r and ε_r are the complex relative permeability and permittivity for the inhomogeneous medium, respectively. Even though all derivations in this section have been given in terms of the E-field formulation, they can also be modified for discretization of the magnetic-field wave equation (H-field formulation) using duality. A more extensive treatment of this method is given in references [24] and [60].

The Langrange-type interpolation generalized hexahedron, shown in Fig. 2.3, is the basic building block for volumetric FEM modeling. This hexahedron is a volume (3-D)

generalization of the quadrilateral patch in Fig. 2.1, and, consequently, can be expressed as a generalization of (2.26), as is discussed by [24], [25], [37], and [60],

$$\mathbf{r}(u,v,w)=\sum_{k=0}^{K_u}\sum_{l=0}^{K_v}\sum_{o=0}^{K_w}\mathbf{r}_{klo}L_k^{K_u}(u)L_l^{K_v}(v)L_o^{K_w}(w),\quad -1\le u,v,w\le 1. \tag{2.44}$$

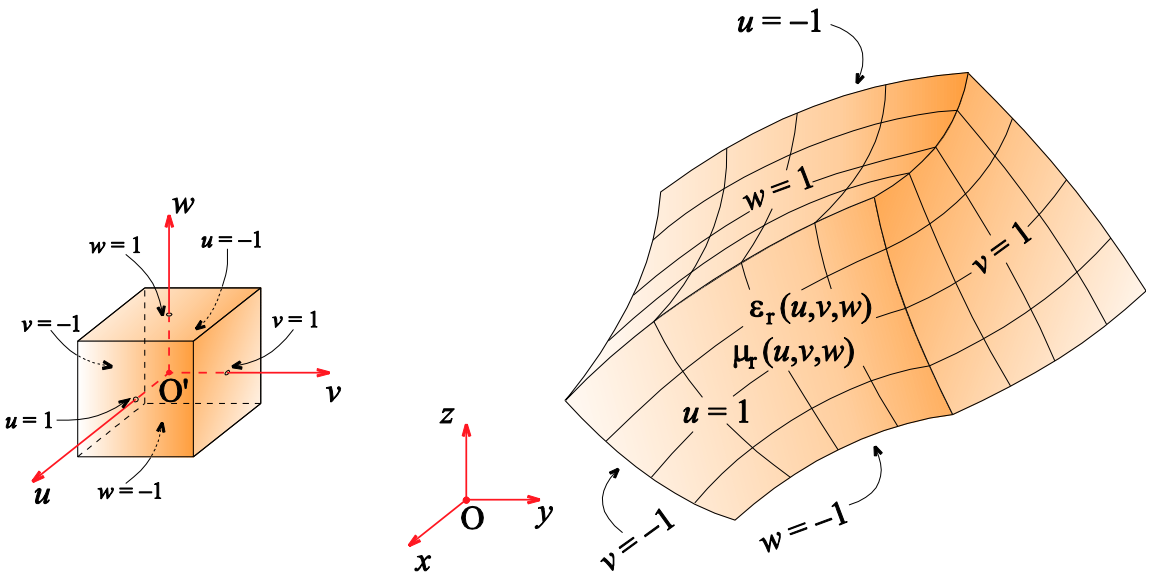

Fig. 2.3. Generalized curved parametric hexahedron defined by (2.44); cubical parent domain is also shown [24-26], [61].

In Fig. 2.4(a), the first-order element ($K_u = K_v = K_w = 1$), called the trilinear hexahedron [24], is shown with visible coordinate lines [60] [62-67]. We can see that it is entirely determined by $M = 8$ interpolation points, or vertices, so that (2.44) can be expressed as [60, p. 33]

$$\mathbf{r}(u,v,w)=\frac{1}{8}[\mathbf{r}_1(1-u)(1-v)(1-w)+\mathbf{r}_2(u+1)(1-v)(1-w)+\ldots+\mathbf{r}_8(u+1)(v+1)(w+1)]=$$
$$\mathrm{a}_{000}+a_{100}u+a_{010}v+a_{001}w+a_{110}uv+a_{101}uw+a_{011}vw+a_{111}uvw,\qquad -1\le u,v,w\le 1 \tag{2.45}$$

All edges and coordinate lines for the element are straight, while its sides are composed of bilinear quadrilateral surfaces, as in Fig. 2.2 [66]. Notice that these generalized hexahedra afford equivalent or improved flexibility for geometrical modeling of general electromagnetic structures when compared to more frequently used elements such as bricks, triangular prisms and tetrahedra. For triquadratic hexahedron, which is the second order element, having $K_u = K_v = K_w = 2$, $M = 27$, shown in Fig. 2.4(b), the 3-D interpolation polynomials in (2.44) can be given as [60]:

$$p_1(u,v,w) = -u(1-u)v(1-v)w(1-w)/8, \text{ node at } \mathbf{r}(-1,-1,-1);$$

$$p_2(u,v,w) = (1-u)(1+u)v(1-v)w(1-w)/4, \text{ node at } \mathbf{r}(0,-1,-1); \ldots,$$

$$p_{14}(u,v,w) = (1+u)(1-u)(1+v)(1-v)(1+w)(1-w), \text{ node at } \mathbf{r}(0,0,0); \ldots, \text{ and}$$

$$p_{27}(u,v,w) = u(1+u)v(1+v)w(1+w)/8, \text{ node at } \mathbf{r}(1,1,1). \tag{2.46}$$

Comparable expressions hold for parametric bodies of higher (K_u, K_v, $K_w > 2$) geometrical orders. Geometrically higher-order elements clearly allow better flexibility and accuracy in modeling of complex curved structures. For a simple example, Figs.2.4(a) and 2.4(b) show a sphere modeled by 1000 trilinear hexahedra and a single triquadratic hexahedron, respectively. Just by looking at these models, we can see that a single hexahedral finite element of the 2nd geometrical order provides an equal or better approximation of the sphere as compared to one thousand elements of the first geometrical order. However, using flexible higher-order curved elements is computationally worthwhile only if they are electrically large, which generally requires

that higher-order field expansions also be used with the elements. Additionally, if we are to implement the modeling of realistic structures in an optimal manner, it is ideal to have the ability to use elements of different orders and sizes within the same mesh. If these requirements are to be achieved, selecting hierarchical-type higher-order polynomial basis functions for the approximation of fields is the correct choice.

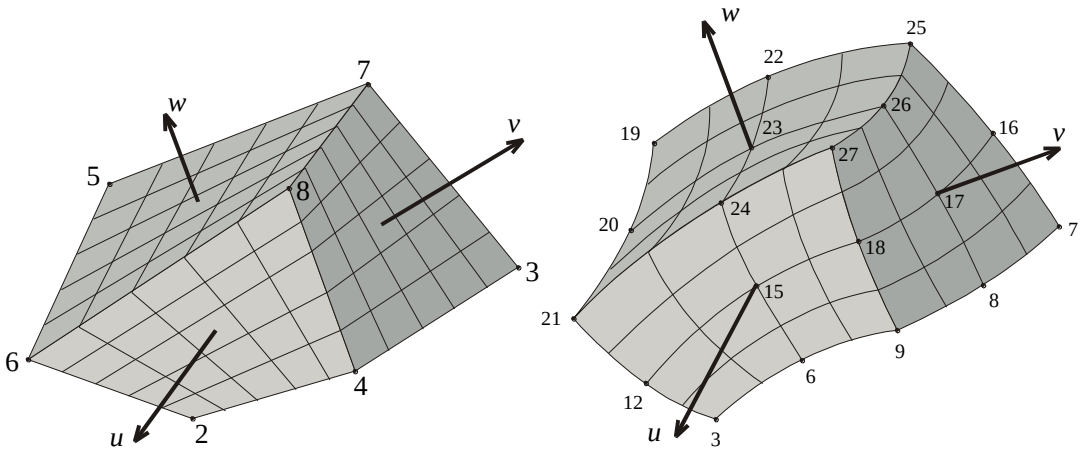

(a) (b)

Fig. 2.4. Two simplest generalized hexahedra described by Eq.(2.44): (a) trilinear hexahedron ($K_u = K_v = K_w = 1$), and (b) triquadratic hexahedron ($K_u = K_v = K_w = 2$) , [37], [60].

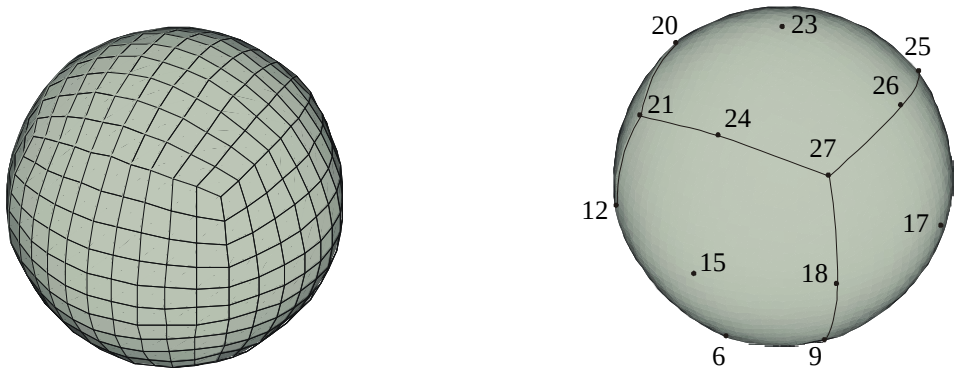

(a) (b)

Fig. 2.5. A sphere modeled by (a) 1000 trilinear hexahedra of Fig. 2.4(a) and (b) a single triquadratic hexahedron of Fig. 2.4(b), [60].

The electric field vector, **E**, inside the FEM hexahedra is approximated by curl-conforming hierarchical vector expansions obtained as a curl-conforming 3-D version of divergence-conforming 2-D bases in (2.30) [24],

$$\mathbf{E} = \sum_{i=0}^{N_u-1}\sum_{j=0}^{N_v}\sum_{r=0}^{N_w}\gamma_{ijr}^{(u)}P_i(u)\hat{P}_j(v)\hat{P}_r(w)\mathbf{a}'_u + \sum_{i=0}^{N_u}\sum_{j=0}^{N_v-1}\sum_{r=0}^{N_w}\gamma_{ijr}^{(v)}\hat{P}_i(u)P_j(v)\hat{P}_r(w)\mathbf{a}'_v + \sum_{i=0}^{N_u}\sum_{j=0}^{N_v}\sum_{r=0}^{N_w-1}\gamma_{ijr}^{(w)}\hat{P}_i(u)\hat{P}_j(v)P_r(w)\mathbf{a}'_w$$

$$\mathbf{a}'_u = \frac{\mathbf{a}_v \times \mathbf{a}_w}{\mathfrak{J}},\quad \mathbf{a}'_v = \frac{\mathbf{a}_w \times \mathbf{a}_u}{\mathfrak{J}},\quad \mathbf{a}'_w = \frac{\mathbf{a}_u \times \mathbf{a}_v}{\mathfrak{J}},\quad \mathfrak{J} = (\mathbf{a}_u \times \mathbf{a}_v)\cdot\mathbf{a}_w,\qquad -1 \le u, v, w \le 1 \tag{2.47}$$

where $\mathbf{a}'_u$, $\mathbf{a}'_v$, and $\mathbf{a}'_w$ are reciprocal unitary vectors, and $\{\gamma\}$ are the unknown field-distribution coefficients. As a matter of course, the field expansions satisfy continuity boundary conditions for tangential fields on surfaces shared by adjacent hexahedra in the structure (curl-conforming functions).

Using the Galerkin testing procedure, weighted residuals of (2.43) are formulated as [24]

$$\int_V \mathbf{f}_{\hat{i}\hat{j}\hat{r}} \cdot \nabla \times \mu_r^{-1} \nabla \times \mathbf{E}\, \mathrm{d}V - k_0^2 \int_V \varepsilon_{\mathrm{r}}\, \mathbf{f}_{\hat{i}\hat{j}\hat{r}} \cdot \mathbf{E}\mathrm{d}V = 0, \tag{2.48}$$

where $\mathbf{f}_{\hat{i}\hat{j}\hat{r}}$ can be any of the testing functions for the *u*, *v* and *w* field components, respectively and *V* is the volume of a generalized hexahedron. The vector analogue to Green's first identity can be used to modify the first integral in (2.48) in order to obtain a weak form representation of (2.43) that is suitable for numerical solution [24]:

$$\int_V \mu_{\mathrm{r}}^{-1}(\nabla \times \mathbf{f}_{\hat{i}\hat{j}\hat{r}}) \cdot (\nabla \times \mathbf{E})\, \mathrm{d}V - k_0^2 \int_V \varepsilon_{\mathrm{r}} \mathbf{f}_{\hat{i}\hat{j}\hat{r}} \cdot \mathbf{E}\, \mathrm{d}V = \oint_S \mathbf{f}_{\hat{i}\hat{j}\hat{r}} \times \mu_{\mathrm{r}}^{-1} \nabla \times \mathbf{E} \cdot \mathrm{d}\mathbf{S}, \tag{2.49}$$

where S is the boundary surface of the hexahedron, $\mathrm{d}\boldsymbol{S} = \boldsymbol{n}\cdot\mathrm{d}S$, and $\boldsymbol{n}$ is the outward unit normal. Using Maxwell's first equation, the term on the right-hand side of (2.49) can be represented as [60, p. 51]

$$G_{\hat{i}\hat{j}\hat{r}} = \mathrm{j}k_0\eta_0 \oint_S \mathbf{f}_{\hat{i}\hat{j}\hat{r}} \cdot (\mathbf{n}\times\mathbf{H})\,\mathrm{d}S\,, \tag{2.50}$$

where η_0 is the free-space intrinsic impedance. Substituting the field expansion given by (2.47) into (2.49) on the left-hand side of the equation, only, yields the following FEM matrix equation [60, p. 52]:

$$([A]-k_0^2[B])\cdot\{\gamma\} = \{G\}\,. \tag{2.51}$$

Matrices [A] and [B] are given by [60, p. 52]

$$[A] = \begin{bmatrix} [UUA] & [UVA] & [UWA] \\ [VUA] & [VVA] & [VWA] \\ [WUA] & [WVA] & [WWA] \end{bmatrix}, \qquad [B] = \begin{bmatrix} [UUB] & [UVB] & [UWB] \\ [VUB] & [VVB] & [VWB] \\ [WUB] & [WVB] & [WWB] \end{bmatrix}, \tag{2.52}$$

where the elements of the corresponding submatrices have the form [60, p. 52]

$$UUA_{\hat{i}\hat{j}\hat{r}ijr} = \int_V \mu_{\mathrm{r}}^{-1}(\nabla\times\mathbf{f}_{\hat{i}\hat{j}\hat{r}}^{(u)})\cdot(\nabla\times\mathbf{f}_{ijr}^{(u)})\,\mathrm{d}V\,,\quad UVA_{\hat{i}\hat{j}\hat{r}ijr} = \int_V \mu_{\mathrm{r}}^{-1}(\nabla\times\mathbf{f}_{\hat{i}\hat{j}\hat{r}}^{(u)})\cdot(\nabla\times\mathbf{f}_{ijr}^{(v)})\,\mathrm{d}V\,, \tag{2.53}$$

$$UUB_{\hat{i}\hat{j}\hat{r}ijr} = \int_V \varepsilon_{\mathrm{r}}\mathbf{f}_{\hat{i}\hat{j}\hat{r}}^{(u)}\cdot\mathbf{f}_{ijr}^{(u)}\,\mathrm{d}V\,,\qquad UVB_{\hat{i}\hat{j}\hat{r}ijr} = \int_V \varepsilon_{\mathrm{r}}\mathbf{f}_{\hat{i}\hat{j}\hat{r}}^{(u)}\cdot\mathbf{f}_{ijr}^{(v)}\,\mathrm{d}V\,, \tag{2.54}$$

with analogous expressions for the elements of other submatrices of [A] and [B]. All integrals over the volume of a generalized hexahedron are integrated numerically in the $u-v-w$ domain as [24]

$$\int_V f(u,v,w)\,\mathrm{d}V = \int_u\int_v\int_w f(u,v,w)\,\Im\,\mathrm{d}u\mathrm{d}v\mathrm{d}w\,, \tag{2.55}$$

where integration is carried out using the Gauss-Legendre three-fold integration formula, as in (2.50). Note that, as is the case with the MoM integrals in (2.38) and (2.41), the integrands of FEM integrals are not polynomials in u, v, and w, either.

Due to the continuity of the tangential component of the magnetic field intensity vector, $\mathbf{n} \times \mathbf{H}$, in (2.50) across the interface between any two finite elements in the connected FEM model, the right-hand side terms $\{G\}$ in (2.51) for the connected model contain the surface integral over the overall boundary surface of the entire FEM domain, but not over the internal boundary surfaces between the individual hexahedra in the structure. The tangential component of **H** over the boundary surface of the FEM domain is determined by boundary conditions imposed at the surface. This provides a foundation for a numerical interface between the FEM domain and the remaining space for the modeling of unbounded problems (e.g., antennas and scatterers), i.e., for implementing mesh termination schemes based on absorbing boundary conditions, artificial absorbers, and integral equations [1], [24], [37], [60] all leading to different versions of hybrid FEM methodologies. Alternatively, in the analysis of metallic cavities, boundary conditions require that the tangential component of the electric field intensity vector, **E**, vanish near the cavity walls, which is an example of the simplest mesh termination technique.

2.3. Higher Order Hybrid FEM-MoM

Hybrid finite element-boundary integral (FE-BI) techniques introduce exact BI terminations to numerically truncate and circumscribe the computational modeling domain for unbounded problems (antennas and scatterers) utilizing the finite element method (FEM). Doing so divides the problem into interior and exterior regions. The

electromagnetic field in the interior region, which generally contains inhomogeneous materials, is modeled using an FE differential-equation formulation. The field in the exterior region, which filled with a homogeneous material (usually free space), is represented by some type of BI equations. Then, the fields can be coupled across the FE-BI interface using the appropriate boundary conditions. The system of coupled differential and integral equations is solved using FE and BI numerical discretizations. Since the computational methodologies for the BI correspond to solving surface integral equations (SIEs) based on the method of moments (MoM), the hybrid methods are also known as FEM-MoM techniques.

This section describes the higher order Galerkin-type hybrid FEM-MoM technique for 3-D electromagnetic analysis of arbitrary antennas and scatterers in the frequency domain which is described in detail in reference [37]. The solution in the interior region of the problem is obtained by means of the higher order FEM described in Section 2.2, while the solution in the exterior region is based on the higher order MoM described in Section 2.1, with the two methods being coupled together at the boundary of the interior (FEM) region via boundary conditions.

Consider an electromagnetic system composed of variously shaped metallic and dielectric objects. This system should be excited by a time-harmonic electromagnetic field of complex field intensities $\mathbf{E}^{inc}$ and $\mathbf{H}^{inc}$ with angular frequency ω. This field may consist of a combination of impressed fields from one or more lumped generators, for an antenna structure, or of incident plane waves, for a scattering structure. As the first step of the analysis, the system is decomposed into two sections, as shown in Fig. 2.6: a MoM exterior region, called region *a*, and a FEM interior region, called region *b*.

Generally, multiple FEM and MoM objects can exist within the overall MoM environment. Consequently, homogeneous dielectric domains can be modeled as parts of the FEM region or as MoM objects (using the surface equivalence principle). Similarly, metallic objects, like wires or plates, in the external medium (generally air) can either be modeled as MoM objects, through the use of surface electric currents, or else can be enclosed in a virtual dielectric (air) domain and considered to be a FEM sub-region.

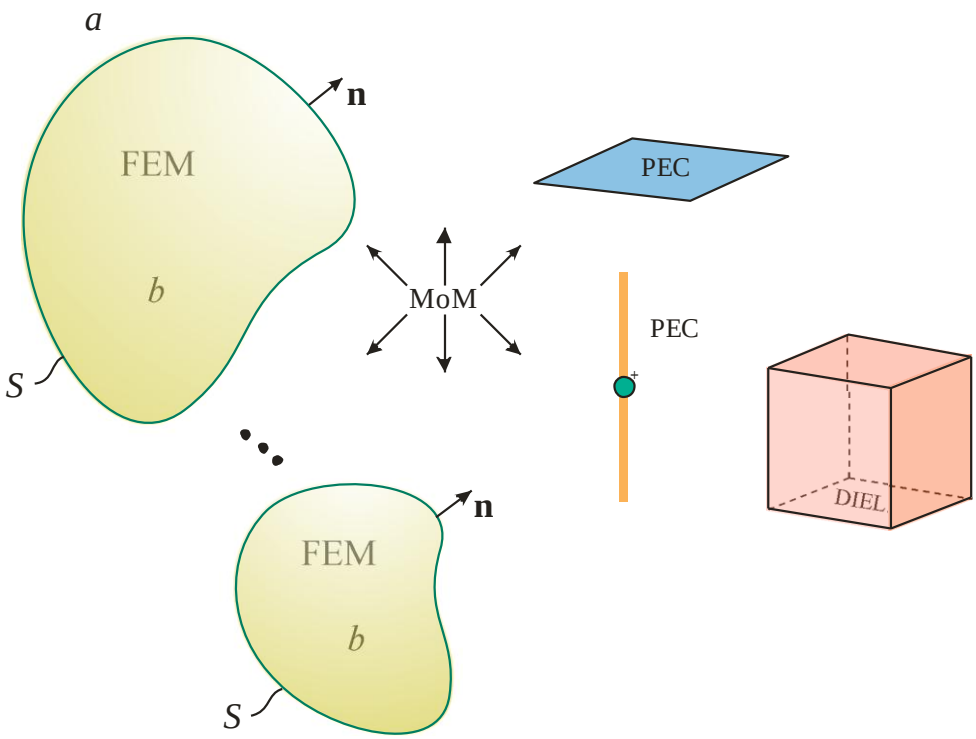

Fig. 2.6. Decomposition of an electromagnetic structure into a MoM (exterior) and a FEM (interior) region, denoted as regions *a* and *b*, respectively [37].

The total electric and magnetic field intensity vectors within region *a*, $\mathbf{E}^a$ and $\mathbf{H}^a$, are formulated in terms of the equivalent surface magnetic current density, $\mathbf{M}_S$, and the equivalent surface electric current density, $\mathbf{J}_S$, that are located on the outer boundaries, surface *S*, of all of the scatterers in region *b*, and the impressed or incident field vectors as

is here shown [37]:

$$\mathbf{E}^a = \mathbf{E}_{\mathrm{J}}(\mathbf{J}_{\mathrm{S}}) + \mathbf{E}_{\mathrm{M}}(\mathbf{M}_{\mathrm{S}}) + \mathbf{E}^{\mathrm{inc}}, \tag{2.56}$$

$$\mathbf{H}^a = \mathbf{H}_{\mathrm{J}}(\mathbf{J}_{\mathrm{S}}) + \mathbf{H}_{\mathrm{M}}(\mathbf{M}_{\mathrm{S}}) + \mathbf{H}^{\mathrm{inc}}, \tag{2.57}$$

where $\mathbf{E}_{\mathrm{M}}$ and $\mathbf{H}_{\mathrm{M}}$ stand for the scattered electric and magnetic field vectors due to current $\mathbf{M}_{\mathrm{S}}$, while $\mathbf{E}_{\mathrm{J}}$ and $\mathbf{H}_{\mathrm{J}}$ are the scattered fields due to $\mathbf{J}_{\mathrm{S}}$, and they are computed using (2.5)-(2.14). Fields $\mathbf{E}^a$ and $\mathbf{H}^a$ are coupled to corresponding field vectors within region *b*, $\mathbf{E}^b$ and $\mathbf{H}^b$, by means of boundary conditions for the tangential field components on the surface *S* [37],

$$(\mathbf{E}^a)_{\tan} = (\mathbf{E}^b)_{\tan}, \tag{2.58}$$

$$(\mathbf{H}^a)_{\tan} = (\mathbf{H}^b)_{\tan} = \mathbf{J}_{\mathrm{S}} \times \mathbf{n}, \tag{2.59}$$

where **n** is the outward unit normal from *S*. Combined with (2.1) and (2.2), we find that

$$-[\mathbf{E}_{\mathrm{J}}(\mathbf{J}_{\mathrm{S}})]_{\tan} - [\mathbf{E}_{\mathrm{M}}(\mathbf{M}_{\mathrm{S}})]_{\tan} + (\mathbf{E}^b)_{\tan} = (\mathbf{E}^{\mathrm{inc}})_{\tan}, \tag{2.60}$$

$$-[\mathbf{H}_{\mathrm{J}}(\mathbf{J}_{\mathrm{S}})]_{\tan} - [\mathbf{H}_{\mathrm{M}}(\mathbf{M}_{\mathrm{S}})]_{\tan} + \mathbf{J}_{\mathrm{S}} \times \mathbf{n} = (\mathbf{H}^{\mathrm{inc}})_{\tan}, \tag{2.61}$$

which provides the computational interface between the FEM and MoM regions, where the field $\mathbf{E}^b$ within region *b* (the FEM region) and the currents $\mathbf{J}_{\mathrm{S}}$ and $\mathbf{M}_{\mathrm{S}}$ over *S* are unknowns [37].

In the FEM-MoM discretization procedure, $\mathbf{J}_{\mathrm{S}}$ and $\mathbf{M}_{\mathrm{S}}$ are represented as in (2.30), with a total of $2N_{\mathrm{MoM}}$ unknown current-distribution coefficients $\{\alpha\}$ and $\{\beta\}$ on the FEM-MoM interface, and $\mathbf{E}^b$ is given by (2.47), with a total of N_{FEM} unknown field-distribution coefficients $\{\gamma\}$. Since there is such an exact compatibility between volume and surface geometrical elements, as well as field and current approximations, the hybridization of the two methods is occurs in a true higher order fashion, in regards to both field/current

and geometrical modeling in both the FEM and MoM regions. Additionally, the modeling flexibility and computational efficiency of the hybrid method is further enhanced by the hierarchical nature of both techniques.

To solve for the coefficients $\{\gamma\}$ in the FEM region of the model, the matrix form of the FEM equation is found by substituting the expansion (2.47) into (2.49) [24], on its left-hand side, and (2.9) and the first expansion in (2.30) into (2.50), namely, on the right-hand side of (2.49), so which results in [37]

$$[FEM_{kl}]\{\gamma_l\} = [C_{kj}]\{\alpha_j\}, \quad [FEM] = [A] - k_0^2[B] \ , \tag{2.62}$$

where the elements of matrices [*A*] and [*B*] are those in (2.52)-(2.54). The matrix [*C*] in (2.62) is given by [37]

$$[C_{kj}] = \mathrm{j}k_0\eta_0[<\mathbf{e}_k, \mathbf{j}_{\mathrm{S}_j}>], \tag{2.63}$$

where the inner product of the FEM and MoM basis functions is

$$<\mathbf{e}_k, \mathbf{j}_{\mathrm{S}_j}> = \oint_S \mathbf{e}_k \cdot \mathbf{j}_{\mathrm{S}_j} \mathrm{d}S \, . \tag{2.64}$$

On the other side, the Galerkin discretization of (2.48) and (2.49), together with the testing and basis functions in (2.30), results in a SIE matrix equation over the FEM-MoM interface (surface *S*) [37],

$$\begin{bmatrix} -<\mathbf{j}_{\mathrm{S}_i}, \mathbf{E}_{\mathrm{J}}(\mathbf{j}_{\mathrm{S}_j})> + <\mathbf{j}_{\mathrm{S}_i}, \mathbf{E}^b(\mathbf{j}_{\mathrm{S}_j})> & -<\mathbf{j}_{\mathrm{S}_i}, \mathbf{E}_{\mathrm{M}}(\mathbf{j}_{\mathrm{S}_j})> \\ -<\mathbf{j}_{\mathrm{S}_i}, \mathbf{H}_{\mathrm{J}}(\mathbf{j}_{\mathrm{S}_j})> + <\mathbf{j}_{\mathrm{S}_i}, \mathbf{j}_{\mathrm{S}_j} \times \mathbf{n}> & -<\mathbf{j}_{\mathrm{S}_i}, \mathbf{H}_{\mathrm{M}}(\mathbf{j}_{\mathrm{S}_j})> \end{bmatrix} \begin{bmatrix} \{\alpha_j\} \\ \{\beta_j\} \end{bmatrix} = \begin{bmatrix} <\mathbf{j}_{\mathrm{S}_i}, \mathbf{E}^{\mathrm{inc}}> \\ <\mathbf{j}_{\mathrm{S}_i}, \mathbf{H}^{\mathrm{inc}}> \end{bmatrix}, \tag{2.65}$$

which can be represented as [37]

$$\begin{bmatrix} [-Z_{ij}^{ee} + <\mathbf{j}_{\mathrm{S}_i}, \mathbf{E}^b(\mathbf{j}_{\mathrm{S}_j})>] & [-Z_{ij}^{em}] \\ [-Z_{ij}^{me} + <\mathbf{j}_{\mathrm{S}_i} \times \mathbf{j}_{\mathrm{S}_j}, \mathbf{n})>] & [-Z_{ij}^{mm}] \end{bmatrix} \begin{bmatrix} \{\alpha_j\} \\ \{\beta_j\} \end{bmatrix} = \begin{bmatrix} \{v^e\}^{\mathrm{inc}} \\ \{v^m\}^{\mathrm{inc}} \end{bmatrix}. \tag{2.66}$$

In (2.66), all of the terms can be readily solved for with the exception of $\mathbf{E}^b(\mathbf{j}_{S_j})$, which we can obtain as follows using (2.47) and (2.62) [37]:

$$\mathbf{E}^b(\mathbf{j}_{S_j}) = \sum_{l=1}^{N_{\text{FEM}}} \gamma_l^{\hat{j}}\, \mathbf{e}_l = \{\gamma_l^{\hat{j}}\}^{\text{T}}\{\mathbf{e}_l\}, \tag{2.67}$$

$$\{\gamma_l^{\hat{j}}\} = [FEM_{kl}]^{-1}\{C_{k\hat{j}}\}, \tag{2.68}$$

where (2.67) and (2.68) are computed for all values of $\hat{j}$ from 1 to N_{MoM}, and $\{C_{k\hat{j}}\}$ (with a fixed $j = \hat{j}$) stands for the $\hat{j}$-th column of $[C_{kj}]$.

Hierarchical higher order basis functions in (2.47) have poor orthogonality properties, which results in FEM matrices, in (2.68), having large condition numbers, as well as related problems, particularly when using iterative solvers. However, there is often an order of magnitude reduction in the number of unknowns between high and low order FEM matrices. Consequently, as the higher order FEM matrices are much smaller than their low order counterparts, they can be effectively factored using direct sparse factorization techniques and sparse storage algorithms, which are not so sensitive to matrix condition numbers [24], [26]. Note also that [*FEM*] in (2.68) only needs to be factored once, following which the coefficients in (2.68) and fields in (2.67) can be calculated one by one using a fast back-substitution procedure. Overall, direct factorization of the FEM matrix provides an effective solution in the context of the higher order discretization. On the other hand, if the matrix equation is to be solved by an iterative procedure and there is a very large number of unknowns, alternative higher order hierarchical basis functions with improved orthogonality and conditioning properties constructed from Legendre polynomials [24-25] may be utilized to accelerate the solution

procedure. Finally, note that, provided that μ_r and ε_r are frequency independent (dispersionless media), the FEM matrix elements in (2.24) depend on frequency only through k_0^2. This allows the elements of the matrix to be calculated only once, valid for the entire frequency range of interest, and then stored separately as matrices [*A*] and [*B*], from which [*FEM*] can be reconstructed, according to (2.24), for any given frequency. If μ_r and ε_r are frequency dependent, but are also spatially constant within any given FEM element (homogeneous medium in the element), they can be moved in front of the integrals in (2.25) and a similar algorithm can be applied. Using multifrequency solution acceleration procedures such as this significantly reduces the overall computational time by allowing the global FEM matrix to be filled only once, at the expense of requiring a considerably larger storage space be allocated, since matrices [*A*] and [*B*] must be stored separately; this is a worthwhile tradeoff given that the sparse storage scheme is employed, that the numbers of unknowns are generally small, and that, when necessary, matrices can be stored out-of-core without a significant recovery time loss.

Once all $\mathbf{E}^b(\mathbf{j}_{S_j})$ terms are calculated, the MoM matrix in (2.66) can be completed and the system solved for the unknown current distribution coefficients $\{\alpha\}$ and $\{\beta\}$, that is, by way of expansions (2.30), for the MoM surface currents $\mathbf{J}_S$ and $\mathbf{M}_S$ on *S*. Exterior fields in the MoM region can then be found using (2.4)-(2.14). Finally, the FEM field coefficients $\{\gamma\}$ can be obtained using (2.62) [37],

$$\{\gamma_l\} = [FEM_{kl}]^{-1}[C_{kj}]\{\alpha_j\}, \tag{2.69}$$

and the interior electric field (within the FEM region) can be evaluated by means of its expansion (2.47).

3. PROCEDURE FOR DETERMINING OPTIMAL HIGHER ORDER MODELING PARAMETERS THROUGH NUMERICAL EXPERIMENTS

We investigate the behavior of higher order MoM-SIE and FEM-MoM numerical solutions by running an exhaustive series of electromagnetic simulations of several canonical models of metallic and dielectric scatterers, in which we systematically vary the key higher order modeling parameters: number of elements in the model, M (h-refinement), or, equivalently, numbers of subdivisions per edge, H_u, H_v, and H_w, of initially used elements, polynomial orders of basis (and testing) functions, N_u, N_v, and N_w in (2.30) and (2.47) (p-refinement), orders of Gauss-Legendre integration formulas, i.e., numbers of integration points, NGL_u, NGL_v, and NGL_w in (2.42) to solve integrals in (2.38) and (2.41) (integration accuracy), and geometrical orders of elements, namely, orders of Lagrange-type curvature in the model, K_u, K_v, and K_w in (2.26) and (2.44) (when curved elements are employed).

However, the combinatorial space of the adopted key parameters is enormously vast and technically ungraspable, particularly when one takes into account that all of the parameters can generally be changed anisotropically along the element (quadrilateral or hexahedron) edges. Hence, in the study, we limit this space by using only elements with

isotropic polynomial orders, $N_u = N_v = N$ for MoM quadrilaterals and $N_u = N_v = N_w = N$ for FEM hexahedra, and similarly $NGL_u = NGL_v = NGL$ for quadrilaterals and $NGL_u = NGL_v = NGL_w = NGL$ for hexahedra, as well as $K_u = K_v = K$ and $K_u = K_v = K_w = K$, respectively. In addition, meshes in all examples are refined isotropically in all directions: the initial, roughest, geometrical mesh is equally subdivided along all edges in the *h*-refinement process ($H_u = H_v = H_w = H$). Finally, the same set of parameters is adopted (and then equally varied) in all elements in a model. These restrictions impose the utilization of simple symmetric structures to be analyzed as EM models for the given purpose. Hence, the structures to be modeled and simulated are chosen to be metallic and homogeneous dielectric cubical and spherical scatterers, respectively. Nonetheless, the number of simulations (and obtained results) with systematically varying (i) the number of edge divisions from $H = 1$ to $H = 3$, (ii) polynomial orders of basis (and testing) functions from $N = 1$ to $N = 10$, and (iii) orders of Gauss-Legendre formulas from $NGL = 2$ to $NGL = 20$, as well as (iv) using the curvature orders (for spheres) of $K = 2$ and $K = 4$, respectively, is still extremely large and entirely sufficient for drawing the desired conclusions.

In higher order computational models, we define the model mesh complexity by referring to the number of quadrilateral patches on the structure side, $E = H \times H$. For instance, a cube or a sphere modeled by only one patch per side is defined by $E = 1 \times 1$, which results in a total of $6 \times 1 \times 1 = 6$ patches (and $1 \times 1 \times 1 = 1$ FEM element in the FEM-MoM model). The refined mesh determined by $E = 2 \times 2$ is the one with initial side patches divided into 2×2 quadrilaterals, yielding a total of $6 \times 2 \times 2 = 24$ patches (the corresponding number of FEM elements in such a mesh would be $2 \times 2 \times 2 = 8$). Similarly,

an $E = 3\times3$ model has $6\times3\times3$ patches. Additionally, cube side length and sphere radius for the considered scatterers are both set to $a = 1$ m and the relative dielectric permittivity of dielectric scatterers is adopted to be $\varepsilon_r = 4$ in all examples and experiments. When referring to the electrical size of the model, we consider a/λ_0 for metallic and a/λ for dielectric scatterers, where λ_0 and λ are the wavelengths in free space and in the dielectric of the object, respectively. Finally, we adopt only single machine precision for all computations, having in mind, however, that this is one of the key limiting factors for both accuracy and convergence with *h*-, *p*-, and integral accuracy refinements, and that quantitative recipes for adoptions of optimal higher order modeling parameters would be different in double (or higher) precision.

Cubical scatterers (metallic and dielectric) are excellent benchmarking choices because their geometry can be modeled exactly, thus eliminating the geometrical error from the numerical solution. They are attractive for evaluation of numerical methods also because of their sharp edges and corners, in the vicinity of which the fields and currents exhibit singular, and challenging to model and capture, behavior. Although analytical solutions do not exist for these models, experimental results and highly accurate numerical solutions (carefully checked for convergence in a considered frequency range), obtained by one of the industry's leading commercial software tools for full wave EM analysis – WIPL-D, is used for validations and comparisons. Spherical scatterers, on the other hand, are excellent evaluation and benchmarking models because the analytical solutions for them exist in the form of Mie's series, allowing exact validation of numerical solutions and rigorous judging of the numerical accuracy. Additionally, they are objects with pronounced curvature, which is always a challenge for modeling from the geometrical

point of view (in fact, spheres are customarily taken as examples of difficulties with modeling of curvature by many researchers). Spherical scatterers are therefore convenient for analysis of higher order solutions involving curved large-domain Lagrange-type quadrilaterals and hexahedra.

The direct solution to EM (scattering) problems analyzed by the MoM-SIE technique is the (equivalent) surface current distribution on the scatterer surface(s). The quality of the solution can thus be most naturally (from the mathematical point of view) judged by examining an error associated with the current distribution (e.g., in an average or an RMS sense). However, in this study, we take a more practical approach and adopt the radar cross-section (RCS), which is most frequently the quantity of interest that is measured and simulated in real EM scattering applications, to be the quantity of choice for our assessment of the solution accuracy. We also construct a simple metric, the absolute RCS error in dB, for error evaluation. We evaluate the absolute RCS error in FEM-MoM computations as well.

To cope with the still abundantly large number of possible parameter variations and experimentation scenarios, we adopt the following systematic analysis procedure and strategy. In all examples, we start with the simplest model ($E = 1\times1$) and analyze (a) the absolute monostatic RCS error, computed as $|RCS_{\text{numerical}} - RCS_{\text{reference}}|$ in dB, for a fixed high *NGL* (*NGL* = 20) vs. the model electrical size and (b) the average absolute RCS error, averaged over multiple electrical sizes of elements in a reasonable frequency range, where the elements are electrically small enough to yield accurate solutions, vs. *NGL*. Both analyses are carried out for a series of polynomial orders *N*, and respective families of curves are generated. In analysis of the error vs. the model size [analysis (a)], we seek,

for every N, the a/λ (or a/λ_0) limit for which the model yields a solution with an error not significantly higher than 0.1 dB (in graphs, we truncate the error curves when the error becomes much higher than 1 dB – for the clarity of the graph) and note how this limit increases with increasing N (p-refinement). In analysis of the average error vs. *NGL* [analysis (b)], we seek the optimal N, for which the average error is small enough (below 0.1 dB) and does not improve much with further p-refinement, and the corresponding *NGL*. We consider the accuracy of RCS simulation results with an error lower than 0.1 dB to be excellent in terms of practical relevance, since the minimum uncertainty (error) in RCS measurements and calibrations is almost never at or below the 0.2 dB level [68-70], and the errors lower than 0.1 dB are practically undetectable. In other words, based on the obtained results, we draw conclusions about the convergence of the results with increasing N (p-refinement), maximum electrical size of the elements, e (in terms of λ or λ_0), that can be analyzed using sufficiently high N (beyond which h-refinement should be performed), the highest N that can be reasonably used, and the optimal N and *NGL*. We then h-refine the model mesh and repeat the procedure. For spheres, we go through the same steps using curved Lagrange-type elements with fixed $K = 2$ and $K = 4$, respectively. Finally, we perform higher order RCS analysis of the NASA almond [71], which is an EMCC (Electromagnetic Code Consortium) benchmark target and one of the most popular benchmarking examples for both research and commercial CEM codes.

4. NUMERICAL RESULTS AND DISCUSSION: OPTIMAL MODELING PARAMETERS AND PARAMETER LIMITS

4.1. Optimal Higher Order Modeling Parameters for MoM-SIE Scattering Analysis of a Metallic Cube

We first present the higher order MoM-SIE scattering analysis of a metallic (PEC) cube (with a = 1 m), starting with the simplest model ($E = 1\times1$) of the scatterer. Based on the results in Fig. 4.2, we conclude that the model is accurately simulated up to a limit of $a/\lambda_0 = 2$ (element edge size amounts to $e = 2\lambda_0$) using $N = 6$ or (depending on the desired accuracy level) up to $a/\lambda_0 = 3$ with $N = 7$, and that even a model as large as $a/\lambda_0 = 3.5$ in electrical size of the element edge may be considered to be usable (for some engineering applications) if $N = 8$ is employed. From Fig. 4.3, where, for the average error, we take into account the conservative maximum element size (before h-refinement) of $e = 2\lambda_0$, we realize (looking at the "knee" points of the curves) that $NGL = N + 2$ is optimal for all orders N (N = 5, 6, 7, and 8) providing very accurate results (error smaller than 0.1 dB). Orders $N > 8$ are not recommended as they do not yield better results – they neither significantly increase the analyzable model size nor improve the average accuracy of the solution in the reasonable frequency range. Based on all of the above, we select the overall optimal choice of parameters to be $N = 6$ and $NGL = 8$ (for $e = 2\lambda_0$), and compute

and plot the normalized RCS in Fig. 4.4, where we also plot the results for $N = 8$ and $NGL = 10$ for the less conservative maximum element size ($e = 3\lambda_0$), as well as the measured RCS [72]. If elements smaller than optimal have to be used, which may be mandated by the geometrical or material complexity of the structure under consideration, the optimal polynomial orders are reduced by one for every reduction of the element size by $0.5\lambda_0$; for instance, based (preliminary) on Fig. 4.2, $N = 5$ is optimal for $\lambda_0 < e \leq 1.5\lambda_0$, while $N = 4$ is the best choice if $0.5\lambda_0 < e \leq \lambda_0$ (this will be explored more in studies with *hp*-refinements).

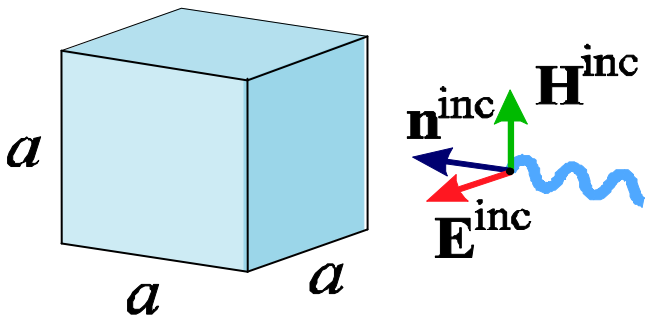

Fig. 4.1. Higher order MoM-SIE scattering analysis of a metallic cube with $E = 1\times1$ ($K = 1$).

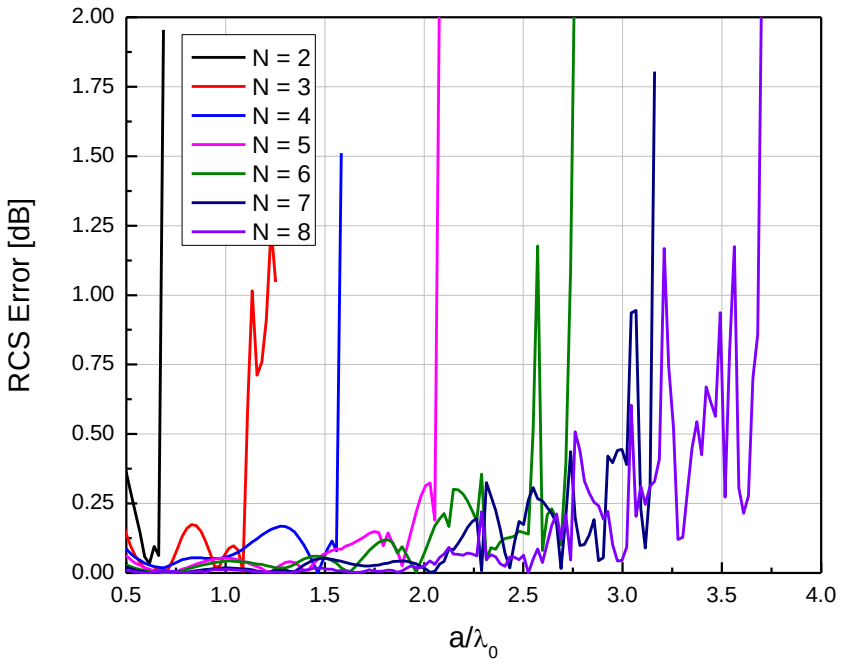

Fig. 4.2. Higher order MoM-SIE scattering analysis of a metallic cube with $E = 1\times1$ ($K = 1$): absolute RCS error for $NGL = 20$ and a series of orders N (p-refinement) vs. the model electrical size.

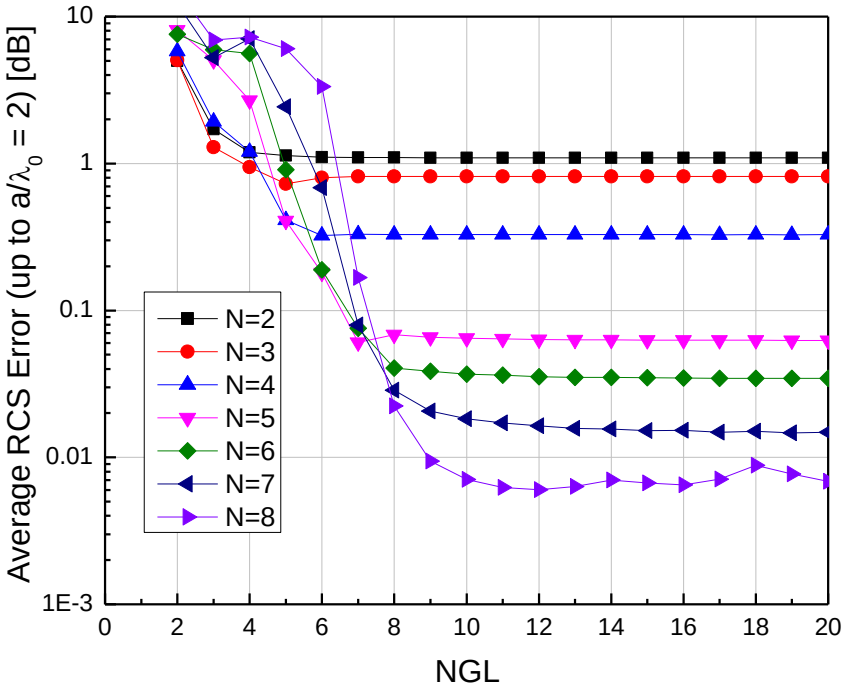

Fig. 4.3. Higher order MoM-SIE scattering analysis of a metallic cube with $E = 1\times1$ ($K = 1$): absolute RCS error averaged over multiple values of a/λ_0 in a frequency range corresponding to reasonable model sizes, $a/\lambda_0 \leq 2$ (conservative maximum model size), with a series of N values vs. NGL.

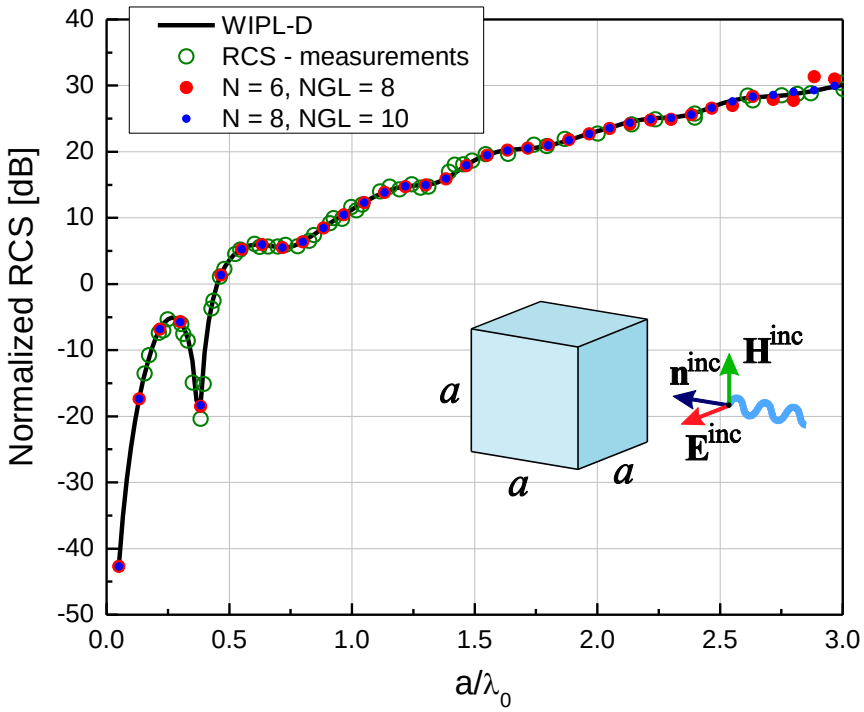

Fig. 4.4. Higher order MoM-SIE scattering analysis of a metallic cube with $E = 1\times1$ ($K = 1$): the optimal solution ($N = 6$ and $NGL = 8$ for $e = 2\lambda_0$), along with the results for $N = 8$ and $NGL = 10$ (for $e = 3\lambda_0$) and measured data [72].

We then *h*-refine the cube model mesh to $E = 2\times2$ and repeat the procedure. From the results in Fig. 4.6, we see that the model is accurately analyzed up to $a/\lambda_0 = 4$ ($e = 2\lambda_0$) using $N = 6$, and even to $a/\lambda_0 = 6$ ($e = 3\lambda_0$) with $N = 8$. Based on Fig. 4.7, we conclude that – for $N = 5$, 6, 7, and 8 – $NGL = N + 2$ is optimal ("knees" of curves"), as well as that the optimal polynomial order is again $N = 6$ (with $NGL = 8$), while orders $N = 9$ and higher are not recommended. The normalized RCS for the more conservative ($N = 6$, $e = 2\lambda_0$) and less conservative ($N = 8$, $e = 3\lambda_0$) optimal solutions is shown in Fig. 4.8.

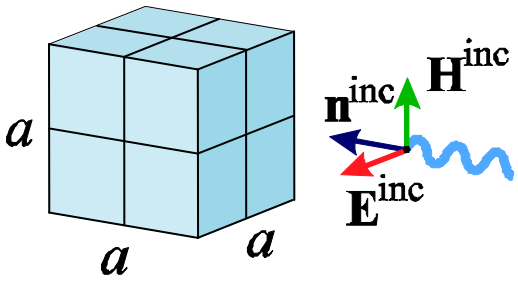

Fig. 4.5. MoM-SIE analysis of a metallic cube with E = 2×2.

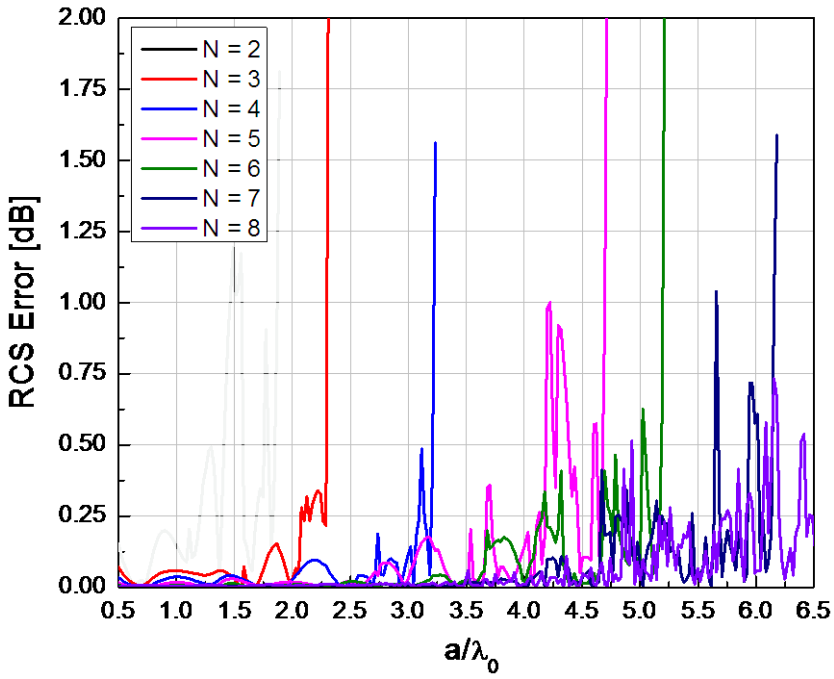

Fig. 4.6. MoM-SIE analysis of a metallic cube with E = 2×2: RCS error for NGL = 20 and p-refinement.

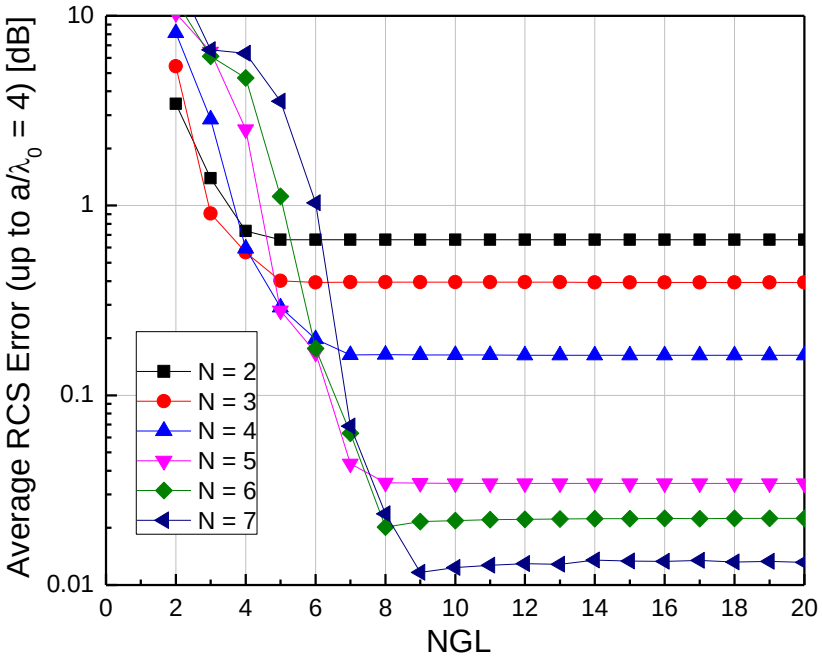

Fig. 4.7. MoM-SIE analysis of a metallic cube with $E = 2\times2$: average RCS error for reasonable model sizes, $a/\lambda_0 \leq 4$, with *p*-refinement vs. *NGL*.

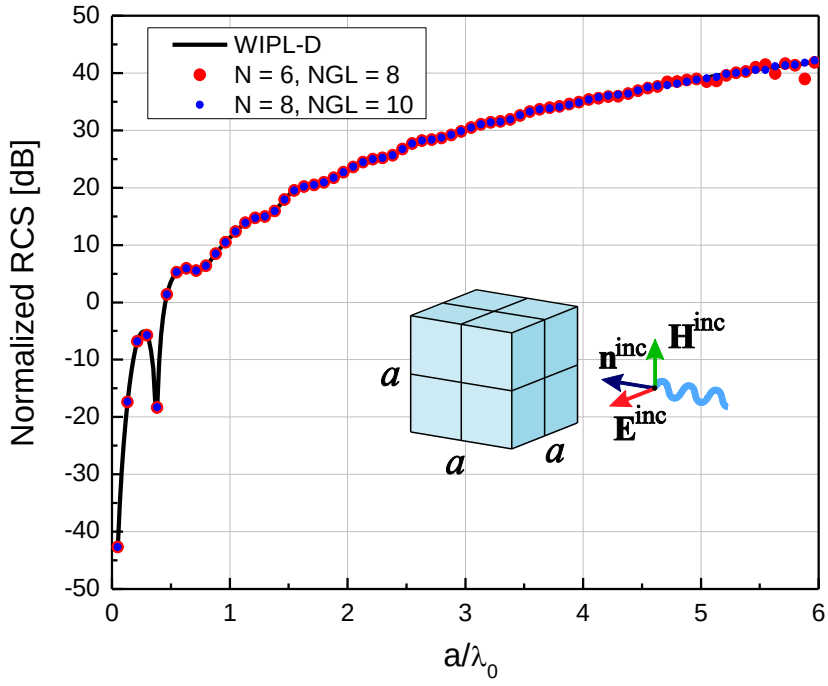

Fig. 4.8. MoM-SIE analysis of a metallic cube with $E = 2\times2$: (c) the optimal solution for both $N = 6$ ($e = 2\lambda_0$) and $N = 8$ ($e = 3\lambda_0$).

Finally, for $E = 3\times3$, the results in Fig. 4.10 tell us that the model is accurate up to $a/\lambda_0 = 6$ ($e = 2\lambda_0$) for $N = 6$, and even higher (for $N = 7$). From Fig. 4.11, $NGL = N + 2$ is optimal, for $N = 5$, 6, and 7, and the optimal N, for $e = 2\lambda_0$, comes out to be $N = 6$ (with $NGL = 8$). Fig. 4.12 shows the optimal solution for both $e = 2\lambda_0$ and $e = 3\lambda_0$. In addition, Fig. 4.13 tells us that if elements up to $e = 0.5\lambda_0$ in size are used, orders $N = 2$ or 3 provide accurate results, $N = 3$ or 4 suffices, based on Fig. 4.14, for $e \leq \lambda_0$, and $N = 4$ or 5 should be used if the maximum element size in the model is $e = 1.5\lambda_0$, Fig. 4.15, where, in all cases, $NGL = N + 2$ ("knee" points of the curves) is the optimal choice.

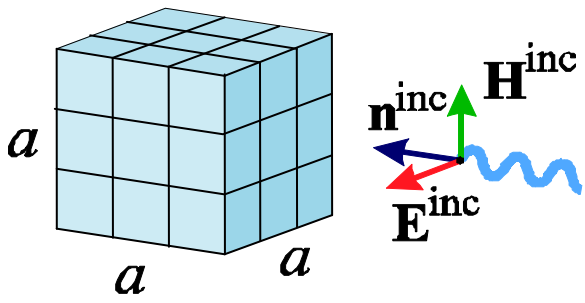

Fig. 4.9. MoM-SIE simulations of a metallic cube with $E = 3\times3$.

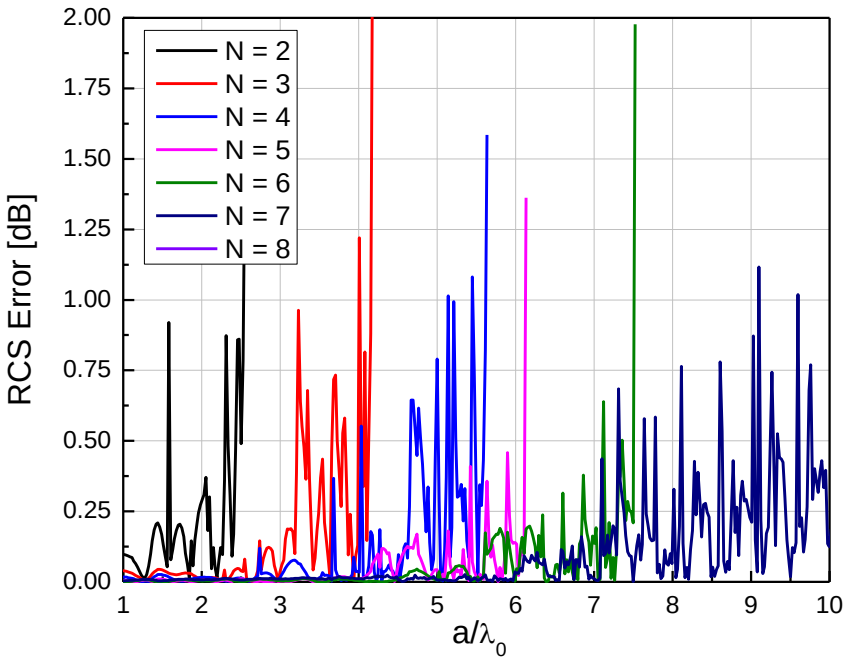

Fig. 4.10. MoM-SIE simulations of a metallic cube with $E = 3\times3$: RCS error vs. a/λ_0 ($NGL = 20$).

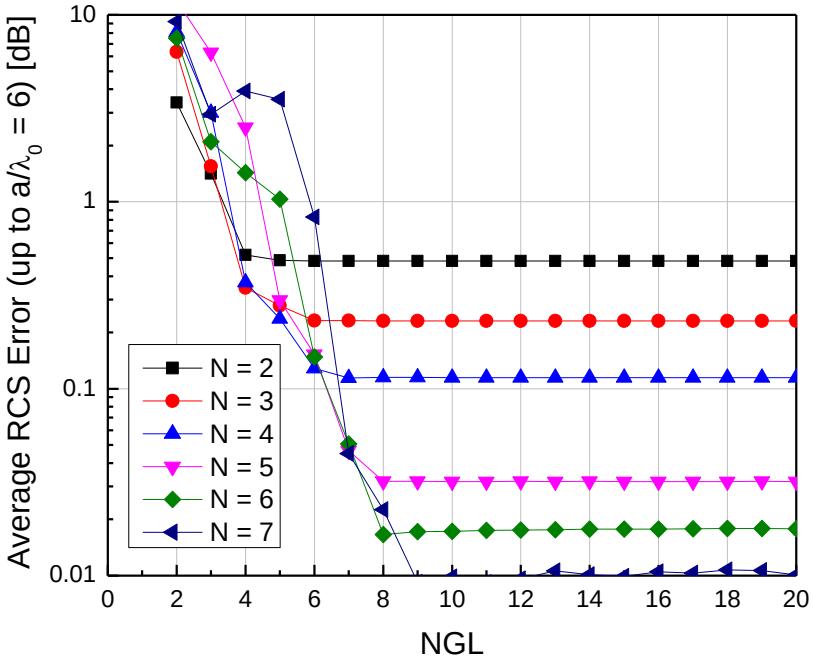

Fig. 4.11. MoM-SIE simulations of a metallic cube with $E = 3\times3$: RCS error averaged over reasonable model sizes up to $a/\lambda_0 = 6$ or $e = 2\lambda_0$ (conservative choice).

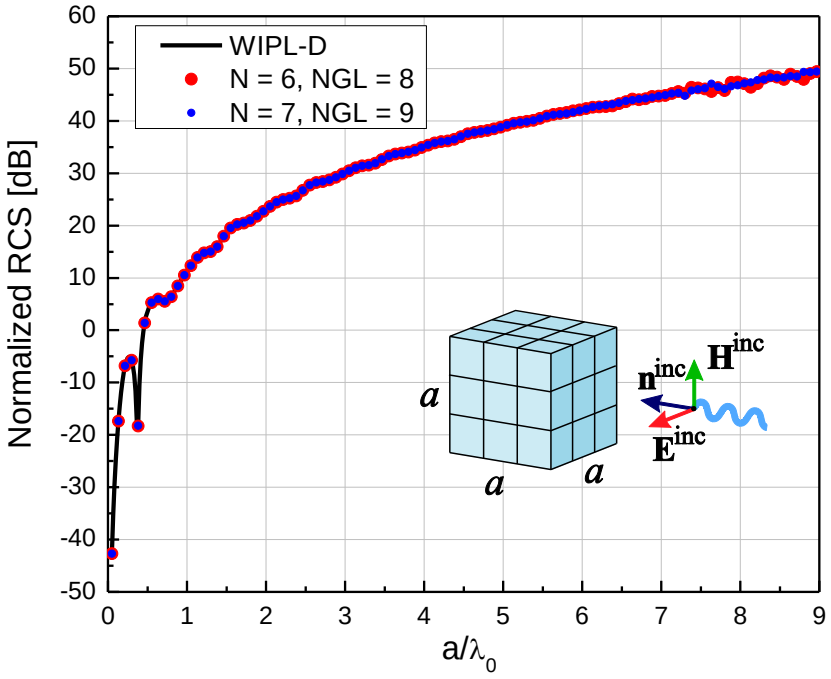

Fig. 4.12. MoM-SIE simulations of a metallic cube with $E = 3\times3$: the optimal solution (for both $e = 2\lambda_0$ and $e = 3\lambda_0$).

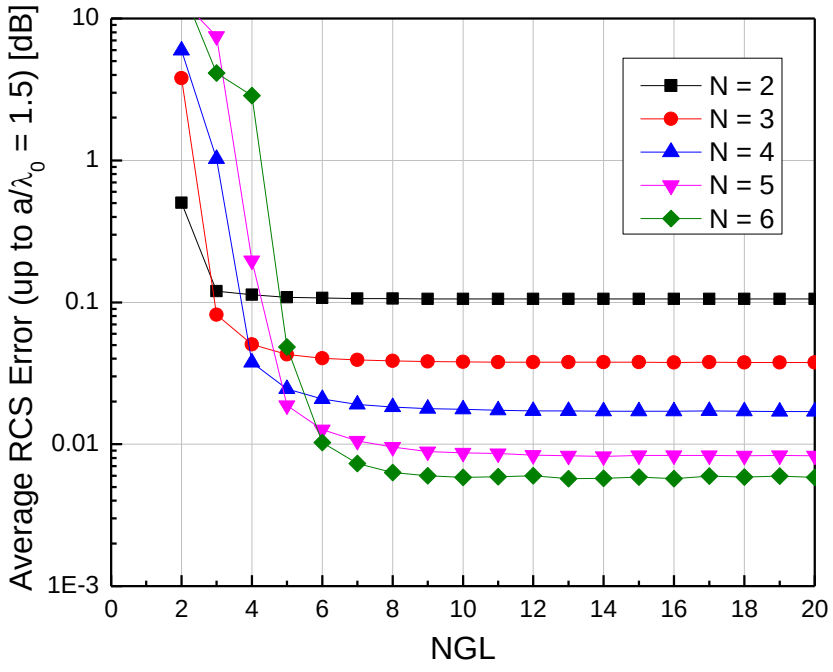

Fig. 4.13. Average RCS error in the MoM-SIE analysis of a metallic cube with $E = 3\times3$ for $e \leq 0.5\lambda_0$.

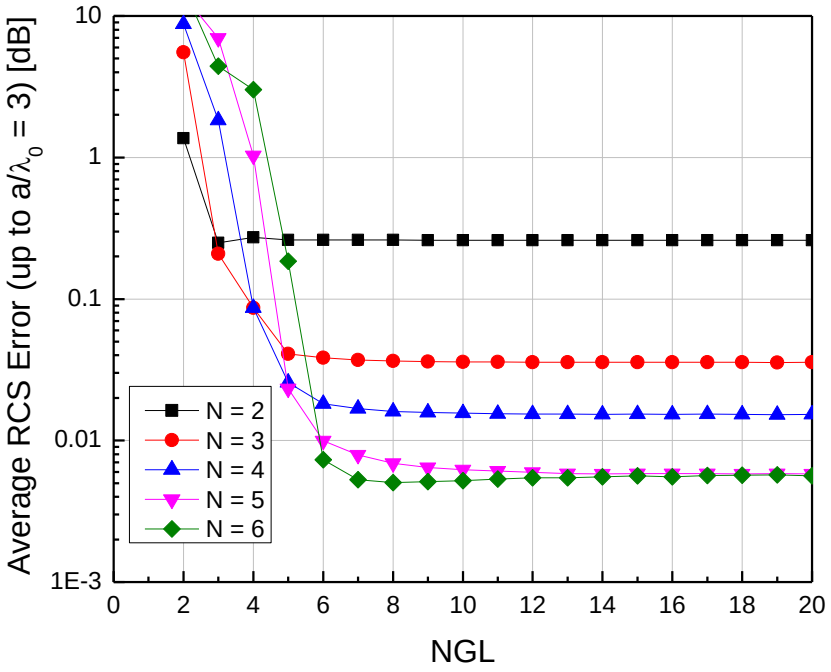

Fig. 4.14. Average RCS error in the MoM-SIE analysis of a metallic cube with E = 3×3 for $e \leq \lambda_0$.

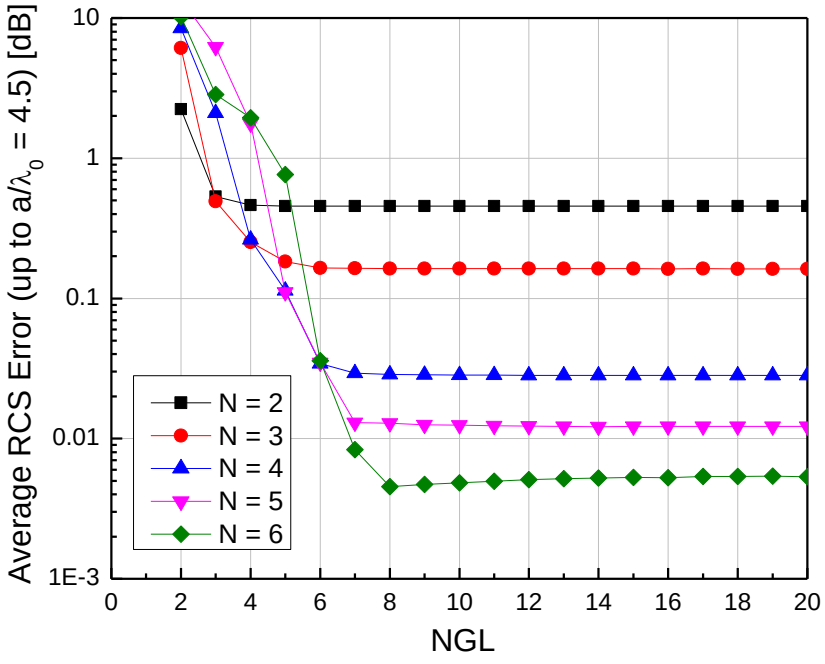

Fig. 4.15. Average RCS error in the MoM-SIE analysis of a metallic cube with E = 3×3 for $e \leq 1.5\lambda_0$.

General conclusions for the higher order MoM-SIE scattering analysis of a metallic cube are that the optimal (or nearly optimal) choice of polynomial orders of basis and testing functions and orders of Gauss-Legendre integration formulas is given by $N = 6$ and $NGL = 8$, respectively. The mesh should be *h*-refined if the element edge size becomes greater than $e = 2\lambda_0$ (conservative option). If elements smaller than optimal are to be used, the optimal polynomial orders are $N = 2$ for $e \leq 0.25\lambda_0$, $N = 3$ for $0.25\lambda_0 < e \leq 0.5\lambda_0$, $N = 4$ for $0.5\lambda_0 < e \leq \lambda_0$, $N = 5$ for $\lambda_0 < e \leq 1.5\lambda_0$, and $N = 6$ for $1.5\lambda_0 < e \leq 2\lambda_0$. Hence, the minimum average total number of unknowns [the number of coefficients $\{\alpha\}$ in (3), for the whole model] per wavelength for accurate RCS analysis amounts approximately to 11.3 if $N = 2$ is used, to 8.5 if $N = 3$, to 5.7 for $N = 4$, to 4.7 for $N = 5$, and to 4.2 if $N = 6$ is implemented in the model. Orders $N > 8$ are not recommended to be used (*h*-refinement should be performed instead). It is generally optimal to use $NGL = N + 2$ for any N. It is generally not recommended to increase NGL any further, except in order to verify the solution stability.

4.2. Optimal Higher Order Modeling Parameters for MoM-SIE Scattering Analysis of a Dielectric Cube

Next, we carry out the numerical investigation of higher order modeling parameters in the MoM-SIE analysis of a dielectric cube scatterer (with $a = 1$ m and $\varepsilon_r = 4$). For the simplest model ($E = 1\times1$), results in Fig. 4.17 indicate that the computation is accurate up to $a/\lambda = 2$ (element edge size is $e = 2\lambda$) using $N = 5$ or 6, while adoption of a larger N can extend the analyzable size even further. According to Fig. 4.18, we realize that the

polynomial orders N = 5 or 6 are optimal, for $NGL = N + 2$ (see the "knee" points of the curves), while orders N = 7 and higher are not recommended. The normalized RCS of the cube using the optimal set of parameters N = 6 and NGL = 8 is shown in Fig. 4.19.

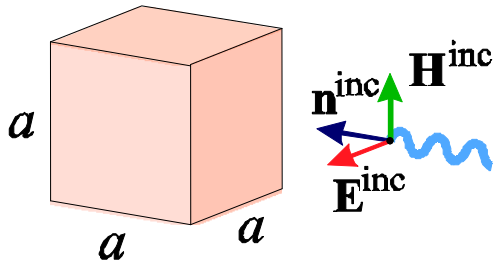

Fig. 4.16. Higher order MoM-SIE computation of a dielectric cube scatterer with E = 1×1.

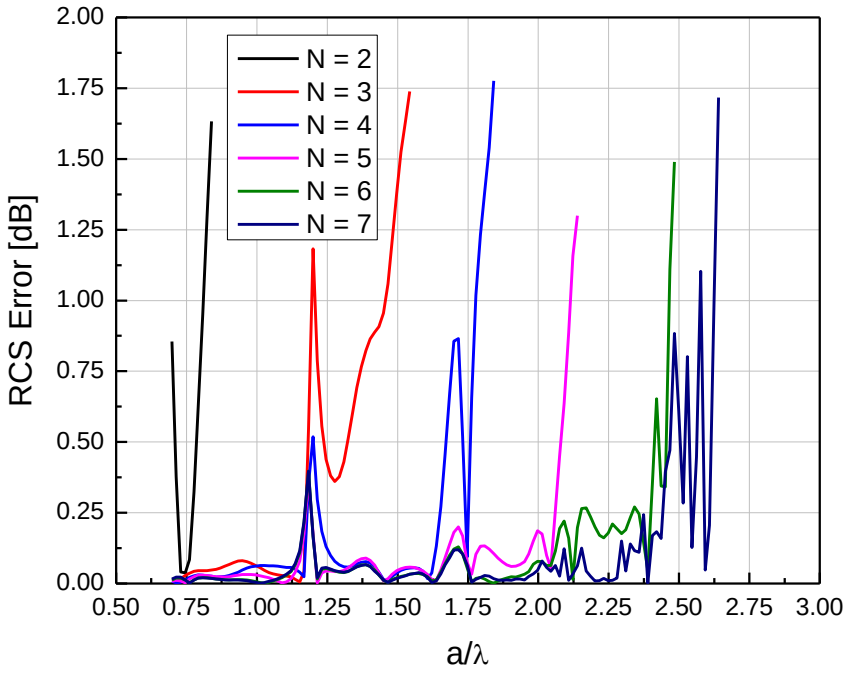

Fig. 4.17. Higher order MoM-SIE computation of a dielectric cube scatterer with E = 1×1: absolute RCS error for NGL = 20 and p-refinement vs. the model electrical size.

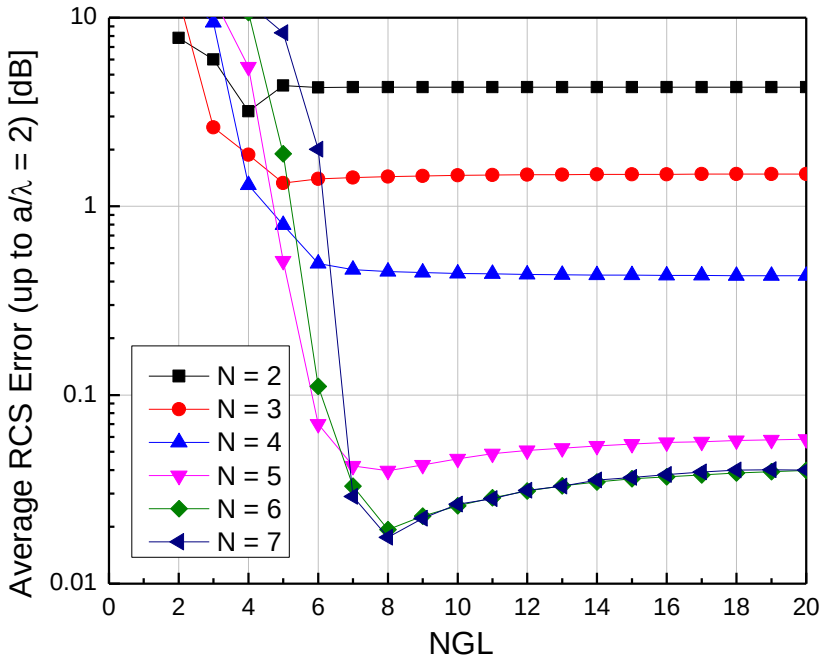

Fig. 4.18. Higher order MoM-SIE computation of a dielectric cube scatterer with $E = 1\times1$: absolute RCS error averaged over multiple reasonable model sizes, $a/\lambda \leq 2$, with *p*-refinement vs. *NGL*.

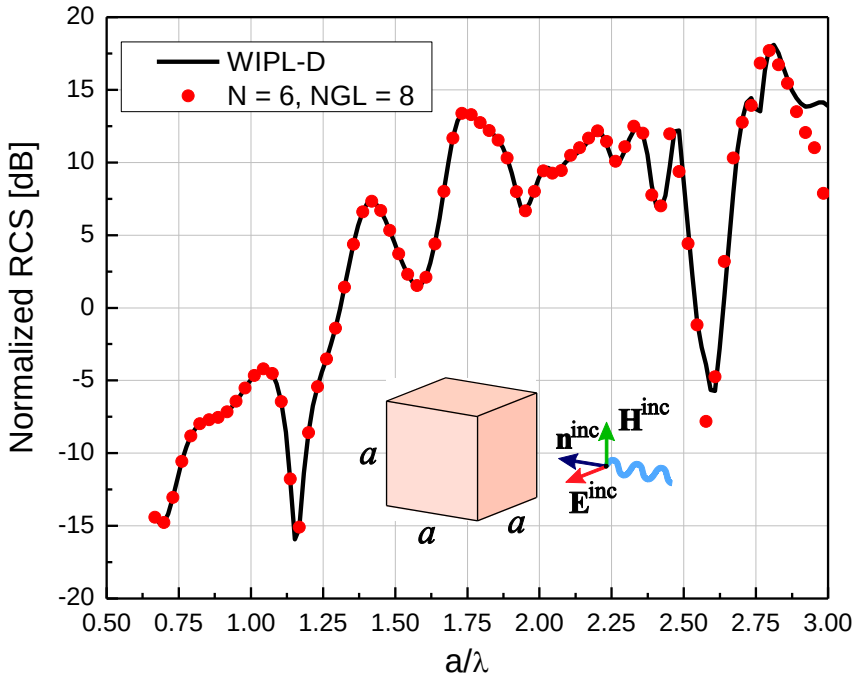

Fig. 4.19. Higher order MoM-SIE computation of a dielectric cube scatterer with $E = 1\times1$: the optimal solution (the results are shown also beyond the reasonable range, i.e., up to $a/\lambda = 3$).

For the mesh with $E = 2\times2$, the results in Fig. 4.21 are accurate up to $a/\lambda = 4$ ($e = 2\lambda$, again) for $N = 6$. Using $N = 7$ increases this range up to $a/\lambda = 4.5$. From Fig. 4.22, we conclude that $NGL = N + 2$ is consistently optimal, as well as that the optimal polynomial order is again $N = 6$, while orders $N = 7$ and higher are not recommended. The optimal solution is presented in Fig. 4.23. We also see, in Fig. 4.21, that $N = 2$ or 3 is optimal for $e \leq 0.5\lambda$ ($a/\lambda \leq 1$), $N = 4$ is the best choice for $0.5\lambda < e \leq \lambda$, and $N = 5$ should be adopted for $\lambda < e \leq 1.5\lambda$.

Results in Figs. 4.25–4.27 for the model of the dielectric cube scatterer with $E = 3\times3$ yield identical conclusions as those in Figs. 4.21–4.23.

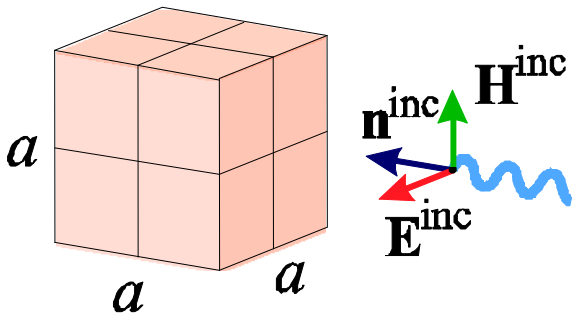

Fig. 4.20. MoM-SIE simulations of a dielectric cube with $E = 2\times2$.

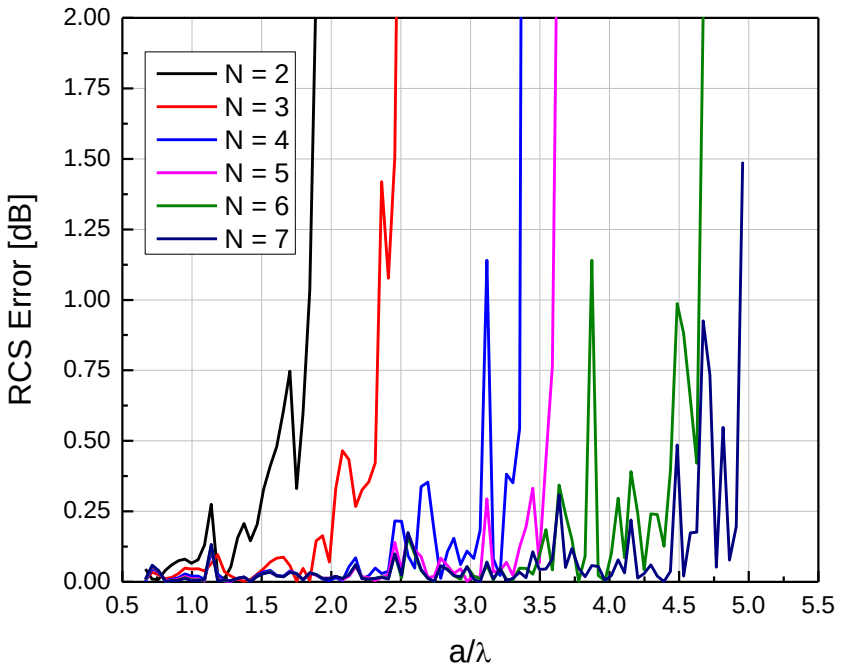

Fig. 4.21. MoM-SIE simulations of a dielectric cube with $E = 2\times2$: RCS error vs. the model electrical size ($NGL = 20$).

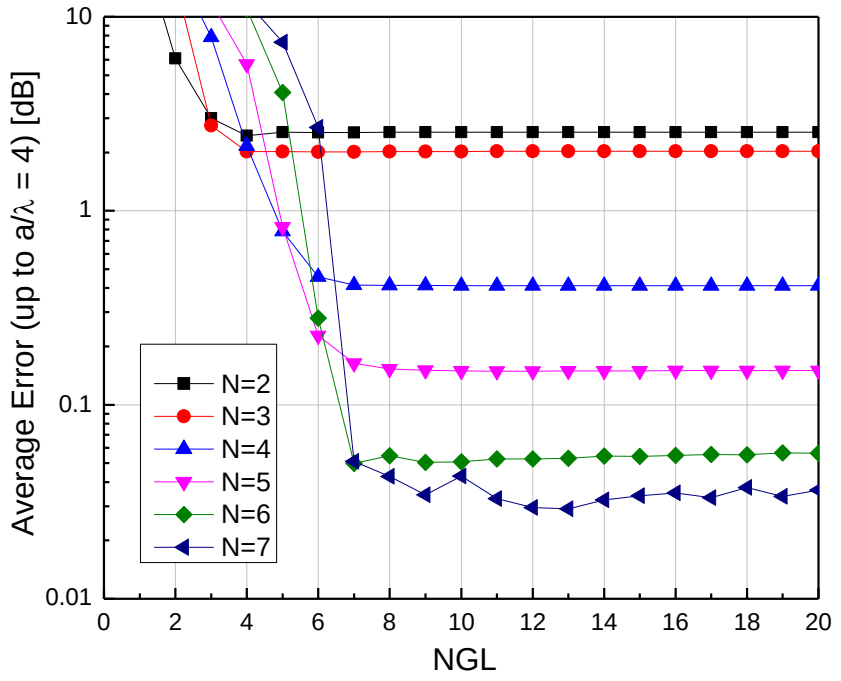

Fig. 4.22. MoM-SIE simulations of a dielectric cube with $E = 2\times2$: average RCS error for reasonable model sizes, $a/\lambda \leq 4$, vs. NGL.

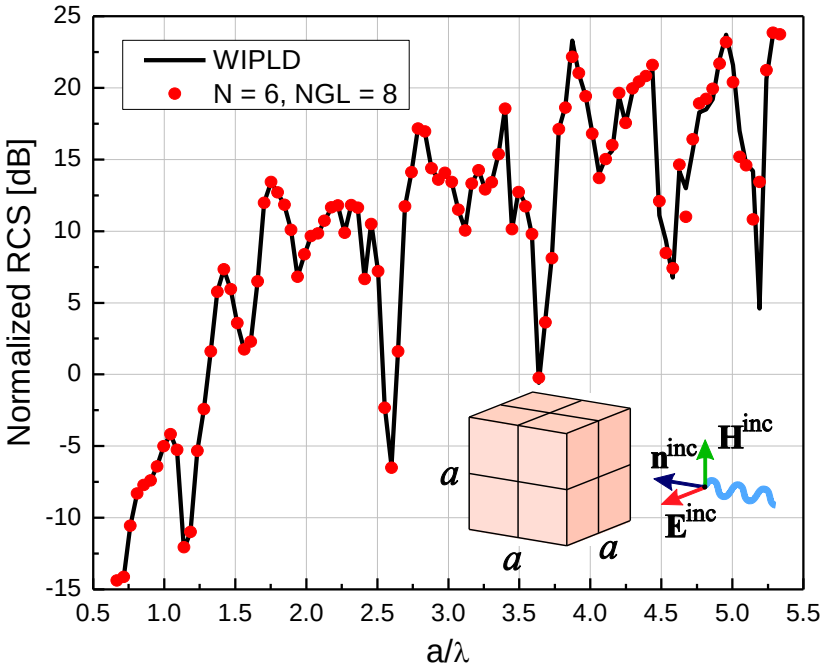

Fig. 4.23. MoM-SIE simulations of a dielectric cube with E = 2×2: the optimal solution (shown within the reasonable range and above it, up to a/λ = 5.5).

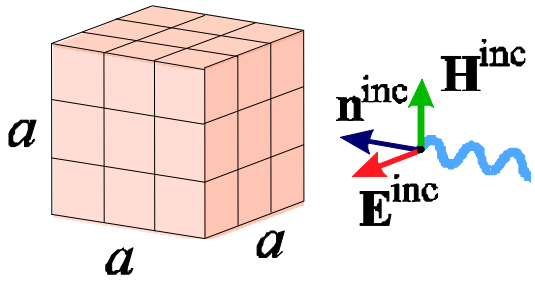

Fig. 4.24. MoM-SIE analysis of a dielectric cube with E = 3×3.

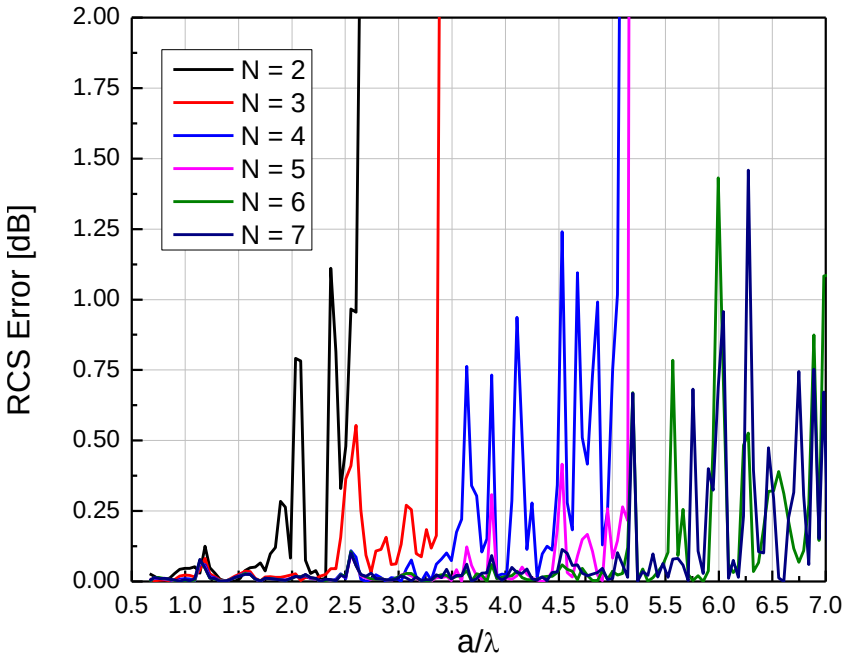

Fig. 4.25. MoM-SIE analysis of a dielectric cube with E = 3×3: RCS error (NGL = 20).

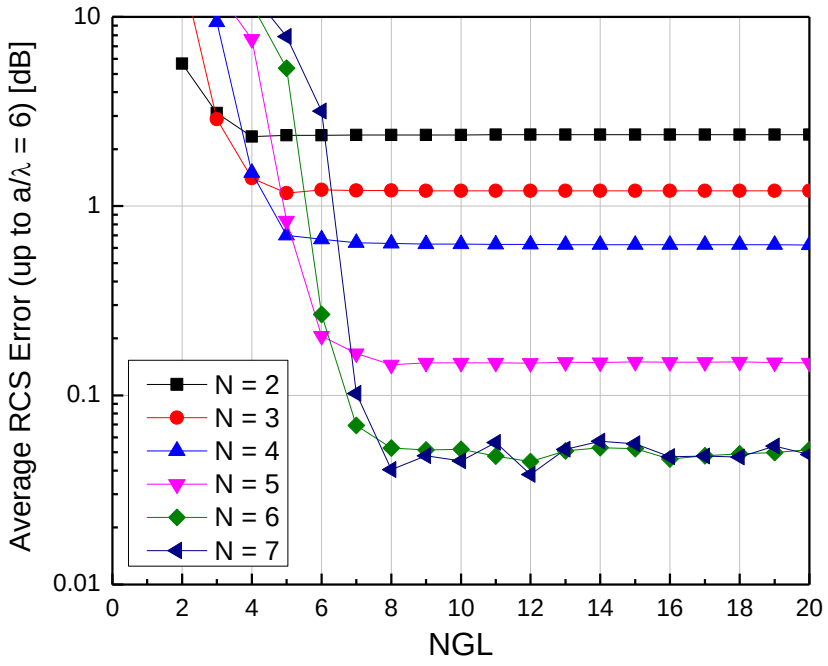

Fig. 4.26. MoM-SIE analysis of a dielectric cube with E = 3×3: average RCS error for reasonable model sizes up to a/λ = 6.

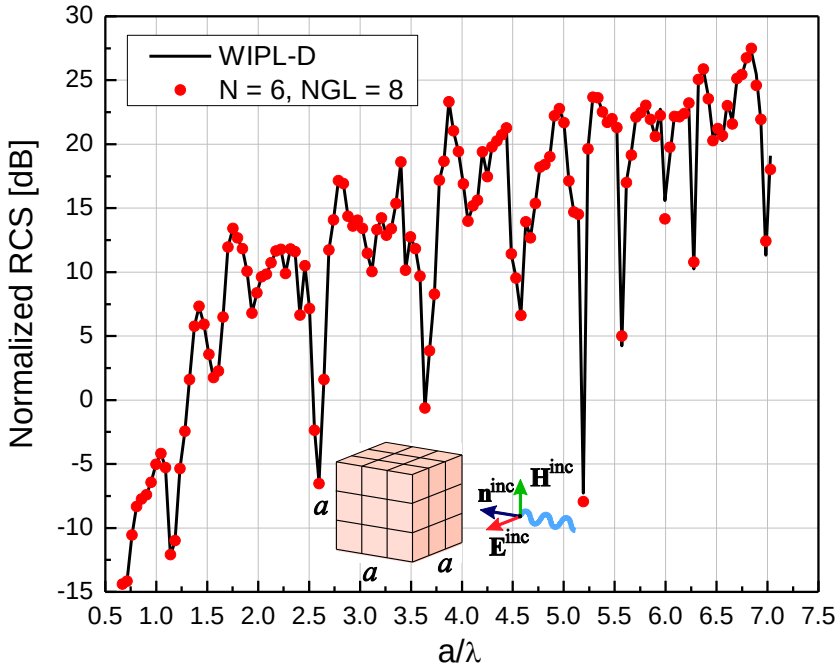

Fig. 4.27. MoM-SIE analysis of a dielectric cube with $E = 3\times3$: the optimal solution (shown across and beyond the reasonable range).

Overall, the conclusions are practically the same as in the analysis of metallic scatterers, that $N = 6$ and $NGL = 8$ constitute the optimal (or very close to optimal) choice for MoM-SIE expansion polynomial orders and numbers of Gauss-Legendre integration points, respectively, that the mesh should be refined for elmements larger than $e = 2\lambda$ in edge length, which corresponds to the conservative maximum element edge length selection for metallic scatterers of $e = 2\lambda_0$, that the optimal orders N are reduced by one for every reduction of the element size by 0.5λ if elements smaller than optimal have to be used, and that setting $NGL = N + 2$ is generally optimal for any N.

4.3. Optimal Higher Order Modeling Parameters for MoM-SIE Scattering Analysis of a Dielectric Sphere

The next example is a dielectric spherical scatterer (with $a = 1$ m and $\varepsilon_r = 4$) analyzed using the higher order MoM-SIE technique, and the first geometrical model is characterized by $E = 1\times1$ and $K = 2$. From the results in Fig. 4.28, we realize that the solution accuracy is limited by the accuracy of the geometrical model, and that it cannot be improved by *p*-refinement. For an *h*-refined model with $E = 2\times2$ and $K = 2$, we observe, in Fig. 4.29, that the model enables accurate simulations up to $a/\lambda = 1$ or $d/\lambda = 2$ (d is the diameter of the sphere), with the elements being about $e = 0.8\lambda$ across, for $N = 2$, and up to $a/\lambda = 1.75$ or $d/\lambda = 3.5$ ($e = 1.4\ \lambda$) for $N = 3$, while, based on Fig. 4.30, $NGL = N + 1$ is an optimal choice. High-order basis functions ($N \geq 4$) cannot be efficiently used due to the geometrical inaccuracy of the model.

We then increase the element geometrical orders in the $E = 1\times1$ model of the sphere to $K = 4$ and repeat the procedure. Results in Fig. 4.32 indicate that the model can now be accurately simulated up to at least $a/\lambda = 1.3$ or $d/\lambda = 2.6$ ($e = 2\lambda$) with $N = 6$. According to Fig. 4.33, the average RCS error is very small (0.068 dB) for $N = 4$ and $NGL = 6$, and does not improve much with further *p*-refinement, due to small geometrical inaccuracy (e.g., setting $N = 6$ and $NGL = 8$ yields a 0.057 dB error), while generally optimal orders of Gauss-Legendre integration formulas are (observing the "knees" of the respective curves) $NGL = N + 2$ (for any N). It turns out that we can now take advantage of high-order basis functions due to significantly higher geometrical accuracy of the model than

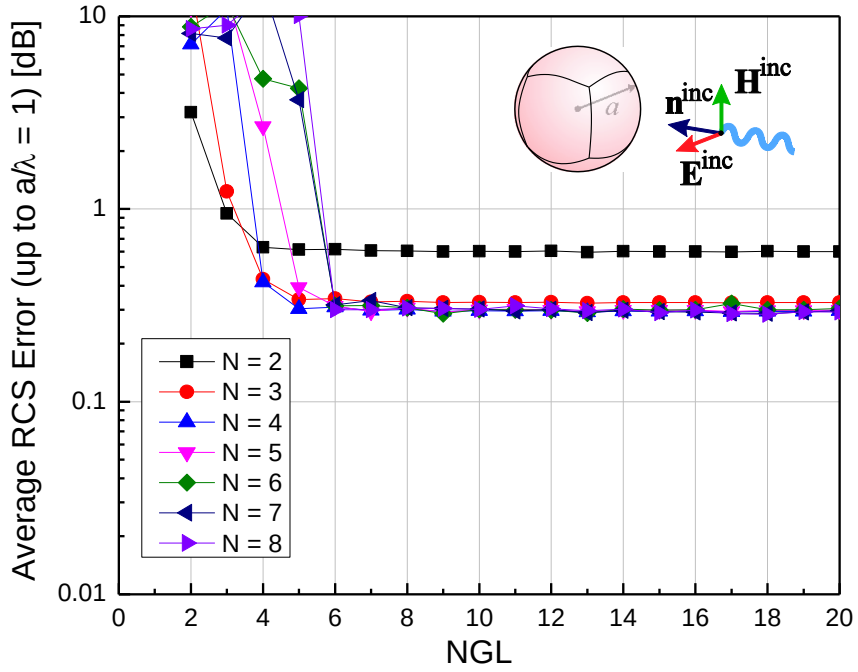

Fig. 4.28. Higher order MoM-SIE analysis of a dielectric spherical scatterer with K = 2: average RCS error for E = 1×1 and p-refinement (unsuccessful) vs. NGL.

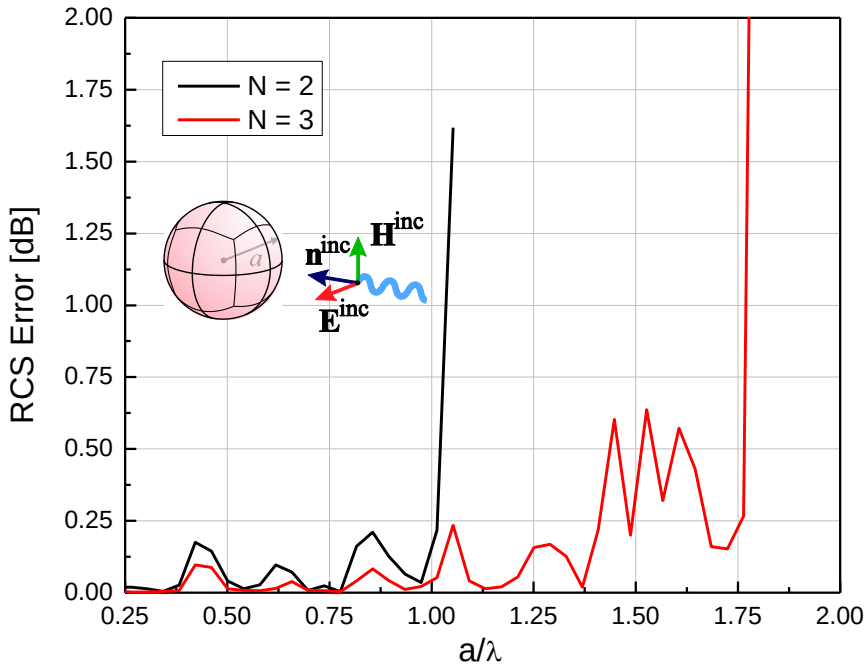

Fig. 4.29. Higher order MoM-SIE analysis of a dielectric spherical scatterer with K = 2: RCS error for E = 2×2, NGL = 20, and two lower values of N vs. the model electrical size.

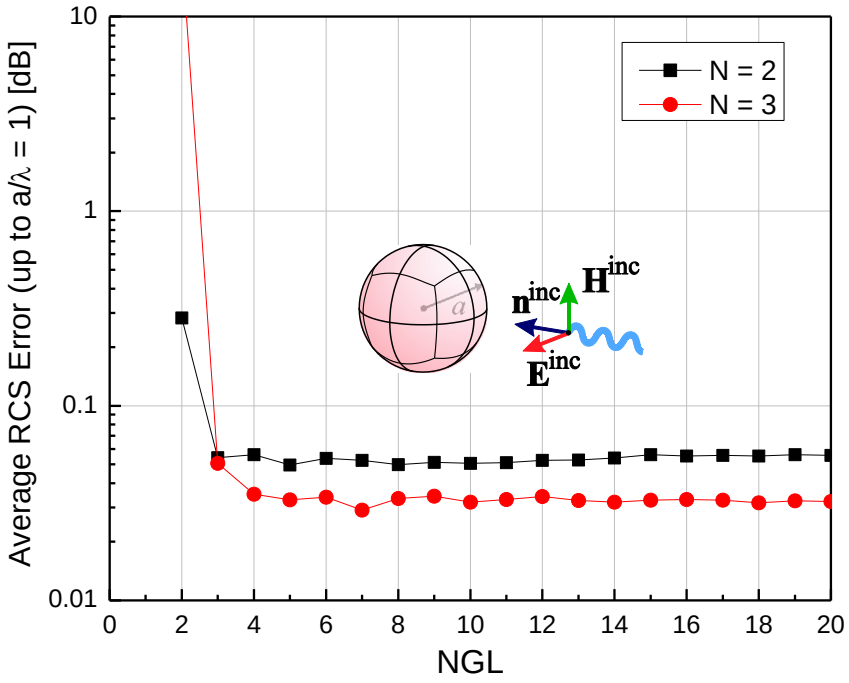

Fig. 4.30. Higher order MoM-SIE analysis of a dielectric spherical scatterer with $K = 2$: RCS error for $E = 2\times2$ averaged for multiple reasonable model sizes, $d/\lambda \leq 2$, vs. *NGL*.

with $K = 2$. However, orders $N \geq 8$ are not recommended, since they do not yield better average errors. The optimal solution, for $N = 6$, is given in Fig. 4.34. Note that all conclusions are essentially the same as for the dielectric cube. Note also that the same conclusions are obtained for a metallic (PEC) spherical scatterer as well.

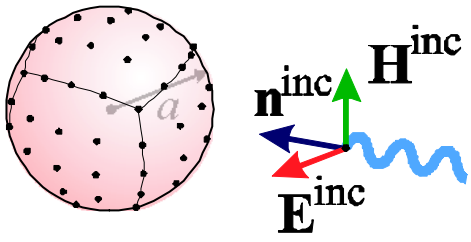

Fig. 4.31. MoM-SIE scattering computation of a dielectric sphere with $E = 1\times1$ and $K = 4$.

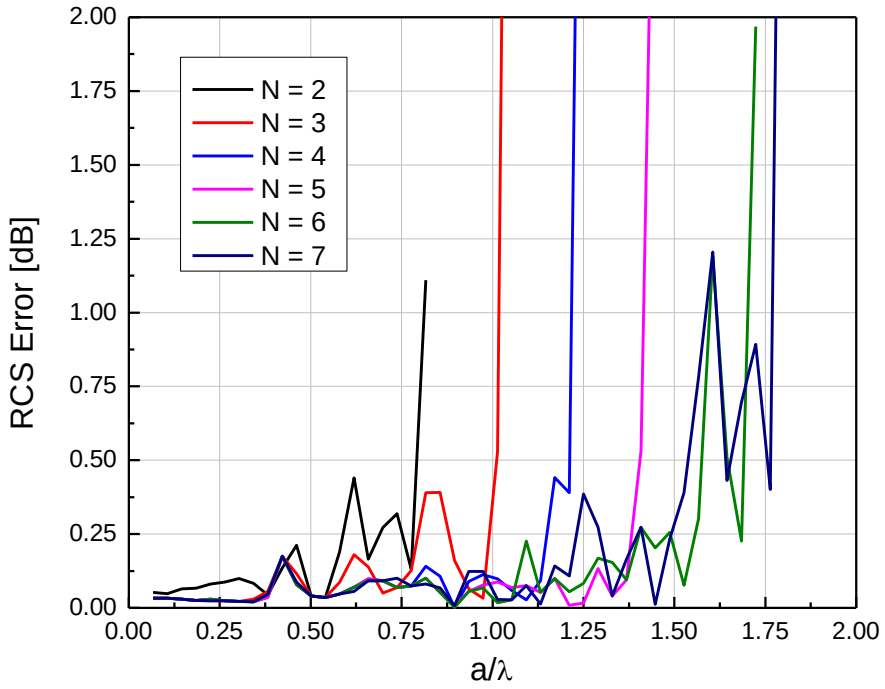

Fig. 4.32. MoM-SIE scattering computation of a dielectric sphere with $E = 1\times1$ and $K = 4$: RCS error vs. the model electrical size ($NGL = 20$).

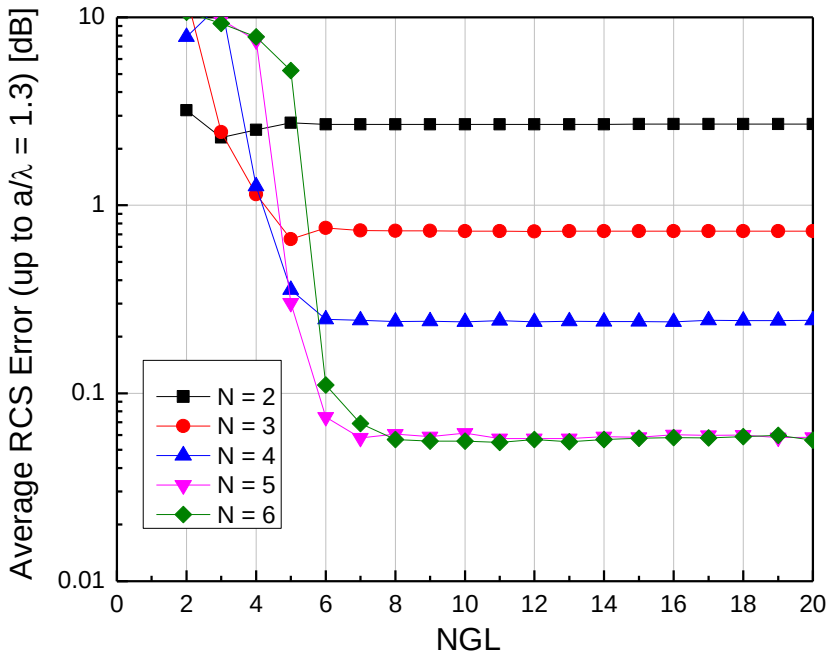

Fig. 4.33. MoM-SIE scattering computation of a dielectric sphere with $E = 1\times1$ and $K = 4$: average RCS error for reasonable model sizes up to $d/\lambda = 2.6$ vs. NGL.

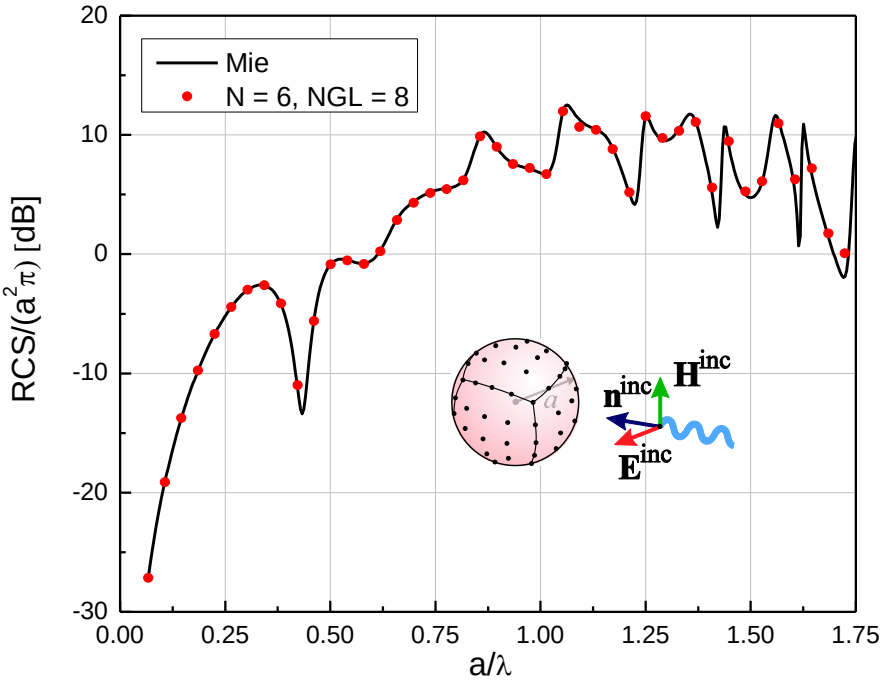

Fig. 4.34. MoM-SIE scattering computation of a dielectric sphere with $E = 1\times1$ and $K = 4$: the optimal solution (shown within and above the reasonable range).

4.4. Optimal Higher Order Modeling Parameters for FEM-MoM Scattering Analysis of a Dielectric Cube

We next conduct a numerical study of higher order modeling parameters in the hybrid FEM-MoM scattering analysis of a dielectric cube ($a = 1$ m and $\varepsilon_r = 4$), adopting the simplest model possible, with $E = 1\times1$ (one FEM and six MoM elements). We sweep polynomial orders for FEM field expansions from $N_{\text{FEM}} = 3$ to 11 and for MoM current expansions from $N_{\text{MoM}} = 2$ to 13, keeping a conservative choice of orders of Gauss-Legendre integration formulas given by $NGL_{\text{MoM}} = N_{\text{MoM}} + 4$ (higher than optimal according to the MoM-SIE studies) and adopting the same choice for the FEM part, $NGL_{\text{FEM}} = N_{\text{FEM}} + 4$. Fig. 4.35 shows that the minimal order sums $N_{\text{FEM}} + N_{\text{MoM}}$ (thick

gray curve) for any given error are achieved when parameter $N_{FEM} - N_{MoM}$ equals 1 or 2. However, we realize that N_{FEM} is the accuracy limiting factor (light yellow areas), and hence the choice that gives the minimal order sum is $N_{FEM} - N_{MoM} = 1$ (green curve). Note that the light yellow ribbons (constant N_{FEM}) are depicted for the first 5 curves only (excluding the blue and magenta curves). These ribbons would be shifted higher (larger error) for the $N_{FEM} - N_{MoM} = +2$ curve and even higher for the $N_{FEM} - N_{MoM} = +3$ curve. So, the conclusion is that the optimal order separation between N_{FEM} and N_{MoM} is unity. This can be attributed to the fact that dominant FEM-MoM inner products are normally those between FEM and MoM basis functions in the same direction, whose maximal orders are offset by one in the mixed-order arrangement for curl-conforming functions in (7) with respect to that for divergence-conforming functions in (3).

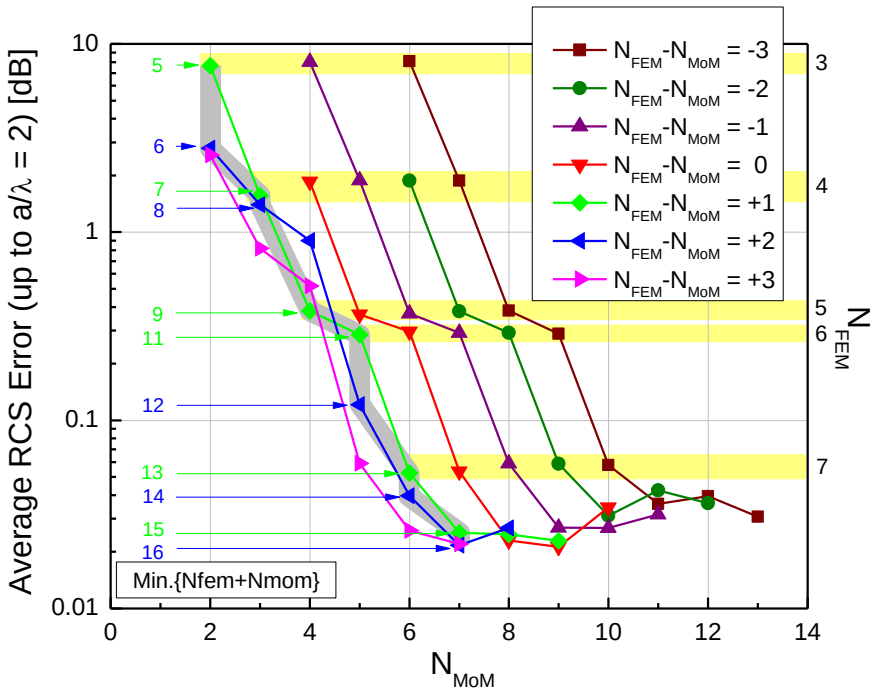

Fig. 4.35. Higher order FEM-MoM scattering analysis of a dielectric cube with $E = 1\times1$: RCS error averaged for multiple reasonable model sizes, up to $a/\lambda = 2$, for different polynomial orders N_{FEM} and N_{MoM}.

Finally, to determine the optimal *NGL* and *N* in the FEM-MoM analysis, we simulate the same dielectric scatterer employing the optimal $N_{FEM} - N_{MoM} = 1$ and systematically varying N_{FEM} from 5 to 10, and plot the graphs in Figs. 4.36 and 4.37. To reduce the number of combinations and computations, we also adopt $NGL_{FEM} - NGL_{MoM} = 1$. Based on Fig. 4.36, we conclude that the cube can be very accurately analyzed up to $a/\lambda = 2$ ($e = 2\lambda$) using $N_{FEM} = 7$ and $N_{MoM} = 6$. From Fig. 4.37, on the other side, we obtain that the generally optimal NGL_{FEM} ("knees" of the curves) is $NGL_{FEM} = N_{FEM} + 1$ for any N_{FEM} (but higher *NGL*s can be used as well), and that the overall optimal orders come out to be $N_{FEM} = 7$, $N_{MoM} = 6$, $NGL_{FEM} = 8$, and $NGL_{MoM} = 7$. This conclusion is consistent with conclusions drawn for the same scatterer analyzed by the MoM-SIE technique, where $N_{MoM\text{-}SIE} = 6$ and $e = 2\lambda$ is the optimal choice as well.

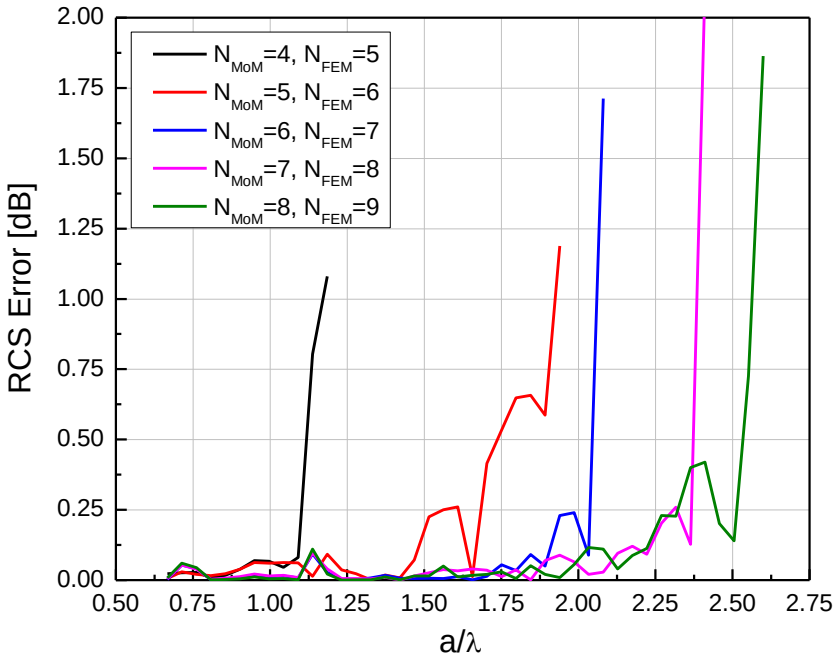

Fig. 4.36. Higher order FEM-MoM scattering analysis of a dielectric cube with $E = 1\times1$: absolute RCS error for a series of values for N_{FEM} ($N_{FEM} - N_{MoM} = 1$) vs. the electrical size of the scatterer ($NGL_{FEM} = 20$ and $NGL_{MoM} = 19$).

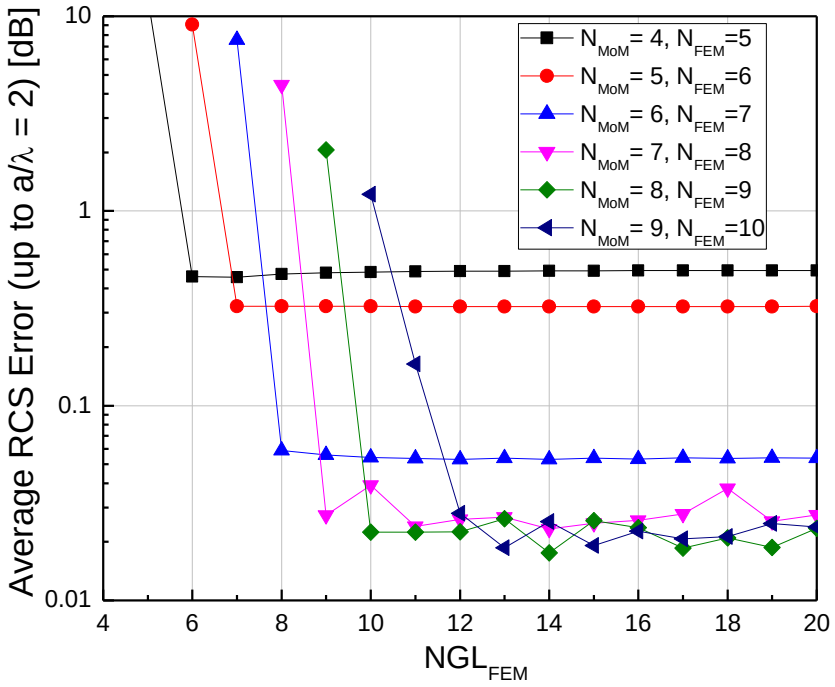

Fig. 4.37. Higher order FEM-MoM scattering analysis of a dielectric cube with $E = 1\times1$: and average RCS error for reasonable model sizes, $a/\lambda \leq 2$, with *p*-refinement vs. *NGL* ($NGL_{\mathrm{FEM}} - NGL_{\mathrm{MoM}} = 1$).

4.5. Computational Time

To further emphasize the importance of knowing and using the optimal (or nearly optimal) *N* and *NGL* in a higher order computational EM model, and thus not adopting their values in an ad hoc manner and higher than reasonable or necessary, Fig. 13 provides the graphs of the computational times for the MoM-SIE simulations of the simplest model of the dielectric cube scatterer. It is apparent from the figure that increasing *N* beyond 6 or 7 and *NGL* beyond 10 can be very costly. We also see that, for the generally optimal choice of $N = 6$, the simulation time is 31% longer if $NGL = N + 4$ is used instead of the generally optimal $NGL = N + 2$. If a "brute-force" adoption of $NGL = 20$ is employed, the simulation time is 742% longer. Hence, optimizing both *N*

and *NGL* is more than worthwhile and justified as far as the computational time is concerned. In addition, using geometrical orders higher than $K = 4$ also results in a large increase of computational time, and is thus not recommended.

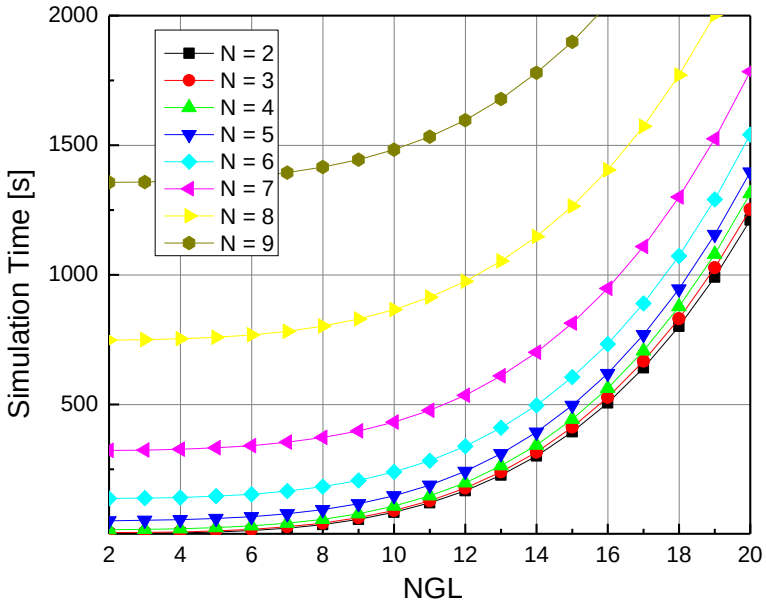

Fig. 13. Computational time for the MoM-SIE scattering analysis of a dielectric cube ($E = 1\times1$) in 100 frequency points as a function of modeling parameters *N* and *NGL*.

4.6. Higher Order MoM-SIE RCS Analysis of the NASA Almond

As the last example, we perform higher order MoM-SIE RCS analysis of the NASA almond, a benchmark target established by the Electromagnetic Code Consortium (EMCC) [71]. The length of the almond is d = 9.936 inches (25.24 cm). Its geometry is defined by the following equations [71] in terms of the Cartesian coordinate system as in Fig. 4.31:

for $-0.41667 < t < 0$ and $-\pi < t < \pi$

$$x = dt \text{ inches} \tag{4.1}$$

$$y = 0.193333d\sqrt{1-\left(\frac{t}{0.416667}\right)^2}\cos\psi \tag{4.2}$$

$$z = 0.064444d\sqrt{1-\left(\frac{t}{0.416667}\right)^2}\sin\psi \tag{4.3}$$

for $0 < t < 0.58333$ and $-\pi < t < \pi$

$$x = dt \text{ inches} \tag{4.4}$$

$$y = 4.83345d\left[\sqrt{1-\left(\frac{t}{2.08335}\right)^2} - 0.96\right]\cos\psi \tag{4.5}$$

$$z = 1.61115d\left[\sqrt{1-\left(\frac{t}{2.08335}\right)^2} - 0.96\right]\sin\psi \tag{4.6}$$

First, we analyze the almond at a frequency of f = 1.19 GHz (λ_0 = 25.21 cm). Fig. 4.31 shows a model of the almond built [based on geometrical equations (4.1)-(4.6)] using M = 56 quadrilateral curved elements with K = 2, N = 2, and NGL = 4 (all elements are in the $e \le 0.25\lambda_0$ range), resulting in a total of only 448 unknowns (with no use of symmetry). The higher order simulation results for the RCS of the almond are compared in Fig. 4.32 with the results obtained by WIPL-D and FEKO [73], respectively, as well as with measurements [71]. We observe an excellent mutual agreement of the three sets of numerical results and their good agreement with the measurements – for the parameters in the higher order model selected exactly according to the established recipes for adoption of higher order modeling parameters for elements smaller than optimal.

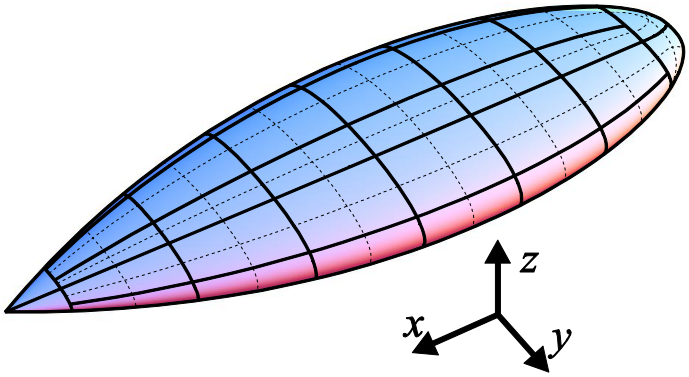

Fig. 4.31. Higher order MoM-SIE scattering analysis of the NASA metallic almond at f = 1.19 GHz [71]: geometrical model with M = 56 curved (K = 2) quadrilateral elements.

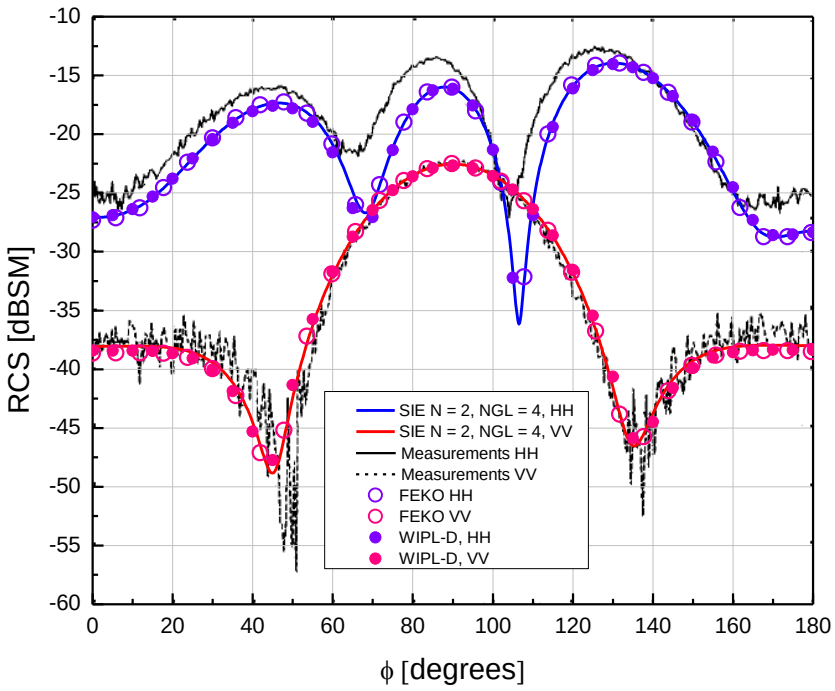

Fig. 4.32. Higher order MoM-SIE scattering analysis of the NASA metallic almond at f = 1.19 GHz: comparison of the simulation results for the RCS of the almond as a function of the azimuthal angle (the elevation angle is zero) for the horizontal (HH) and vertical (VV) polarizations, respectively, with the numerical results obtained by WIPL-D and FEKO [73], as well as with the results of measurements [71].

Next, we analyze the NASA almond at a frequency of f = 7 GHz (λ_0 = 4.29 cm). Here, we use two geometrical models, both with K = 2 and M = 56 (226 interpolation nodes): the first model is the one shown in Fig. 4.31 (all elements are now in the $e \leq 1.5\lambda_0$ range), while the second one ensures a more uniform distribution of interpolation nodes at the expense of having an edge (shared by adjacent patches) along the lateral perimeter of the almond – as depicted in Fig. 4.33. We observe in Figs. 4.34-4.37 an excellent convergence of higher order MoM-SIE results with p-refinement, namely, with increasing N from N = 2 to N = 7 ($NGL = N + 2$ in all cases), as well as an excellent agreement of all results with measurements. However, we also realize that the geometrical model in Fig. 4.33 performs better, when compared to experimental results, than the model in Fig. 4.31 for azimuthal angles from 0 to 20 degrees for the HH polarization and for 80 – 100 degrees for the VV polarization.

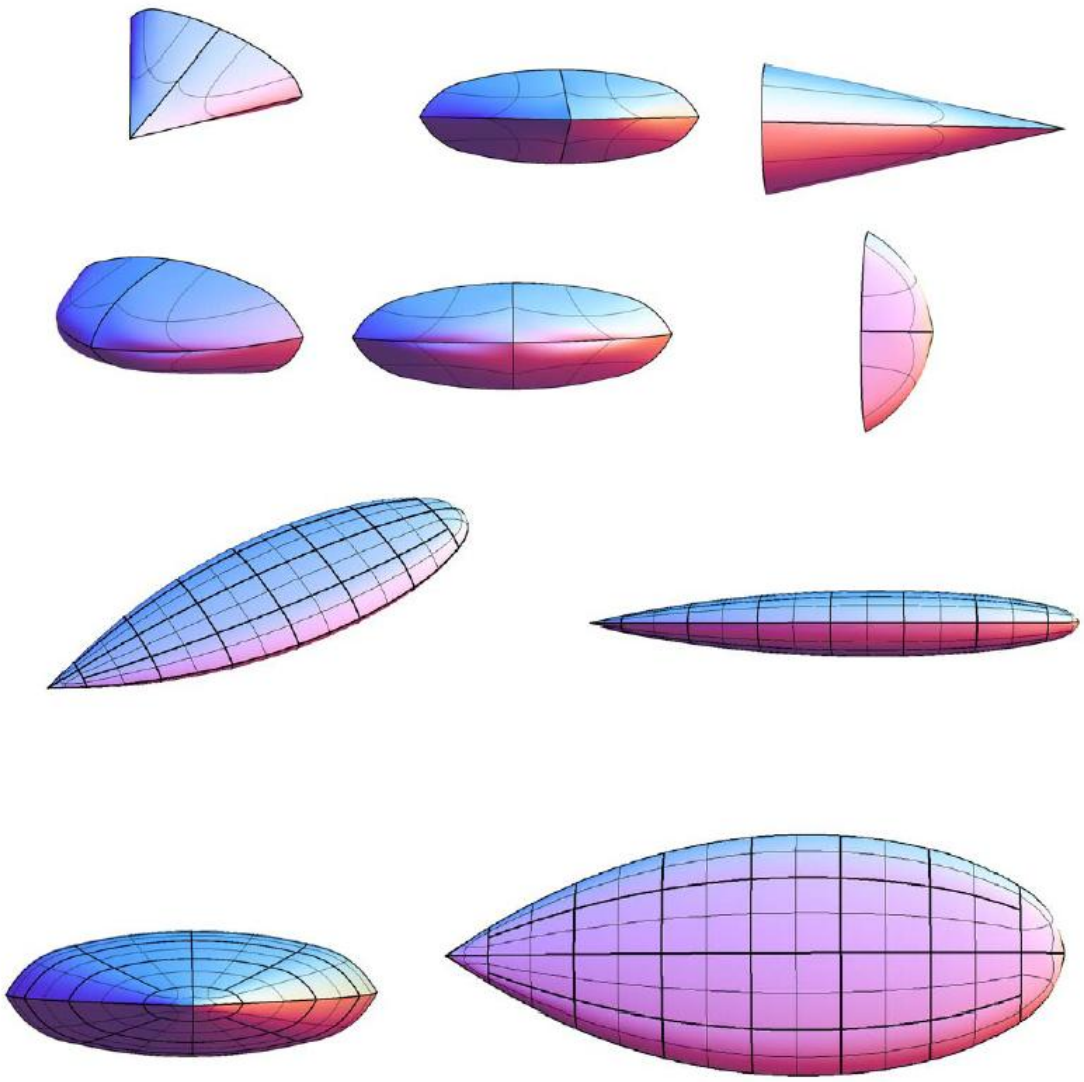

Fig. 4.33. Second geometrical model with M = 56 and K = 2 of the NASA almond, used at f = 7 GHz: the model ensures a more uniform distribution of interpolation nodes, while having an edge (shared by adjacent patches) along the lateral perimeter of the almond.

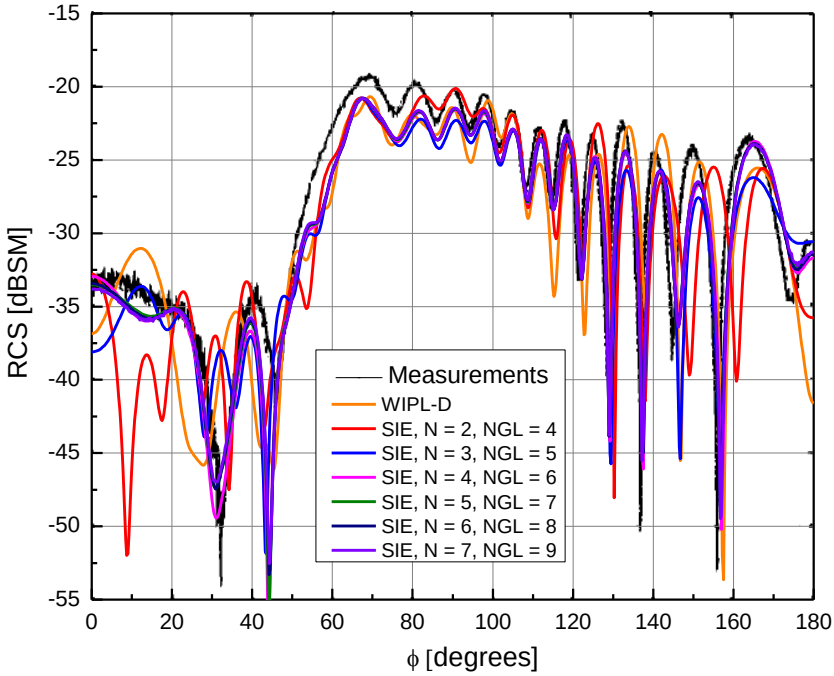

Fig. 4.34. Higher order MoM-SIE scattering analysis of the NASA metallic almond at f = 7 GHz using the geometrical model in Fig. 4.31: comparison of the simulation results for the RCS of the almond for the horizontal (HH) polarization with the numerical results obtained by WIPL-D and with the results of measurements [71].

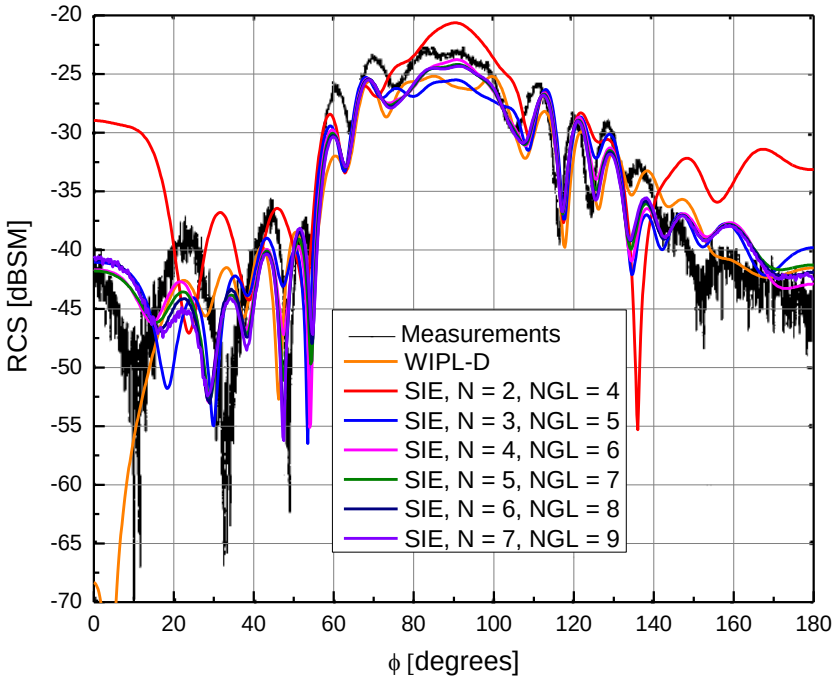

Fig. 4.35. Higher order MoM-SIE scattering analysis of the NASA metallic almond at f = 7 GHz using the geometrical model in Fig. 4.31: comparison of the simulation results for the RCS of the almond for the vertical (VV) polarization with the numerical results obtained by WIPL-D and with the results of measurements [71].

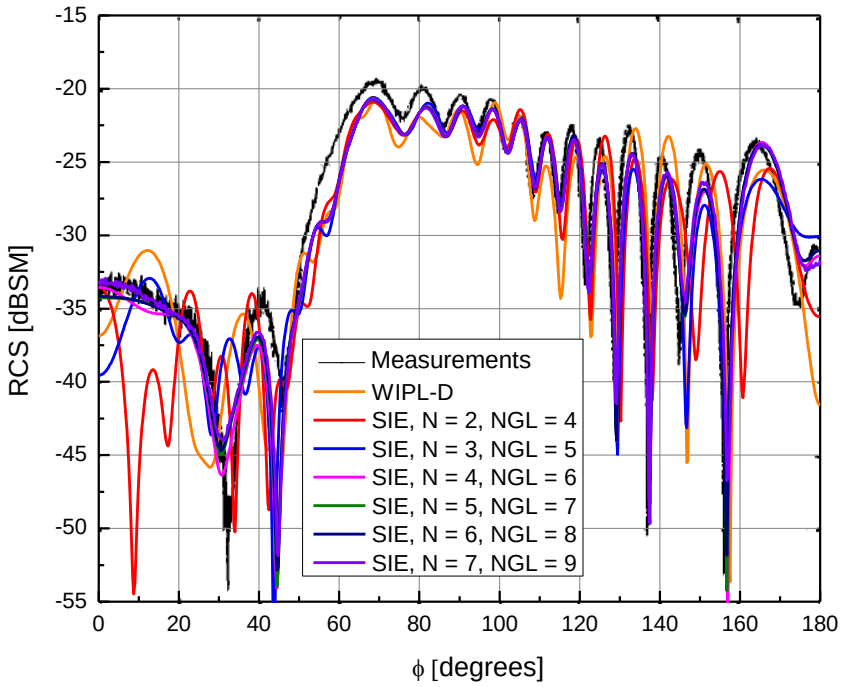

Fig. 4.36. Higher order MoM-SIE RCS analysis of the NASA almond at f = 7 GHz for the HH polarization using the geometrical model in Fig. 4.33: comparison with the numerical results obtained by WIPL-D and with the experimental results [71].

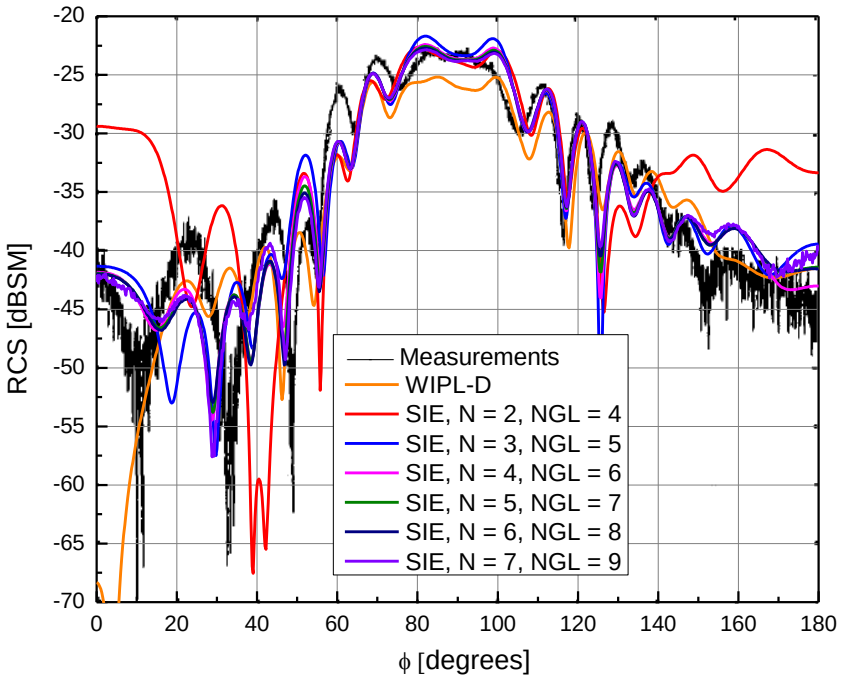

Fig. 4.37. Higher order MoM-SIE RCS analysis of the NASA almond at f = 7 GHz for the VV polarization using the geometrical model in Fig. 4.33: comparison with the numerical results obtained by WIPL-D and with the experimental results [71].

5. CONCLUSIONS: OPTIMAL MODELING PARAMETERS AND PARAMETER LIMITS

The previous two chapters have investigated and evaluated the behavior of higher order hierarchical MoM-SIE and FEM-MoM numerical solutions to electromagnetic scattering problems by running an exhaustive series of simulations and systematically varying and studying the key higher order modeling parameters and their influence on the solutions. Based on numerical experiments and comprehensive case studies on symmetric canonical models that allow using elements with isotropic higher order parameters and uniform meshes (to limit the combinatorial space of the parameters in investigations), this work has established and validated general guidelines and instructions, and as precise as possible quantitative recipes, for adoptions of optimal higher order and large-domain parameters for electromagnetic modeling, within the class of CEM approaches and techniques considered. The modeling parameters considered (note that all these parameters can, theoretically, be arbitrary) are: electrical dimensions of elements (subdivisions) in the model, e/λ (*h*-refinement), polynomial orders of basis and testing functions (*p*-refinement), *N*, orders of Gauss-Legendre integration formulas (numbers of integration points – integration accuracy), *NGL*, and geometrical orders of elements (orders of Lagrange-type curvature) in the model, *K*. In addition, higher order MoM-SIE RCS analysis of an EMCC benchmark target (NASA almond) has been performed.

Overall, the main conclusions of the study, which is the first such study of higher order parameters in CEM, can be summarized as follows. The MoM-SIE or FEM-MoM model should be *h*-refined if the dimensions of (flat or curved) elements become greater than $e = 2\lambda$, with λ standing for the wavelength in free space (λ_0) in the case of metallic structures and for the wavelength in the dielectric for dielectric ones. The optimal (or nearly optimal) choice of orders N and NGL is given by $N = 6$ and $NGL = 8$, respectively, for both metallic and dielectric structures, with or without pronounced curvature. If elements smaller than optimal have to be used, due to the geometrical or material complexity of the structure, the optimal polynomial orders should be adopted as follows: $N = 1$ for element sizes $e \leq 0.1\lambda$, $N = 2$ for $0.1\lambda < e \leq 0.25\lambda$, $N = 3$ for $0.25\lambda < e \leq 0.5\lambda$, $N = 4$ for $0.5\lambda < e \leq \lambda$, $N = 5$ for $\lambda < e \leq 1.5\lambda$, and $N = 6$ for $1.5\lambda < e \leq 2\lambda$. The minimum average total number of unknowns per wavelength for accurate RCS analysis amounts to about 14.1, 11.3, 8.5, 5.7, 4.7, and 4.2 if $N = 1$, 2, 3, 4, 5, and 6, respectively, is used in a higher order model of a PEC structure, while these numbers are doubled for dielectric scatterers. In hybrid FEM-MoM models, $N_{\text{FEM}} - N_{\text{MoM}} = 1$ is optimal. Polynomial orders higher than $N = 8$ are not recommended to be used. It is generally optimal to use $NGL = N + 2$ for any N. It is generally not recommended to increase NGL any further. For curved structures, $K = 2$-4 is always a better choice than $K = 1$; for surfaces with pronounced curvature, $K = 4$ should be adopted in order to enable efficient use of high orders N on electrically large elements, while geometrical orders higher than that are not recommended. All conclusions are for computations in single precision.

The developed set of rules (recipes) for adopting the optimal simulation parameters in a typical higher order EM simulation and identified limits (perimeters) of the parameters for which valid and reasonable solutions of the EM problems can be obtained are meant to be built into a comprehensive knowledge base that should be of significant interest and value for MoM and FEM practitioners and application engineers using similar (or even not so similar) CEM software, and may result in considerable reductions of the overall simulation (modeling plus computation) time. For instance, computations involving unreasonably high or low polynomial orders of basis and testing functions and/or orders of Gauss-Legendre integration formulas, and unreasonable, too large or too small, electrical dimensions of elements in the model, as well as various unreasonable combinations of different choices, could result in meaningless models and simulations (that often cannot be refined) and/or in an unnecessarily extensive utilization of computational resources (e.g., orders of magnitude longer computational times). It should also be valuable to CEM research community in developing new higher order MoM and FEM computational methods and techniques, and to CEM software designers (e.g., in designing and building automatic or semi-automatic higher order meshes and models with optimally preset parameters).

The ultimate goal of this present work and the continued future work in this area is to reduce the dilemmas and uncertainties associated with the great modeling flexibility in higher order CEM techniques in terms of the size and shape of elements and spans of approximation and testing functions, and to ease and facilitate the decisions to be made on how to actually use them, by both CEM developers and practitioners. The goal is for the class of approaches and techniques considered here and for the higher order CEM

modeling methodology in general to be an easily and confidently used analysis and design tool, with a minimum of expert interaction required to produce valuable results in practical applications. It is expected that other researchers will conduct similar studies with their methods and codes – to build this knowledge base further, although a significant overlap with the presented conclusions is expected, in both qualitative modeling concepts and guidelines and quantitative recipes for optimal parameters. This is especially important given that practically all future CEM techniques and codes will likely have some higher order properties, because such elements and bases exhibit excellent convergence, flexibility, and suitability for refinements and adaptive simulations.

6. TRANSIENT RESPONSE OF ELECTROMAGNETIC STRUCTURES BASED ON HIGHER ORDER ANALYSIS IN FREQUENCY DOMAIN

6.1. Introduction: Time-from-Frequency-Domain FEM Solver

The previous chapters dealt exclusively with MoM and FEM computations in the frequency domain, which is a much more explored and established area of CEM. However, time-domain analysis and characterization of electromagnetic structures and systems and evaluation of associated transient field and wave phenomena are also of great practical importance for a number of areas of applied electromagnetics, including wideband communication, electromagnetic compatibility, electromagnetic interference, packaging, high-speed microwave electronics, signal integrity, material characterization, and other applications. For this purpose, time-domain MoM and FEM techniques have recently been developed [74], allowing electromagnetic phenomena to be modeled directly in the time domain. In [75], for instance, the spatially and temporally varying electric field is approximated using interpolatory spatial vector basis functions defined on tetrahedral elements, with time-dependent field-distribution coefficients, which are determined solving the corresponding second-order ordinary differential equation in time by a time-marching procedure. When compared to frequency-domain solutions, time-

domain MoM and FEM formulations enable effective modeling of time-varying and nonlinear problems and fast broadband simulations (provide broadband information in a single run), at the expense of the additional discretization – in time domain, and the associated numerical complexities, programming and implementation difficulties, and stability and other problems inherent for time-domain computational electromagnetic approaches.

Here, in the realm of FEM computations, we present an alternative approach, an indirect time-domain analysis – namely, finding the time-domain response of a microwave passive structure based on the frequency-domain FEM analysis in conjunction with the discrete Fourier transform (DFT) and its inverse (IDFT). This approach seems to have not been exploited, primarily because it requires FEM solutions with many unknowns (unknown field-distribution coefficients to be determined) at many discrete frequency points, which may be very time consuming and computationally prohibitively costly. This chapter demonstrates exactly opposite – that with a highly efficient and appropriately designed frequency-domain FEM technique it is possible to obtain extremely fast and accurate time-domain solutions of microwave passive structures performing computations in the frequency domain along with the DFT/IDFT. The technique is a higher order large-domain Galerkin-type FEM for 3-D analysis of *N*-port waveguide structures with arbitrary metallic and dielectric discontinuities implementing curl-conforming hierarchical polynomial vector basis functions of arbitrarily high field-approximation orders in conjunction with Lagrange-type curved hexahedral finite elements of arbitrary geometrical orders [26], coupled with standard DFT and IDFT algorithms. The technique appears to be the first time-from-frequency-domain FEM

solver. Note that a similar approach in the method of moments (MoM) framework (using WIPL-D code) is presented in [76].

6.2. Frequency-Domain FEM Analysis of 3-D Multiport Waveguide Structure with Arbitrary Discontinuities

Consider a 3-D *N*-port waveguide structure with an arbitrary metallic and/or dielectric discontinuity shown in Fig. 6.1. In our analysis method [26], the computational domain is first truncated by introducing fictitious planar surfaces at each of the ports, and thus obtained closed structure is then tessellated using curvilinear geometrical elements in the form of Lagrange-type generalized parametric hexahedra of arbitrary geometrical orders, shown in Fig. 6.1 and analytically described by (2.44). The electric fields inside the hexahedra are approximated by means of curl-conforming hierarchical-type vector basis functions in (2.47).

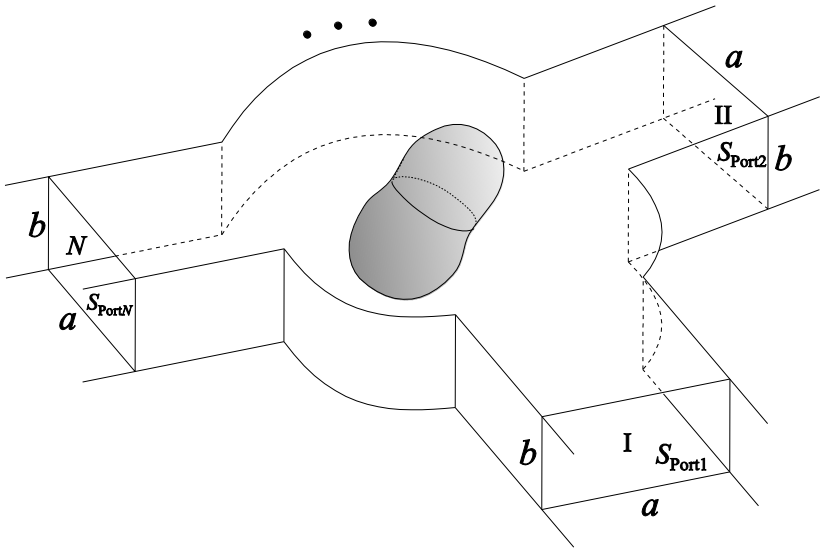

Fig. 6.1. 3-D multiport waveguide structure with an arbitrary discontinuity [26].

In a solution procedure, we invoke the curl-curl electric-field vector wave equation (2.43), a standard Galerkin-type weak form discretization of which is that in (2.49), where the right-hand side term contains the surface integral only across the artificially introduced planar surfaces (waveguide ports). If the waveguide operates in the single-mode regime (which is a standard assumption for practical microwave applications) and the ports are placed far enough from all discontinuities, it can be shown [27] that the boundary condition at the ports can be expressed as

$$\mathbf{n}\times(\nabla\times\mathbf{E})+\mathrm{j}k_{z10}\mathbf{n}\times(\mathbf{n}\times\mathbf{E})=\begin{cases}-2\mathrm{j}k_{z10}\mathbf{E}^{\mathrm{inc}},\ \mathbf{E}^{\mathrm{inc}}=E_0\mathbf{e}_{10}\exp(-\mathrm{j}k_{z10}z) & (\text{excitation port})\\ 0 & (\text{receiving ports})\end{cases},\tag{6.1}$$

where, for a rectangular waveguide, $k_{z10}=\sqrt{k_0^2-(\pi/a)^2}$ is the wave number of the dominant mode (a is the larger dimension of the waveguide cross section), and $\boldsymbol{E}^{\mathrm{inc}}$ is the electric field of the TE_{10} wave, incident on the excitation port. This condition is much easier to implement and faster to compute than alternative multi-mode conditions. However, it has frequently been found to be impractical and computationally costly in traditional small-domain FEM models, due to the fact that placing the ports far from discontinuities (needed to ensure a single-mode simulation) requires a considerable number of additional elements to be employed, which significantly enlarges the computational domain and introduces a large number of new unknowns to be determined. On the other side, this major drawback can be very effectively overcome in the higher order large-domain waveguide modeling, by placing a single large element with a high field-approximation order in the longitudinal direction as a buffer zone between each port and the domain with discontinuities. The sufficient length of the buffer-element allows

for the higher modes excited at the discontinuity to relax before they reach the port, while the high-order field expansion in the longitudinal direction ensures the accurate approximation of the fields throughout the element, without introducing an unnecessarily large number of new unknowns.

Substituting the field expansion (2.47) and the boundary condition (6.1) into (2.49) yields the following FEM matrix equation:

$$([A]-k_0^2[B]+\mathrm{j}k_{z10}[C])\cdot\{\alpha\}=2\mathrm{j}k_{z10}\{G\}. \tag{6.2}$$

Matrix [A] is given by

$$[A]=\begin{bmatrix}[UUA] & [UVA] & [UWA]\\ [VUA] & [VVA] & [VWA]\\ [WUA] & [WVA] & [WWA]\end{bmatrix}, \tag{6.3}$$

and similarly for matrices [B], [C], and [G], where the elements of the respective submatrices have the form

$$UUA_{\hat{i}\hat{j}\hat{k}ijk}=\int_V \mu_{\mathrm{r}}^{-1}(\nabla\times\mathbf{f}_{ui\hat{j}\hat{k}})\cdot(\nabla\times\mathbf{f}_{uijk})\,\mathrm{d}V, \tag{6.4}$$

$$UUB_{\hat{i}\hat{j}\hat{k}ijk}=\int_V \varepsilon_{\mathrm{r}}\mathbf{f}_{ui\hat{j}\hat{k}}\cdot\mathbf{f}_{uijk}\,\mathrm{d}V, \tag{6.5}$$

$$UUC_{\hat{i}\hat{j}\hat{k}ijk}=\int_{S_{\mathrm{allports}}} \mu_{\mathrm{r}}^{-1}(\mathbf{n}\times\mathbf{f}_{ui\hat{j}\hat{k}})\cdot(\mathbf{n}\times\mathbf{f}_{uijk})\,\mathrm{d}S, \tag{6.6}$$

$$UUG_{\hat{i}\hat{j}\hat{k}ijk}=\int_{S_{\mathrm{excitation\,port}}} \mu_{\mathrm{r}}^{-1}(\mathbf{n}\times\mathbf{f}_{ui\hat{j}\hat{k}})\cdot(\mathbf{n}\times\mathbf{E}^{\mathrm{inc}})\,\mathrm{d}S, \tag{6.7}$$

with analogous expressions for the elements corresponding to other combinations of field components. The assembly of a local system of linear equations of the form given by

(6.2) is repeated for each of the elements comprising the mesh, and the global connected system, again of the same form, solved for the unknown coefficients $\{\alpha\}$. Once they are known, the electric field $\boldsymbol{E}$ inside the structure in Fig. 6.1 is computed from (2.47), and the *S*-parameters of the structure are obtained as

$$S_{11} = \frac{\int_{S_{\text{Port1}}} \mathbf{E} \cdot \mathbf{e}_{10} \, \mathrm{d}S}{E_0 \int_{S_{\text{Port1}}} \mathbf{e}_{10} \cdot \mathbf{e}_{10} \, \mathrm{d}S} - 1, \qquad S_{21} = \frac{1}{E_0} \int_{S_{\text{Port2}}} \mathbf{E} \cdot \mathbf{e}_{10} \, \mathrm{d}S \,, \tag{6.8}$$

and so on.

What is very important for finding the time-domain response of multiport waveguide structures based on the frequency-domain analysis, if the materials contained in the structure are dispersionless, integrals appearing in (6.4)-(6.7) are frequency independent. Therefore, for a multifrequency analysis of the same structure, which exactly is our case – where we need a large number of frequency samples of the resulting quantities (e.g., *S*-parameters of the structure), these integrals can be calculated only once, conveniently stored, and then recalled during the problem solution for different excitation frequencies, since the only change in the global system is that of the wave number. This procedure significantly reduces the overall computational time for the time response calculation by allowing the global FEM matrix to be filled only once, at the expense of a considerably larger storage space that needs to be allocated, since matrices [*A*], [*B*], and [*C*] have to be stored separately. However, higher order large-domain FEM models of frequently encountered waveguide discontinuity structures require very small numbers of unknowns for high levels of accuracy, which makes them perfect for implementing the described

multifrequency solution acceleration procedure within the time-from-frequency-domain FEM solver.

6.3. Time Response of a Multiport Waveguide Structure Based on Discrete Fourier Transform

To obtain the transient response of the structure in Fig. 6.1, we excite one of its ports by a causal real signal $E_0(t)$ that is band-limited in the frequency domain. The signal is sampled at N uniformly spaced points over the total time period T, the time step thus amounting to $\Delta t = T/N$, where Δt must satisfy the Nyquist sampling criterion, $\Delta t \le 1/(2f_{\max})$, i.e., the sampling rate, $f_s = 1/\Delta t$, must be at least twice the highest frequency in the spectrum of the signal, $f_{\max}$ [76]. We then compute the frequency-domain response to this excitation, in its discrete (sampled) form, $E_0(t_n)$, as $R(f_k) = S(f_k)E_0(f_k)$, where $E_0(f_k)$ is the discrete Fourier transform (DFT) of $E_0(t_n)$, given by

$$E_0(f_k) = E_0(k) = \sum_{n=0}^{N-1} E_0(t_n) \exp\left(-\mathrm{j}\frac{2\pi}{N}nk\right), \quad f_k = k\frac{f_s}{N}, \quad k = 0, 1, \ldots, N-1, \qquad (6.9)$$

and $S(f_k)$ is the port-to-port frequency-domain transfer function (namely, an S-parameter) of the structure, which can be defined for two different ports (e.g., S_{12}) or for a single port (e.g., S_{11}), and is obtained by the frequency-domain FEM based on (6.1)-(6.8), (2.43), (2.44), (2.47) and (2.49), at frequencies f_k ($k = 0, 1, \ldots, N-1$). In fact, since $S(-f) = S^*(f)$, that is, $S(N-k) = S^*(k)$, only $N/2$ frequency points, for $f > 0$,

suffice in the FEM analysis. Moreover, as the waveguides in Fig. 6.1 are assumed to operate in the single-mode (dominant-mode) regime, with buffer elements at the ports included in the FEM region ensuring the relaxation of the higher order modes, we implement a brick-wall band-pass filter to practically use only frequency samples within the dominant frequency range of the waveguide, between the cutoff frequency of the dominant mode and that of the next propagating mode in the structure. Finally, the transient response $R(t_n)$ is evaluated as the inverse discrete Fourier transform (IDFT) of $R(f_k)$, as follows:

$$R(t_n) = R(n) = \frac{1}{N}\sum_{k=0}^{N-1} R(f_k)\exp\left(\mathrm{j}\frac{2\pi}{N}nk\right),\ t_n = n\Delta t\ ,\ n = 0, 1, \ldots, N-1\ . \tag{6.10}$$

6.4. Numerical Results by the Higher Order FEM-DFT/IDFT Technique and Discussion

As the first numerical example, consider a homogeneous lossless dielectric post in a WR-90 rectangular waveguide [77], as shown in Fig. 6.3(a). The post is illuminated by an incident TE_{10} wave, and we calculate the modal *S*-parameters using the higher order large-domain FEM. In the analysis, we allow a certain distance between the waveguide ports, at which the *S*-parameters are calculated, and the discontinuity, as depicted in Fig. 6.3(b), where the large-domain FEM model (mesh) is also shown. Note that only seven trilinear ($K_u = K_v = K_w = 1$) hexahedral elements are sufficient to model the structure in this example. The polynomial field-expansion orders (N_u, N_v, and N_w) in the FEM simulation range from 4 to 7 in different elements and different directions.

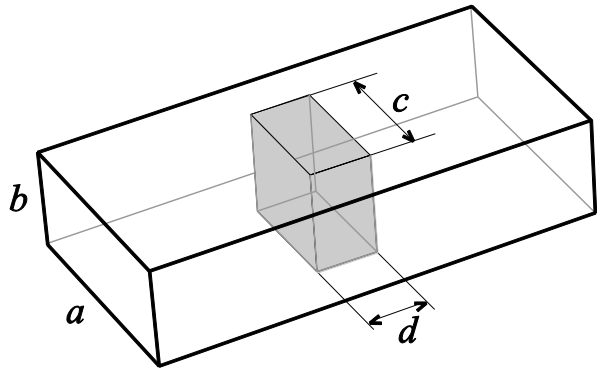

(a)

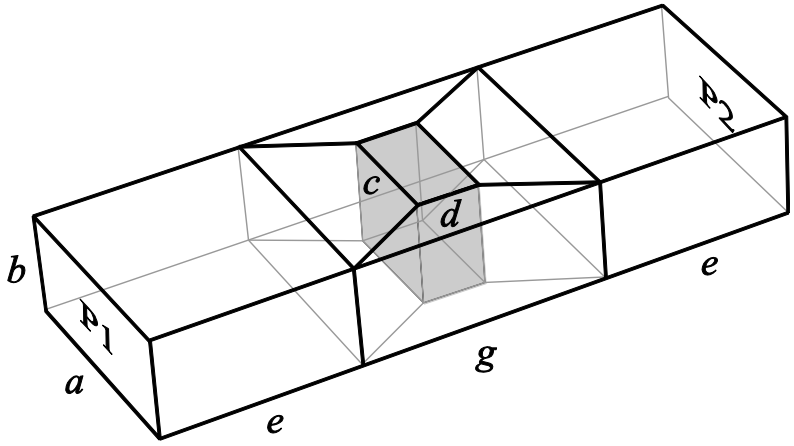

(b)

Fig. 6.3. Dielectric ($\varepsilon_r = 8.2$) post discontinuity in a WR-90 waveguide: (a) definition of the structure geometry ($a = 22.86\,\text{mm}$, $b = 10.16\,\text{mm}$, $c = 12\,\text{mm}$, and $d = 6\,\text{mm}$) [77] and (b) higher order large-domain FEM model (mesh) of the structure using generalized hexahedra in Fig. 6.2 ($e = 45.72\,\text{mm}$ and $g = 24\,\text{mm}$).

For the purpose of verification of the numerical results by an alternative computational technique, which is adopted in the form of a higher order method of moments (MoM) within the surface integral equation (SIE) approach [7], a special model is constructed, as shown in Fig. 6.4, where we first calculate the *S*-parameters between the two wire probes

with point-generators (ports 1' and 2'), and then de-embed the modal *S*-parameters for the two-port section between ports 1 and 2 [78].

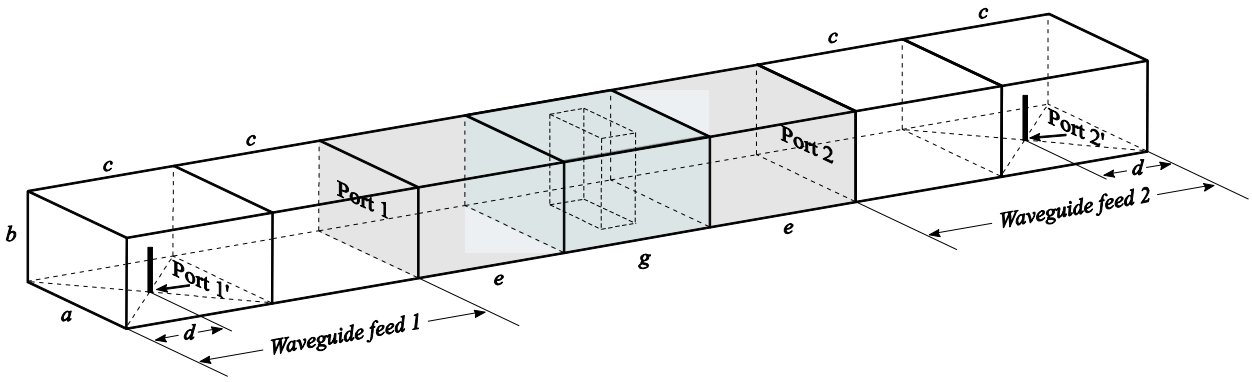

Fig. 6.4. MoM-SIE model of the waveguide structure in Fig. 6.3: the model includes two waveguide feed sections required for the de-embedding of *S*-parameters.

The magnitudes of the computed *S*-parameters of the dielectrically loaded waveguide structure in Fig. 6.1 are plotted in Fig. 6.5. The results obtained by the higher order FEM are compared to the envelope-finite element (EVFE) results from [77] and to the results obtained by the MoM-SIE technique [7], and a very good agreement between the three sets of results is observed. Note that the results obtained by the FEM and MoM (both directly in the frequency domain) are practically identical in the lower half of the considered frequency range, while the EVFE results (extracted from a time-domain solution) are slightly different. The computational time required for the FEM simulation on a very modest laptop computer (IBM ThinkPad T60p with Intel® T7200 CPU at 2.0 GHz) is 64 seconds for matrix filling (only once) and only 0.2 seconds for the solution for *S*-parameters per every frequency point. We consider this simulation to be extremely fast and suitable for large frequency sweeps necessary for the generation of transient responses.

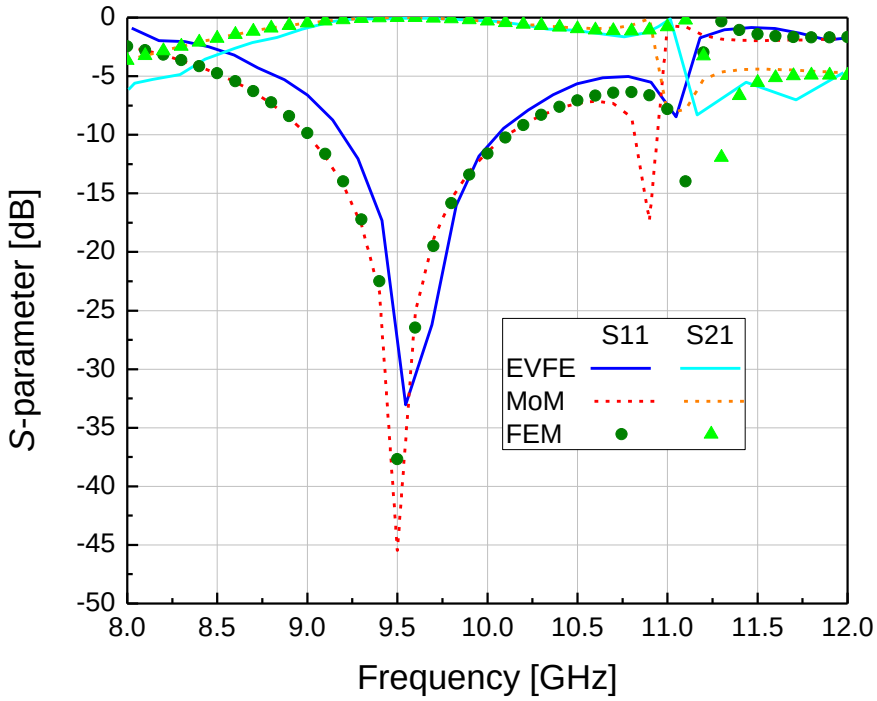

Fig. 6.5. Frequency-domain results for *S*-parameters of the dielectrically loaded waveguide in Fig. 6.3.

We next calculate the transient response of the waveguide structure in Fig. 6.3 exciting it by a modulated Gaussian pulse expressed as [77]

$$E_0(t) = \exp\left[-4\left(\frac{t-t_0}{T}\right)^2\right]\sin\left[2\pi f_c(t-t_0)\right]\text{V/m}\,, \tag{6.11}$$

where the carrier frequency is $f_c = 10\,\text{GHz}$, half bandwidth is $\Delta f = 2.5\,\text{GHz}$, $T = 4/(\pi\Delta f)$, and $t_0 = 1.4\,\text{T}$. The parameters of DFT/IDFT calculations are as follows: the sampling frequency is $f_s = 200\,\text{GHz}$ (time step is $\Delta t = 1/f_s = 5\,\text{ps}$) and the number of samples is $N = 2048$; in fact, we compute responses only at frequency points within the dominant frequency range of the waveguide. The obtained transient waveforms,

shown in Fig. 6.6(a)-(c), are in a good agreement with EVFE responses from [77], Fig. 6.6(d)-(f), having in mind that the two sets of results are obtained with different waveguide excitations – current probes in [77] (with no details provided), as opposed to modal excitations in this present work, as well as that no details are provided in [77] about the actual locations of reference planes with respect to which the responses are given.

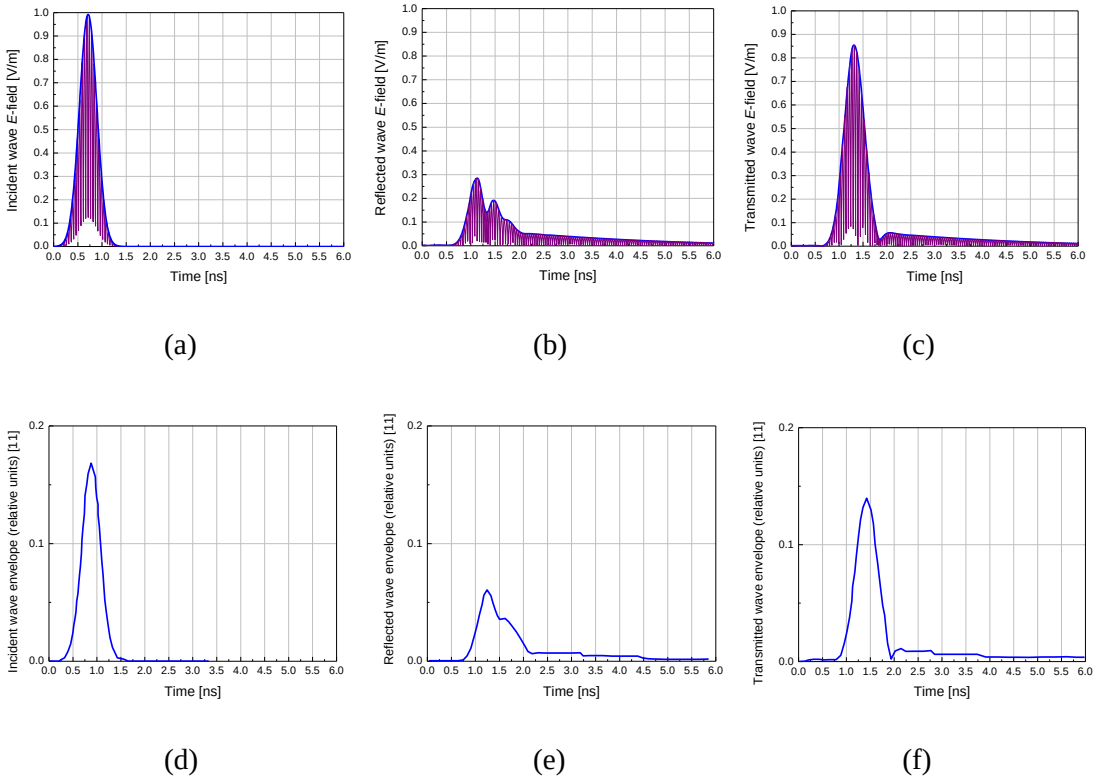

Fig. 6.6. Transient waveforms of incident, reflected and transmitted waves for the structure in Fig. 6.3 and excitation in (6.11): (a)-(c) results obtained by the FEM-DFT/IDFT technique (note that rectified modulated signals are shown within the envelopes) and (d)-(f) EVFE results from [77].

Based on a close analysis of the reflected wave, in Fig. 6.6(b), we realize that the two peaks occurring at $t_{\text{refl1}} \approx 1.135$ ns and $t_{\text{refl2}} \approx 1.5$ ns correspond to the waves reflected

from the front and rear sides of the dielectric post, respectively. Note also that, although the unloaded waveguide sections in front of and behind the post are equally long, the maximum of the transmitted wave, Fig. 6.6(c), arrives at the second port at $t_{\text{trans}} \approx 1.32$ ns , which is in between t_{refl1} and t_{refl2}. This can be attributed to the fact that the transmitted wave travels a slightly shorter distance (from port 1 to port 2) than the wave reflected from the rear side of the post (from port 1 to the rear side and back to port 1). Additionally, the wave reflected from the front side of the post travels only in air (hence, it is the fastest), the wave reflected from the rear side makes a round trip inside the dielectric post (which slows it down considerably), and the transmitted wave travels through the dielectric only in one direction (and thus its average speed is between those of the other two waves).

As the second example, consider a WR-15 waveguide loaded with a continuously inhomogeneous dielectric slab where $\varepsilon_{\text{r}}(u) = 9 - 8u^2$, $-1 < u < 1$ and $u = 2z/c - 1$, as portrayed in Fig. 6.7, where two simple large-domain FEM models are shown as well. The continuously inhomogeneous section can be either modeled by a single continuously inhomogeneous finite element or approximated by a series of piecewise homogeneous dielectric layers. In the former case, we use the FEM technique that implements large finite elements with continuous change of medium parameters throughout their volumes, based on Lagrange interpolating scheme for variations of medium parameters [61]. In the latter case, when the piecewise homogeneous approximation of the dielectric profile is implemented, the original slab is subdivided into N_{layers} equally thick layers with

individual permittivities calculated as an average permittivity of the original profile in the corresponding coordinate range, i.e.,

$$\varepsilon_{ri} = \frac{1}{\Delta z} \int_{z_i}^{z_i+\Delta z} \varepsilon_{\mathrm{r}}(z)\,\mathrm{d}z\,, \quad \Delta z = \frac{c}{N_{\mathrm{layers}}}\,, \quad z_i = (i-1)\Delta z\,, \quad i = 1,2,...,\, N_{\mathrm{layers}}. \tag{6.12}$$

Such piecewise constant permittivities for $N_{\mathrm{layers}} = 3$, 5, and 7, respectively, are given in Table I.

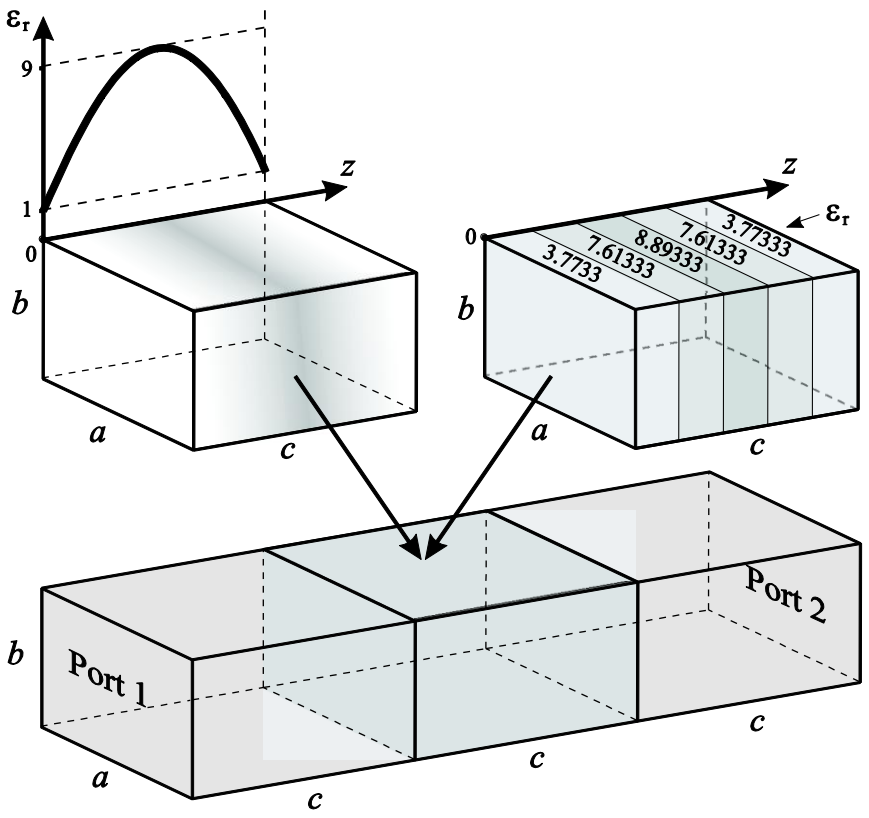

Fig. 6.7. Three-element higher order large-domain FEM model of a WR-15 waveguide ($a = 3.76\,\mathrm{mm}$, $b = 1.88\,\mathrm{mm}$, and $c = 2.5\,\mathrm{mm}$) with a continuously inhomogeneous lossless dielectric load (central element) whose permittivity varies quadratically in the longitudinal direction; five-layer ($N_{\mathrm{layers}} = 5$) model of the load with piecewise constant approximation of the permittivity profile, according to (6.12), is also shown.

Table I. Dielectric permittivities constituting three piecewise homogeneous layered approximations of the continuously inhomogeneous dielectric slab in Fig. 6.7 obtained using (6.12).

No. of layers	Average permittivity of layers (ε_r)						
(N_{layers})	L1	L2	L3	L4	L5	L6	L7
3	5.14815	8.7037	5.14815				
5	3.77333	7.61333	8.89333	7.61333	3.77333		
7	3.06803	6.33333	8.29252	8.94558	8.29252	6.33333	3.06803

Results of the frequency-domain analysis of waveguide structure in Fig. 6.7 are shown in Fig. 6.8. In all the graphs, the higher order FEM solution with the continuously inhomogeneous model is compared to higher order FEM simulations of piecewise homogeneous models with $N_{layers} = 3$ and 7, respectively, and to higher order MoM-SIE [7] results for the $N_{layers} = 7$ approximate model (excitation/reception by wire probes and *S*-parameters de-embedding are done as in Fig. 6.4). It is clearly seen in the four figures that the model with 3 layers provides a poor approximation of the continuous permittivity profile of the slab, yielding very inaccurate *S*-parameters in both magnitude and phase (both equally important for the accurate calculation of transient responses), and that seven (and more) layers are necessary to obtain a fairly good approximation of the profile resulting in a rather accurate *S*-parameter characterization. We also observe a practically exact match of the FEM and MoM solutions for the same $N_{layers} = 7$ model.

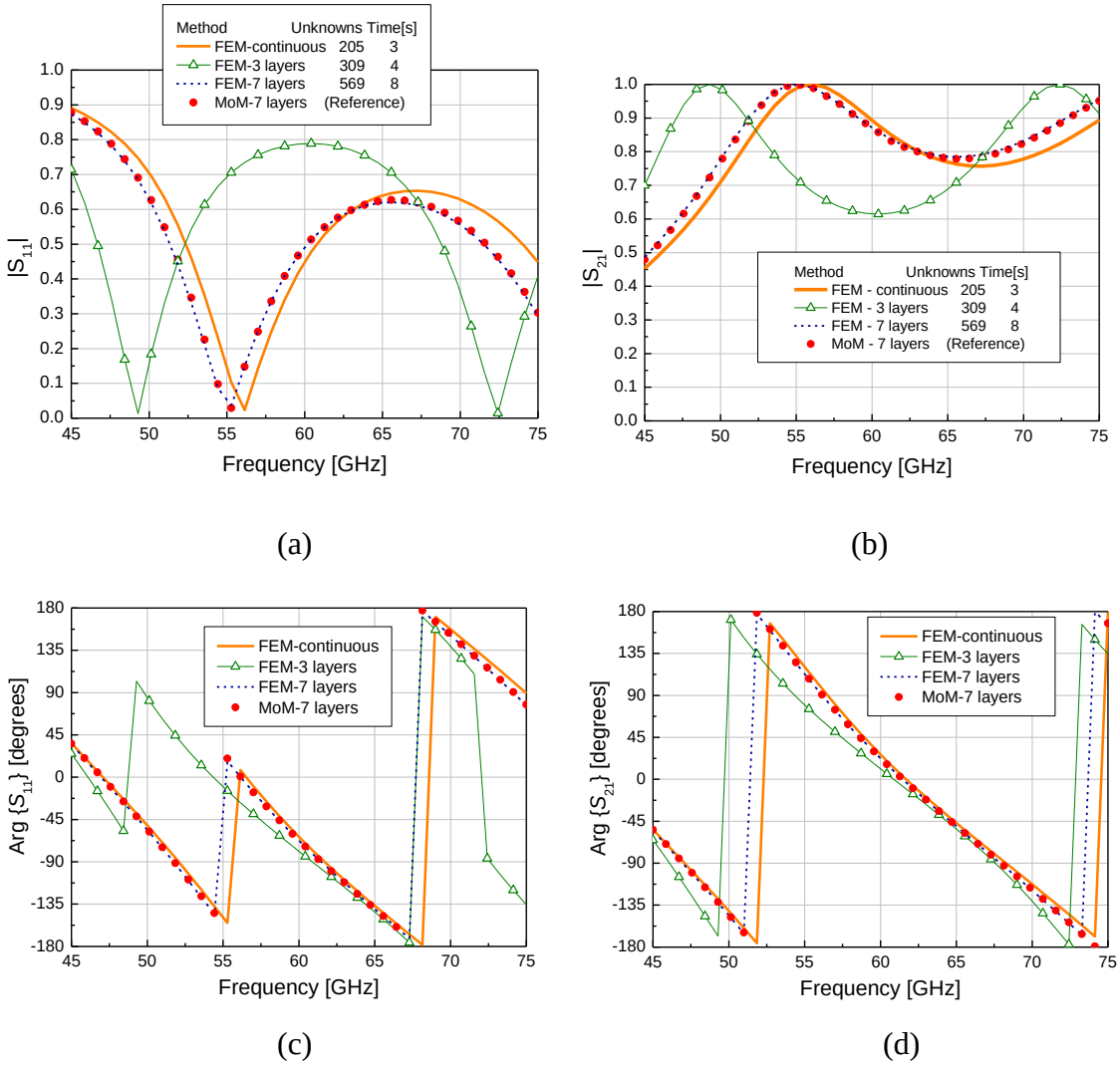

Fig. 6.8. Magnitude and phase (argument) of *S*-parameters of the waveguide structure with a continuously inhomogeneous dielectric load in Fig. 6.7.

For the transient analysis of the structure in Fig. 6.7, we employ the excitation in (6.11) with $f_c = 62\,\text{GHz}$ and $\Delta f = 15\,\text{GHz}$. The sampling frequency is now $f_s = 1240\,\text{GHz}$ ($\Delta t \approx 0.8\,\text{ps}$), whereas the numbers of time and frequency samples are the same as in Fig. 6.6. The results of the FEM DFT/IDFT computation are shown in Fig. 6.9, where we conclude, as expected based on the frequency-domain results in Fig. 6.8, that the transient

response of the $N_{\text{layers}} = 3$ approximate model is significantly less accurate than that with $N_{\text{layers}} = 7$, as compared to the FEM model with the inhomogeneous profile modeled exactly.

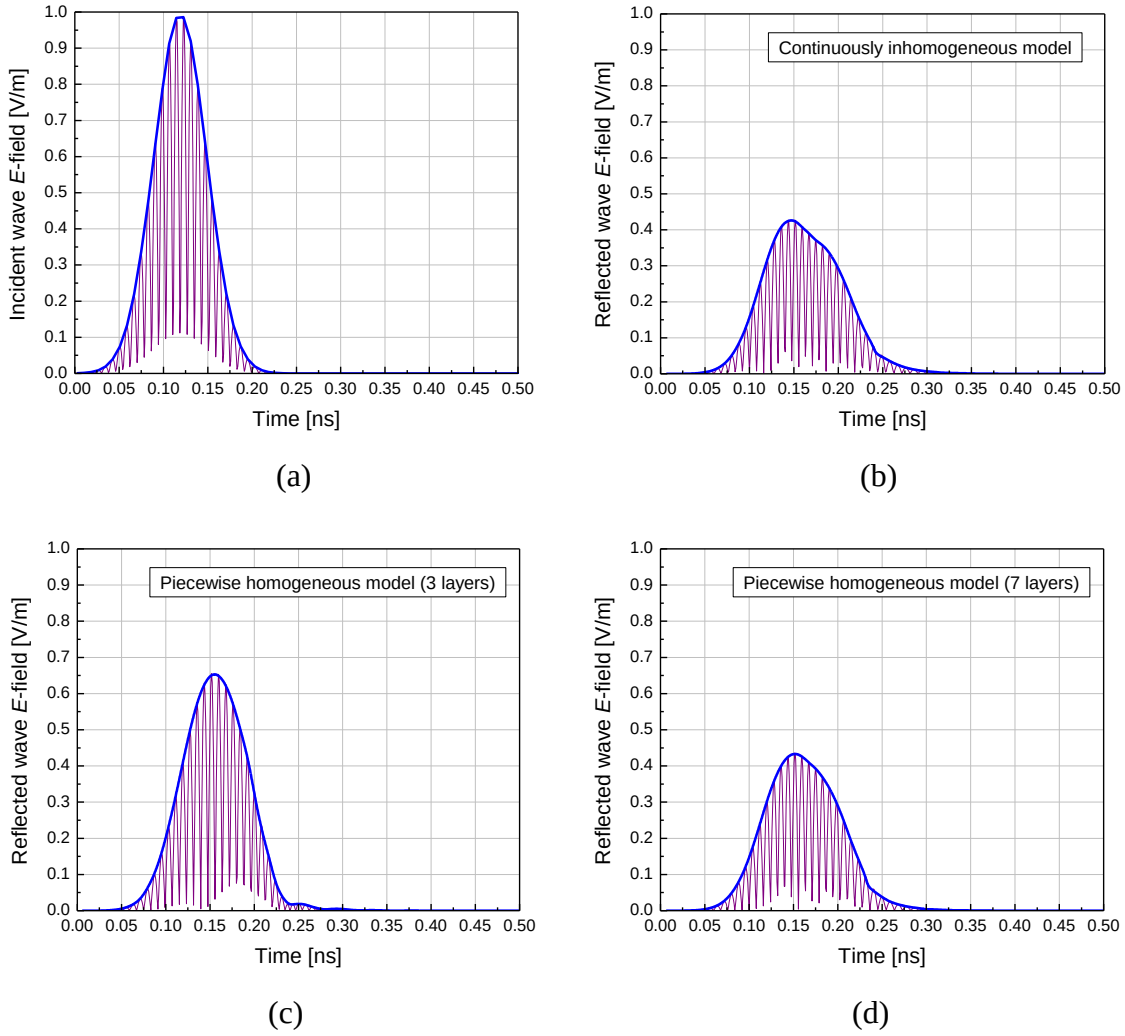

Fig. 6.9. Transient response of the structure in Fig. 6.7 computed by the FEM-DFT/IDFT technique: (a) incident wave, (b) reflected wave for the continuous permittivity profile, (c) reflected wave for the 3-layer approximation of the load (see Table I), and (d) reflected wave for the 7-layer approximation.

6.5. Conclusions: Efficient Time-Domain Analysis of Waveguide Discontinuities Using Higher Order FEM in Frequency Domain

This chapter has presented a computational technique for efficient and accurate time-domain analysis of multiport waveguide structures with arbitrary metallic and dielectric discontinuities using a higher order FEM in the frequency domain. It has demonstrated that with a highly efficient and appropriately designed frequency-domain FEM solver, it is possible to obtain extremely fast and accurate time-domain solutions of microwave passive structures performing computations in the frequency domain along with the discrete Fourier transform and its inverse. The technique is a higher order large-domain Galerkin-type FEM for 3-D analysis of waveguide structures with discontinuities implementing curl-conforming hierarchical polynomial vector basis functions in conjunction with Lagrange-type curved hexahedral finite elements, coupled with standard DFT and IDFT algorithms. To close the waveguide problem, simple single-mode boundary condition and excitation have been introduced across the waveguide ports, with a large buffer finite element at each port to ensure relaxation of higher modes. The technique enables an extremely fast multifrequency analysis of a microwave structure, allowing the global FEM matrix to be filled only once and then reused for every subsequent frequency point, which is of great importance for the evaluation of the time-domain response of the structure based on the frequency-domain analysis, where we need a large number of frequency samples of the resulting quantities (e.g., *S*-parameters of the structure). Numerical examples of waveguide structures that include homogeneous and continuously inhomogeneous dielectric discontinuities have validated and verified the accuracy and efficiency of the presented technique, which appears to be the first time-

from-frequency-domain FEM solver. The examples have demonstrated excellent numerical properties of the technique primarily due to (i) very small total numbers of unknowns in higher order solutions, (ii) great modeling flexibility using large (homogeneous and inhomogeneous) finite elements, and (iii) extremely fast FEM solutions at multiple frequencies needed for the inverse Fourier transform.

7. FUTURE OBJECTIVES

Future research objectives include using the results of this research for the development of an improved front end for higher order large-domain techniques. This front end should enable efficient and accurate modeling of practical electromagnetic structures with a minimum of expert interaction, which so far has not been the case in higher order CEM. Specifically, from the starting point of a simulation input file, this front end function would find and optimize modeling parameters within the input file, thus removing the need for the user to determine the correct settings for those values.

One of the main future tasks is validation and evaluation of the conclusions of this work in analysis of a broader range of electromagnetic structures with arbitrary geometries, electrical sizes, and material compositions. Generality and validity of established guidelines and quantitative recipes for adoptions of optimal higher order parameters for CEM modeling should be investigated in as many as possible different classes of real-world problems in antenna and scattering applications.

Additionally, it would be worthwhile to implement new basis functions constructed from standard orthogonal polynomials; candidate functions are classes of Legendre basis functions and Chebyshev functions. Doing so would further expand the data set discussed in this dissertation, and would improve the functionality of the proposed front end function.

BIBLIOGRAPHY

[1] B. M. Notaroš, "Higher order frequency-domain computational electromagnetics," Special Issue on Large and Multiscale Computational Electromagnetics, *IEEE Transactions on Antennas and Propagation*, vol. 56, no. 8, pp. 2251-2276, August 2008.

[2] J. M. Jin, K. C. Donepudi, J. Liu, G. Kang, J. M. Song, and W. C. Chew, "High-Order Methods in Computational Electromagnetics," in *Fast and Efficient Algorithms in Computational Electromagnetics*, W. C. Chew *et al*, Ed. Norwood, MA: *Artech House*, 2001.

[3] B. M. Kolundzija and A. R. Djordjević, "Electromagnetic Modeling of Composite Metallic and Dielectric Structures", Norwood, MA: *Artech House*, 2002.

[4] A. F. Peterson, "Mapped Vector Basis Functions for Electromagnetic Integral Equations", *Morgan & Claypool Publishers*, 2006.

[5] R. D. Graglia, D. R. Wilton, and A. F. Peterson, "Higher order interpolatory vector bases for computational electromagnetics", *IEEE Transactions on Antennas and Propagation*, vol. 45, no. 3, pp. 329-342, March 1997.

[6] G. Kang, J. Song, W. C. Chew, K. C. Donepudi, and J. M. Jin, "A novel grid-robust higher order vector basis function for the method of moments," *IEEE Transactions on Antennas and Propagation*, vol. 49, pp. 908-915, June 2001.

[7] M. Djordjevic and B. M. Notaros, "Double higher order method of moments for surface integral equation modeling of metallic and dielectric antennas and scatterers," *IEEE Transactions on Antennas and Propagation*, vol. 52, no. 8, pp. 2118-2129, August 2004.

[8] E. Jørgensen, J. L. Volakis, P. Meincke, and O. Breinbjerg, "Higher order hierarchical Legendre basis functions for electromagnetic modeling," *IEEE Transactions on Antennas and Propagation*, vol. 52, pp. 2985-2995, November 2004.

[9] B. M. Kolundzija and B. D. Popovic, ''Entire-domain Galerkin method for analysis of generalized wire antennas and scatterers,'' *Proc. IEE H*, vol. 139, no. 1, February 1992, pp. 17–24.

[10] B. M. Kolundžija, "Accurate solution of square scatterer as benchmark for validation of electromagnetic modeling of plate structures," *IEEE Transactions on Antennas and Propagation*, vol. 46, pp. 1009-1014, July 1998.

[11] B. M. Notaros, B. D. Popovic, J. P.Weem, R. A. Brown, and Z. Popovic, "Efficient large-domain MoM solution to electrically large practical EM problems," *IEEE Trans. Microwave Theory Tech.*, vol. 49, pp. 151–159, Jan. 2001.

[12] B. D. Popovic and B. M. Kolundzija, *Analysis of Metallic Antennas and Scatterers*, ser. Electromagn. Wave Series 38. London, U.K.: IEE Press, 1994.

[13] S. Wandzura, "Electric-current basis functions for curved surfaces," *Electromagnetics*, vol. 12, no. 1, pp. 77–91, 1992.

[14] L. F. Canino, J. J. Ottusch, M. A. Stalzer, J. L. Visher, and S. M. Wandzura, "Numerical solution of the Helmholtz equation in 2D and 3D using a high-order Nyström discretization," *J. Comput. Phys.*, vol. 146, no. 2, pp. 627–663, 1998.

[15] N. Y. Zhu and F. M. Landstorfer, "Application of curved parametric triangular and quadrilateral edge elements in the moment method solution of the EFIE," *IEEE Microwave and Guided Wave Letters*, vol. 3, no. 9, pp. 319 - 321, September 1993.

[16] E. Jørgensen, J. L. Volakis, P. Meincke, and O. Breinbjerg, "Higher order hierarchical legendre basis functions for electromagnetic modeling," *IEEE Transactions on Antennas and Propagation*, vol. 52, pp. 2985-2995, November 2004.

[17] K. C. Donepudi, J. M. Jin, and W. C. Chew, "A higher order multilevel fast multipole algorithm for scattering from mixed conducting/dielectric bodies," *IEEE Transactions on Antennas and Propagation*, vol. 51, pp. 2814-2821, October 2003.

[18] B. D. Popović, M. D. Dragović, and A. R. Djordjević, "Analysis and synthesis of wire antennas," Chichester/New York: *Research Studies Press/Wiley*, 1982.

[19] N. J. Champagne, D. R. Wilton, and J. D. Rockway, "The analysis of thin wires using higher order elements and basis functions," *IEEE Transactions on Antennas and Propagation*, vol. 54, pp. 3815-3821, December 2006.

[20] L. R. Hamilton, J. J. Ottusch, M. A. Stalzer, R. S. Turley, J. L. Visher, and S. M. Wandzura, "Numerical solution of 2-D scattering problems using high-order methods," *IEEE Transactions on Antennas and Propagation*, vol. 47, pp. 683-691, April 1999.

[21] A. F. Peterson, "Accuracy of currents produced by the locally-corrected Nyström method and the method of moments when used with higher-order representations," *Applied Computational Electromagnetics Society (ACES) Journal*, vol. 17, no. 1, pp. 74-83, 2002.

[22] B. M. Notaros, B. D. Popovic, J. P. Weem, R. A. Brown, and Z. Popovic, "Efficient large-domain MoM solutions to electrically large practical EM problems," *IEEE Transactions on Microwave Theory and Techniques*, vol. 49, no. 1, pp.151-159, January 2001.

[23] J. P. Webb, "Hierarchical vector basis functions of arbitrary order for triangular and tetrahedral finite elements", *IEEE Transactions on Antennas and Propagation*, vol. 47, no. 8, pp. 1244-1253, August 1999.

[24] M. M. Ilic and B. M. Notaros, "Higher order hierarchical curved hexahedral vector finite elements for electromagnetic modeling," *IEEE Transactions on Microwave Theory and Techniques*, vol. 51, no. 3, pp.1026-1033, March 2003.

[25] M. M. Ilic and B. M. Notaros, "Higher order large-domain hierarchical FEM technique for electromagnetic modeling using Legendre basis functions on generalized hexahedra," *Electromagnetics*, vol. 26, no. 7, pp. 517-529, October 2006.

[26] M. M. Ilic, A. Z. Ilic, and B. M. Notaros, "Higher Order Large-Domain FEM Modeling of 3-D Multiport Waveguide Structures with Arbitrary Discontinuities," *IEEE Transactions on Microwave Theory and Techniques*, vol. 52, no. 6, pp.1608-1614, June 2004.

[27] J. M. Jin, "The Finite Element Method in Electromagnetics", 2nd ed., *John Wiley & Sons*, New York, 2002.

[28] P. P. Silvester and R. L. Ferrari, "Finite Elements for Electrical Engineers", 3rd ed., *Cambridge University Press*, 1996.

[29] J. S. Wang and N. Ida, "Curvilinear and higher order 'edge' finite elements in electromagnetic field computation", *IEEE Transactions on Magnetics*, vol. 29, No. 2, pp. 1491-1493, March 1993.

[30] J. S. Savage and A. F. Peterson, "Higher-order vector finite elements for tetrahedral cells", *IEEE Transactions on Microwave Theory and Techniques*, vol. 44, no. 6, pp. 874-879, June 1996.

[31] X. Q. Sheng and S. Xu, "An efficient high-order mixed-edge rectangular-element method for lossy anisotropic dielectric waveguides," *IEEE Transactions on Microwave Theory and Techniques,* vol. 45, pp. 1009-1013, July 1997.

[32] M. M. Botha and J. M. Jin, "Adaptive Finite Element-Boundary Integral Analysis for Electromagnetic Fields in 3-D," *IEEE Transactions on Antennas and Propagation*, vol. 53, no. 5, pp. 1710-1720, May 2005.

[33] D. K. Sun and Z. Cendes, "Fast High-Order FEM Solutions of Dielectric Wave Guiding Structures," *IEE Proceedings: Microwaves, Antennas and Propagation*, vol. 150, no. 4, pp. 230-236, August 2003.

[34] L. S. Andersen and J. L. Volakis, "Accurate and efficient simulation of antennas using hierarchical mixed-order tangential vector finite elements for tetrahedra", *IEEE Transactions on Antennas and Propagation*, vol. 47, no. 8, pp. 1240-1243, August 1999.

[35] R. D. Graglia, and I. L. Gheorma, "Higher order interpolatory vector bases on pyramidal elements," *IEEE Transactions on Antennas and Propagation*, vol. 47, pp. 775-782, May 1999.

[36] B. M. Dillon and J. P. Webb, "A Comparison of Formulations for the Vector Finite Element Analysis of Waveguides," *IEEE Transactions on Microwave Theory and Techniques,* vol. 42, no. 2, pp. 308-316, February 1994.

[37] M. M. Ilić, M. Djordjević, A. Ž. Ilić, and B. M. Notaroš, "Higher order hybrid FEM-MoM technique for analysis of antennas and scatterers," *IEEE Trans. Antennas Propag.*, vol. 57, pp. 1452-1460, May 2009.

[38] M. Djordjevic and B. M. Notaros, "Higher Order Hybrid Method of Moments–Physical Optics Modeling Technique for Radiation and Scattering from Large Perfectly Conducting Surfaces," *IEEE Transactions on Antennas and Propagation*, vol. 53, no. 2, pp. 800-813, February 2005.

[39] E. Martini, G. Pelosi, and S. Selleri, "A Hybrid Finite-Element—Modal-Expansion Method With a New Type of Curvilinear Mapping for the Analysis of Microwave Passive Devices," *IEEE Transactions on Microwave Theory and Techniques*, vol. 51, no. 6, pp. 1712-1717, June 2003.

[40] J. Liu, and J. M. Jin, "A novel hybridization of higher order finite element and boundary integral methods for electromagnetic scattering and radiation problems," *IEEE Transactions on Antennas and Propagation*, vol. 49, pp. 1794-1806, December 2001.

[41] E. Jørgensen, P. Meincke, and O. Breinbjerg, "A Hybrid PO - Higher-Order Hierarchical MoM Formulation using Curvilinear Geometry Modeling", *2003 IEEE Antennas and Propagation Society International Symposium Digest*, Columbus, OH, U.S.A., vol. 4, pp. 98-101, June 22-27, 2003.

[42] J. L. Volakis, K. Sertel, and B. C. Usner, "Frequency Domain Hybrid Finite Element Methods in Electromagnetics," *Morgan & Claypool Publishers*, 2006.

[43] G. E. Antilla and N. G. Alexopoulos, "Scattering from complex three-dimensional geometries by a curvilinear hybrid finite element-integral equation approach," *Journal of the Optical Society of America A*, vol. 11, no. 4, pp. 1445-1457, April 1994.

[44] B. D. Popovic, "Polynomial approximation of current along thin symmetrical cylindrical dipoles," *IEE Proceedings*, vol. 117, pp. 873-878, 1970.

[45] B. M. Kolundzija, ''Comparison of a class of sub-domain and entire-domain basis functions automatically satisfying KCL,'' *IEEE Trans. on Antennas and Propagat.*, vol. 44, no. 10, pp. 1362–1366, October 1996.

[46] B. M. Notaros and B. D. Popovic, "Optimized entire-domain moment-method analysis of 3D dielectric scatterers," *International Journal of Numerical Modelling: Electronic Networks, Devices and Fields*, vol. 10, pp.177-192, 1997.

[47] V. V. Petrovic and B. D. Popovic, "Optimal FEM solutions of one dimensional EM problems," *Inte. J. Numer. Model.: Electron. Networ.,Devices and Fields*, vol. 14, pp. 49–68, 2001.

[48] R. Cools and P. Rabinowitz, "Monomial cubature rules since "Stroud": a compilation," *Journal of Computational and Applied Mathematics*, vol. 48, pp. 309-326, 1993.

[49] M. M. Bibby and A. F. Peterson, "High accuracy calculation of the magnetic vector potential on surfaces," *Aces Journal*, vol. 18, no. 1, pp. 12-22B, March 2003.

[50] M. A. Khayat and D. R. Wilton, "Numerical evaluation of singular and near singular potential integrals," *IEEE Transactions on Antennas and Propagation*, vol. 53, no. 10, pp. 3180-3190, October 2005.

[51] T. Ozdemir and J. L. Volakis, "Triangular prisms for edge-based vector finite element analysis of conformal antennas," *IEEE Transactions on Antennas and Propagation*, vol. 45, no. 5, pp. 788-797, May 1997.

[52] E. M. Klopf, N. J. Šekeljić, M. M. Ilić, and B. M. Notaroš, "Optimal Modeling Parameters for Higher Order MoM-SIE and FEM-MoM Electromagnetic Simulations", under review for *IEEE Transactions on Antennas and Propagation*, 2011.

[53] E. M. Klopf, S. B. Manić, M. M. Ilić, and B. M. Notaroš, "Efficient Time-Domain Analysis of Waveguide Discontinuities Using Higher Order FEM in Frequency Domain", *Progress in Electromagnetics Research*, PIER 120, pp. 215-234, 2011.

[54] M. E. Honnor, J. Trevelyan, P. Bettess, M. El-hachemi, O. Hassan, K. Morgan, and J. J. Shirron, "An integration scheme for electromagnetic scattering using plane wave edge elements," *Advances in Engineering Software*, 2008.

[55] R. F. Harrington, "Field Computation by Moment Methods", *IEEE PRESS Series on Electromagnetic Waves*, Piscataway, 1993.

[56] S. M. Rao, C. C. Cha, R. L. Cravey, and D. L. Wilkes, "Electromagnetic scattering from arbitrary shaped conducting bodies coated with lossy materials of arbitrary thickness", *IEEE Transactions on Antennas and Propagation*, vol. 39, no. 5, pp.627-631, May 1991.

[57] M. Analoui, M. and Y. Kagawa, "Electromagnetic scattering from conductor-coated material bodies", *International Journal of Numerical Modelling: Electronic Networks, Devices and Fields*, vol.4, no. 4, pp. 287-299, December 1991.

[58] S. M. Rao, T. K. Sarkar, P. Midya, and A. R. Djordjevic, "Electromagnetic radiation and scattering from finite conducting and dielectric structures: surface/surface formulation", *IEEE Transactions on Antennas and Propagation*, vol. 39, no. 7, pp. 1034–1037, July 1991.

[59] M. Djordjević and B. M. Notaroš, "Higher-Order Hierarchical Basis Functions with Improved Orthogonality Properties for Moment-Method Modeling of Metallic and Dielectric Microwave Structures", *Microwave and Optical Technology Letters*, vol. 37, no. 2, pp. 83-88, April 20 2003.

[60] M. M. Ilic, "Higher Order Hexahedral Finite Elements for Electromagnetic Modeling," Ph.D. dissertation, Dept. of Elect. & Comp. Eng., Univ. of Mass. Dartmouth, Dartmouth, MA, 2003.

[61] M. M. Ilic, A. Z. Ilic, and B. M. Notaros, "Continuously Inhomogeneous Higher Order Finite Elements for 3-D Electromagnetic Analysis," *IEEE Transactions on Antennas and Propagations*, vol. 57, no. 9, September 2009, pp. 2798-2803.

[62] M. M. Ilic and B. M. Notaros, "Trilinear hexahedral finite elements with higher-order polynomial field expansions for hybrid SIE/FE large-domain electromagnetic modeling," in *IEEE AP-S Int. Symp. Dig.*, Boston, MA, July 8–13, 2001, pp. III.192–III.195.

[63] M. M. Ilic and B. M. Notaros, "Computation of 3-D electromagnetic cavity resonances using hexahedral vector finite elements with hierarchical polynomial basis functions," in *IEEE AP-S Int. Symp. Dig.*, San Antonio, TX, June 16–21, 2002, pp. IV.682–685.

[64] B. M. Notaros and B. D. Popovic, "General entire-domain method for analysis of dielectric scatterers," *Proc. Inst. Elect. Eng.*, pt. H, vol. 143, no. 6, pp. 498–504, Dec. 1996.

[65] B. M. Notaros and B. D. Popovic, "General entire-domain Galerkin method for analysis of wire antennas in the presence of dielectric bodies," *Proc. Inst. Elect. Eng.*, pt. H, vol. 145, no. 1, pp. 13–18, Feb. 1998.

[66] B. M. Notaros and B. D. Popovic, "Large-domain integral-equation method for analysis of general 3D electromagnetic structures," *Proc. Inst. Elect. Eng.*, pt. H, vol. 145, no. 6, pp. 491–495, December 1998.

[67] B. D. Popovic and B. M. Notaros, "Moment-method analysis of volume dielectric scatterers. Four independent entire-domain solutions: Is entire-domain philosophy a luxury or necessity in the method of moments?," *International Journal of Microwave and Millimeter-Wave Computer-Aided Engineering*, vol. 6, no. 6, November 1996, pp.454-473.

[68] B. M. Kent, "Comparative measurements of precision radar cross section (RCS) calibration targets," *IEEE Antennas and Propagation Society International Symposium, 2001.*, vol. 4, pp. 412-415, 2001.

[69] J. Ruoskanen, P. Eskelinen, H. Heikkila, P. Kuosmanen, T. Kiuru, , "A practical millimeter-wave radar calibration target," *IEEE Antennas and Propagation Magazine,* vol. 46, no. 2, pp. 94- 97, April 2004.

[70] P. S. P. Wei, A. W. Reed, C. N. Ericksen, and R. K. Schuessler, "Measurements and calibrations of larger squat cylinders," *IEEE Antennas and Propagation Magazine*, vol.51, no. 2, pp. 205-212, April 2009.

[71] A. C. Woo, H. T. G. Wang, M. J. Schuh, and M. L. Sanders, "Benchmark radar targets for the validation of computational electromagnetics programs," *IEEE Antennas and Propagation Magazine,* vol.35, no. 1, pp. 84-89, February 1993.

[72] A. Yaghjian and R. McGahan, "Broadside radar cross section of the perfectly conducting cube," *IEEE Transactions on Antennas and Propagation*, vol. 33, pp. 321–329, March 1985.

[73] www.feko.info/applications/white-papers/rcs-benchmarking-of-generic-shapes/

[74] M. El Sabbagh and K. Zaki, "Modeling of Rectangular Waveguide Junctions Containing Cylindrical Posts," *Progress In Electromagnetics Research*, PIER 33, pp. 299–331, 2001.

[75] J. M. Jin and D. J. Riley, "Finite Element Analysis of Antennas and Arrays", *John Wiley & Sons*, New York, 2008.

[76] D. I. Olcan, M. M. Nikolic, B. M. Kolundzija, and A. R. Djordjevic, "Time-domain Response of 3-D Structures Calculated Using WIPL-D," *Proceedings of the 2007 Annual Review of Progress in Applied Computational Electromagnetics – ACES 2007,* March 2007, Verona, Italy, pp. 525-531.

[77] H. P. Tsai, Y. Wang, and T. Itoh, "Efficient Analysis of Microwave Passive Structures Using 3-D Envelope-Finite element (EVFE)," *IEEE Transactions on Microwave Theory and Techniques*, vol. 50, no. 12, pp. 2721-2727, December 2002.

[78] B. Kolundzija, B. Janic, and M. Rakic, "Novel technique for deembeding S-parameters in electromagnetic modeling of arbitrary circuits," *2004 IEEE APS International Symposium Digest*, June 2004, Monterey, CA, U.S.A., pp. 2784-2787.

[79] E. M. Klopf, N. J. Sekeljic, M. M. Ilic, and B. M. Notaros, "Investigations of optimal geometrical and field/current modeling parameters for higher order FEM, MoM, and hybrid CEM techniques," *Proc. 2011 USNC-URSI National Radio Science Meeting*, January 5-8, 2011, Boulder, Colorado.